

Understanding the Carbon Morphology in Sulfonated-Silica Ceramic Carbon Electrodes for the PEM Fuel Cell Device

by

Veronica Janie Cavallari

A thesis submitted to the
School of Graduate and Postdoctoral Studies in partial
fulfillment of the requirements for the degree of

Master of Science in Materials Science

Faculty of Science

University of Ontario Institute of Technology (Ontario Tech University)

Oshawa, Ontario, Canada

March, 2020

© Veronica Janie Cavallari, 2020

THESIS EXAMINATION INFORMATION

Submitted by: **Veronica Janie Cavallari**

Master of Science in Materials Science

Thesis title: **Understanding the Carbon Morphology in Sulfonated-Silica Ceramic Carbon Electrodes for the PEM Fuel Cell Device**

An oral defense of this thesis took place on March 31, 2020 in front of the following examining committee:

Examining Committee:

Chair of Examining Committee	Dr. Franco Gaspari
Research Supervisor	Dr. Brad Easton
Examining Committee Member	Dr. Olena Zenkina
Examining Committee Member	Dr. Igor Svishchev
External Examiner	Dr. Theresa Stotesbury

The above committee determined that the thesis is acceptable in form and content and that a satisfactory knowledge of the field covered by the thesis was demonstrated by the candidate during an oral examination. A signed copy of the Certificate of Approval is available from the School of Graduate and Postdoctoral Studies.

ABSTRACT

Using hydrogen and oxygen gas, the fuel cell is a device that converts chemical energy into electrical energy. Particularly, the proton exchange membrane fuel cell, has multiple components, all that are consistently being studied in order to further increase its practicality. One particular limitation of the fuel cell is the use of the precious metal Pt within the catalyst layer. Efforts in decreasing the amount of Pt has provided information on improved utilization of the catalytic metal. Another limitation can be attributed to the perfluorosulfonated ionomer Nafion[®], that is commercially available and used as a binder within the catalyst layer. The high cost and poor durability of current fuel cell catalyst layers has been linked to the use of Nafion[®] and the amount of carbon in the catalyst.

In this work, 40 wt% Pt/C catalyst is used to obtain total electrode loadings as low as 0.2 mgPt cm⁻², with the hypothesis of increased energy density while reducing catalyst layer thickness. This catalyst is used in conjunction with a Nafion[®]-replacement ionomer that contains sulfonated silica, and provides comparable performance while increasing durability. This work also includes the substitution of the typical carbon support, Vulcan, with ordered mesoporous carbon. In order to grasp a better understanding of the catalyst as a whole, mesoporous carbon will be used in efforts of obtaining more uniform Pt dispersion and greater catalytic activity. With a successful synthetic route of the mesoporous carbon, further studies are required for enhanced Pt deposition techniques on the two-dimensional support.

Keywords: Proton exchange membrane fuel cell; sulfonated silica ceramic carbon electrodes; catalyst layer; ordered mesoporous carbon; clean energy device.

AUTHOR'S DECLARATION

I hereby declare that this thesis consists of original work of which I have authored. This is a true copy of the thesis, including any required final revisions, as accepted by my examiners.

I authorize the University of Ontario Institute of Technology to lend this thesis to other institutions or individuals for the purpose of scholarly research. I further authorize University of Ontario Institute of Technology to reproduce this thesis by photocopying or by other means, in total or in part, at the request of other institutions or individuals for the purpose of scholarly research. I understand that my thesis will be made electronically available to the public.

Veronica Janie Cavallari

STATEMENT OF CONTRIBUTIONS

Part of the work described in Chapter 3 has been published as:

Easton, E. Bradley, Acheampong, Richard, Alipour Moghadam Esfahani, Reza, Cavallari, Veronica J, Moghaddam, Reza B., Fruehwald, Holly M, Afsahi, Foroughazam, “Recent Advances with Sulfonated Silica Ceramic Carbon Electrodes for Fuel Cells”, *ECS Transactions*, 92 (2019) 559-570. [doi: 10.1149/09208.0559ecst](https://doi.org/10.1149/09208.0559ecst)

In Chapter 3, all 20% Pt/C SS-CCE data was sourced from previous Easton Lab member, Richard Acheampong (MSc).

Silica precursor, SBA-15, described in Chapter 4 was synthesized by Dr. Alessandro H.A. Monteverde Videla of Politecnico di Torino (PdT), Torino, Italy. The OMC₁₅ material was synthesized by me at PdT under the supervision of Stefania Specchia (MSc). Pt deposition and catalyst testing were optimized at Ontario Tech University, in the Easton lab.

ACKNOWLEDGEMENTS

I would like to dedicate this thesis to my late grandfathers, Dermot “Jim” Lavery and Michele Cavallari, both of whom I lost during the years of my Masters. These two men taught me to be resilient in life and to be proud of who I am, and what I have accomplished. For that, I will be forever grateful.

A very appreciative thank-you is in order for my supervisor, Dr. Brad Easton. He has shown a lot of patience and dedication with me and my work, which is ultimately how I got to the end stage of my studies. From the moment I joined his lab in 2015, I was constantly learning and being encouraged to do more. Every project I have worked on over the years has taught me patience, confidence, and a lot of electrochemistry.

The Easton lab group almost seems to be in constant motion, with students coming and going all year round. With that I would like to thank each and every Easton lab member, past and present, for the shared wisdom, shared pain, and the laughs throughout the years. A special thanks is kept for Holly Fruehwald (PhD candidate) who is my friend before my lab mate. I know she has been and always will be my number one supporter, and I try, and will continue to try, to return the efforts. A few other lab mates who have helped me, professionally and personally, over the years include: Dr. Mohammadreza Ghavidel, Dr. Reza B. Moghaddam, Dr. Reza Alipour, Dr. Foroughazam Afsahi, Richard Acheampong (MSc), and Mason Sullivan (MSc candidate). The list will continue with many thanks in mind.

I am grateful for the chemistry undergraduate department for providing means of work through my TAsip and for the opportunity to work full-time, as a chemical technician. I have learned tremendous amounts from every person and would like to

individually thank Dr. Richard Bartholomew, Genevieve Barnes, Michael Allison, Clayton Jakins and Stephanie Mavilla. I have only felt amazing support and encouragement from these people, throughout the years, and the conversations and laughs brought me ease during stressful times. I would also like to thank Shumail Kamal for always being a listening ear and for being one of the best TAs this department has.

I would like to thank all of my friends within the Ontario Tech and Durham College community. The campuses are full of kind and welcoming people, all whom have made my experience that much greater. I will also thank all of my friends outside of the institution, especially Angela, Lauren and Melissa, who listened to my “non-sense” about carbon and supported me whenever I needed it. Thank you Maajida Darsot for being such a great support and amazing friend throughout it all. A special thanks to my best friend of over 17 years, Erin Crooks, who has been there to help me through my toughest decisions and to help me see the potential I have that I sometimes cannot see.

One final, and maybe the largest, piece of gratitude goes out to my family, especially my parents, Lorenzo and Janet, my three older siblings, Daniel, Samantha and Brianna, and my Nonna, Maria. You all constantly see the best in me, sometimes with standards that are a bit too high, but it has helped me through more than any of you would know. My love for each of you is extremely immense and I will always look up to each and every one of you. Lastly, to my boyfriend, James Alexandre, you have helped me through the final stages of my degree and I appreciate that so very much. The motivation you have for me helps me be the best version of myself, and I can say, has helped me wrap-up this great accomplishment.

TABLE OF CONTENTS

THESIS EXAMINATION INFORMATION	ii
ABSTRACT.....	iii
AUTHOR’S DECLARATION	iv
STATEMENT OF CONTRIBUTIONS	v
ACKNOWLEDGEMENTS	vi
Chapter 1. Introduction.....	1
1.1 Background.....	1
1.2 The Proton Exchange Membrane Fuel Cell (PEMFC).....	3
1.3 The Membrane Electrode Assembly (MEA)	4
1.3.1 The Proton Exchange Membrane (PEM)	5
1.3.2 Electrode Materials.....	6
1.3.3 PEMFC Catalyst Layer	8
1.4 PEMFC Catalyst Support.....	9
1.4.1 Ordered Mesoporous Carbon (OMC)	10
1.5 Ceramic Carbon Electrodes	11
1.5.1 Sulfonated-Silica Ceramic Carbon Electrode (SS-CCE)	13
1.6 Objectives.....	14

Chapter 2. Experimental Synthesis and Characterization Techniques..16

2.1	Synthesis and Preparation of SS-CCE	16
2.2	Fabrication of Nafion®-Bound Electrodes	17
2.3	Synthesis of Pt/ OMC₁₅	17
2.3.1	Synthesis of OMC₁₅ using the Silica Template.....	17
2.3.2	Platinum Deposition onto OMC₁₅.....	18
2.3.3	Preparation of Pt/ OMC₁₅ Ink and Electrode	18
2.4	Materials Characterization Techniques.....	19
2.4.1	Thermogravimetric Analyses (TGA)	19
2.4.2	Brunauer-Emmett-Teller (BET) Surface Area and Pore Size Analyses..	20
2.4.3	Scanning Electron Microscopy (SEM) and Energy Dispersive X-Ray Spectroscopy (EDX)	20
2.4.4	X-Ray Diffraction (XRD)	20
2.5	Electrochemical Measurements	21
2.5.1	Three- Electrode Testing for OMC₁₅ Catalysts.....	21
2.5.1.1	Cyclic Voltammetry (CV)	22
2.5.1.2	Electrochemical Impedance Spectroscopy (EIS)	24
2.5.1.3	Accelerated Stress Testing (AST) with Oxygen Reduction Reaction (ORR) Activity	25

2.5.2	Hydrogen Fuel Cell Testing for SS-CCE Catalysts	25
2.5.2.1	Cyclic Voltammetry and Electrochemical Impedance Spectroscopy	27
2.5.2.2	Fuel Cell Performance Testing.....	27
Chapter 3. Investigating the Ionomer in Vulcan-based Catalysts		28
3.1	Compositional Analyses of Fuel Cell Catalyst Materials	28
3.2	Comparison of SS-CCEs Fabricated from 20% Pt/C versus 40% Pt/C	36
3.3	Electrochemical Comparison of Ionomers in 40% Pt/C Catalyst Layers...	41
3.3.1	Studying Temperature Dependence on Different Ionomers.....	41
3.3.2	Studying Relative Humidity Dependence on Electrochemical Characteristics	48
3.3.2.1	Studying the Effects of Cathodic Inlet Gas on Fuel Cell Performance .	55
3.4	Summary	64
Chapter 4. Studying Non-Vulcan Based Catalyst Support.....		66
4.1	Morphology and Composition of Carbon Materials.....	66
4.2	Electrochemical Studies on OMC ₁₅ Materials.....	73
4.3	Summary	85
Chapter 5. Conclusions and Future Directions.....		87
References.....		91

LIST OF TABLES

Chapter 3. Investigating the Ionomer in Vulcan-based Catalysts

Table 3.1. Summary of physical properties of the studied fuel cell catalyst materials. 31

Table 3.2. ECSA values from integrated hydrogen desorption region of CV's for 40% Pt/C SS-CCE and 20% Pt/C SS-CCE, at operating cell temperatures of 30°C and 80°C.
..... 38

Table 3.3. Electrochemically active surface area calculated from CV data for the symmetric MEA comprised of 40% Pt/C SS-CCE versus 40% Pt/C NBE at operating temperatures of 30°C and 80°C..... 44

Chapter 4. Studying Non-Vulcan Based Catalyst Support

Table 4.1. Summary of physical properties of the studied catalyst materials. 68

Table 4.2. Summary of electrochemical results from CV and ORR LSV..... 75

Table 4.3. Summary of electrochemical results for testing Pt/OMC₁₅ and 20% Pt/Vulcan before and after AST. 83

LIST OF FIGURES

Chapter 1. Introduction

Figure 1.1. Schematic diagram of the proton exchange membrane fuel cell device.....	4
Figure 1.2. Schematic diagram of the membrane electrode assembly (MEA) in a PEMFC. ¹⁶	5
Figure 1.3. Representation of a typical PEMFC electrode (not to scale).	7
Figure 1.4. Diagram comparing a Nafion [®] -based and a sulfonated-silica ceramic carbon electrode CL, adapted from Alipour et al. ²¹	8
Figure 1.5. Display of steps for hard-templating method for synthesis of OMC ₁₅	10
Figure 1.6. Chemical structures of a) Nafion [®] , b) TPS, and c) TEOS.	14

Chapter 2. Experimental Synthesis and Characterization Techniques

Figure 2.1. Three-electrode set up on the Pine Instruments potentiostat showing the reference electrode (RE), the counter electrode (CE), and the working electrode (WE) in contact with the MSR rotator.	22
Figure 2.2. Example cyclic voltammogram of 20 wt% Pt/C (Johnson Matthey) in 0.5 M H ₂ SO ₄ at 20 mV/s displaying characteristic features of a Pt cyclic voltammogram.	23
Figure 2.3. Typical EIS measurement for fuel cell catalysts.....	24
Figure 2.4. The Fuel Cell Technologies, Inc. testing station at Ontario Tech University.	26

Figure 2.5. Typical fuel cell operation polarization curve comparing to the theoretical performance.....	27
-----------------------------------------------------------------------------------------------------------------	----

Chapter 3. Investigating the Ionomer in Vulcan-based Catalysts

Figure 3.1. 40% Pt/C SS-CCE, commercial 40% Pt/C (Premetek), and NBE material made with 40% Pt/C a) thermograms and b) derivative thermograms to determine Pt catalyst and ionomer loading.....	29
--------------------------------------------------------------------------------------------------------------------------------------------------------------------------------------------------------	----

Figure 3.2. Brunauer-Emmett-Teller analyses of three fuel cell catalyst materials 40% Pt/C SS-CCE, commercial 40% Pt/C (Premetek), and commercial Vulcan XC-72 showing both adsorption (filled symbols) and desorption (open symbols) curves for measuring specific surface area.....	31
----------------------------------------------------------------------------------------------------------------------------------------------------------------------------------------------------------------------------------------------------------------------------------------------	----

Figure 3.3. Overlaid X-ray diffraction patterns of three fuel cell catalyst materials commercial 40% Pt/C (Premetek), 40% Pt/C NBE material, and 40% Pt/C SS-CCE, including Miller Indices of Pt and C facets.....	32
---------------------------------------------------------------------------------------------------------------------------------------------------------------------------------------------------------------------------	----

Figure 3.4. Definitive EDX sample image of a SS-CCE fuel cell electrode for determination of catalyst layer thickness.	33
------------------------------------------------------------------------------------------------------------------------------------	----

Figure 3.5. Energy dispersive X-ray spectroscopy mapping of three fuel cell electrodes a) 40% Pt/C Nafion®-bound electrode, b) 40% Pt/C SS-CCE, and c) 20% Pt/C SS-CCE.	34
-------------------------------------------------------------------------------------------------------------------------------------------------------------------------------------	----

Figure 3.6. Scanning electron microscopy images of three fuel cell electrodes a) 40% Pt/C Nafion®-bound electrode, b) 40% Pt/C SS-CCE, and c) 20% Pt/C SS-CCE.	35
----------------------------------------------------------------------------------------------------------------------------------------------------------------------------	----

Figure 3.7. H ₂ /O ₂ fuel cell polarization curves comparing current density against a) cell potential and b) power density, operating at 80°C for the symmetric MEA comprised of 40% Pt/C SS-CCE versus 20% Pt/C SS-CCE, both with loadings of 0.2 mg _{Pt} /cm ²	37
Figure 3.8. EIS data interpreted to display a) Nyquist, b) capacitance and c) normalized capacitance plots for symmetric MEA comprised of 40% Pt/C SS-CCE versus 20% Pt/C SS-CCE, at operating cell temperatures of 30°C and 80°C and a DC bias of 0.425 V.	39
Figure 3.9. Comparison of EIS-derived data showing a) total resistance and b) limiting capacitance for the symmetric MEA comprised of 40% Pt/C SS-CCE versus 20% Pt/C SS-CCE at cell operating temperatures of 30 °C and 80 °C.	40
Figure 3.10. Cyclic voltammetry of symmetric MEAs with 40% Pt/C SS-CCE and NBE tested at room temperature under conditions of H ₂ (g) at the anode and N ₂ (g) at the cathode.....	41
Figure 3.11. EIS of symmetric MEAs with 40% Pt/C SS-CCE and NBE tested at room temperature under conditions of N ₂ (g) at the cathode and H ₂ (g) at the anode at DC bias of 0.425 V.....	43
Figure 3.12. Cyclic voltammetry of symmetric MEAs with 40% Pt/C SS-CCE and NBE tested at room temperature and 80 °C under conditions of N ₂ (g) at the cathode and H ₂ (g) at the anode at a sweep rate of 50 mV/s.	45

Figure 3.13. EIS of symmetric MEAs with 40% Pt/C SS-CCE and NBE tested at room temperature and 80°C under conditions of N ₂ (g) at the cathode and H ₂ (g) at the anode at a DC bias of 0.425 V.	47
Figure 3.14. Comparison of EIS-derived data showing a) total resistance and b) limiting capacitance for the symmetric MEA comprised of 40% Pt/C SS-CCE versus NBE at cell operating temperatures of 30 °C and 80 °C.	48
Figure 3.15. Cyclic voltammograms at 50mV/s for symmetric MEA tested at 80 °C made with 40% Pt/C a) NBE and b) SS-CCE tested at varying relative humidity with N ₂ (g) at the cathode and H ₂ (g) at the anode, with c) summarized ECSA data versus RH for each MEA.	50
Figure 3.16. EIS comparison for NBE tested at varying relative humidity in N ₂ (g) / H ₂ (g) configuration displaying only high RH a) Nyquist, b) capacitance and c) normalized capacitance plots measured at a DC bias of 0.425 V.	52
Figure 3.17. EIS comparison for SS-CCE tested at varying relative humidity in N ₂ (g) / H ₂ (g) configuration displaying only high RH a) Nyquist, b) capacitance and c) normalized capacitance plots measured at a DC bias of 0.425 V.	53
Figure 3.18. Comparison of EIS - derived data at a DC bias of 0.425 V and a cell temperature of 80 °C displaying the a) total resistance and b) limiting capacitance of symmetric MEAs with 40% Pt/C SS-CCE and NBE.	54

Figure 3.19. Performance curves of current density versus a) cell potential and b) power density for a symmetric MEA with 40% Pt/C NBE tested at varying relative humidity with O ₂ (g) at the cathode and H ₂ (g) at the anode at a cell temperature of 80 °C.....	56
Figure 3.20. Performance curves of current density versus a) cell potential and b) power density for a symmetric MEA with 40% Pt/C NBE tested at varying relative humidity with air at the cathode and H ₂ (g) at the anode at a cell temperature of 80 °C.	57
Figure 3.21. Polarization curve comparison of current densities for a symmetric MEA with 40% Pt/C SS-CCE tested at varying relative humidity with O ₂ (g) at the cathode and H ₂ (g) at the anode at a cell temperature of 80 °C.	59
Figure 3.22. Polarization curve comparison of current densities for a symmetric MEA with 40% Pt/C SS-CCE tested at varying relative humidity with air at the cathode and H ₂ (g) at the anode at a cell temperature of 80 °C.	60
Figure 3.23. Maximum power densities of symmetric MEAs with 40% Pt/C SS-CCE and NBE tested at an operating temperature of 80°C with 100% relative humidity comparing O ₂ (g) versus air at the cathode.....	61
Figure 3.24. Comparison between a) peak power density, and b) normalized peak power density with O ₂ (g) at the cathode. Along with c) peak power density, and d) normalized peak power density with air at the cathode. Tested in symmetric configuration using MEAs of 40% Pt/C SS-CCE, and NBE, tested at varying relative humidity with H ₂ (g) at the anode.....	63

Chapter 4. Studying Non-Vulcan Based Catalyst Support

Figure 4.1. Brunauer-Emmett-Teller analyses of OMC ₁₅ and Pt/OMC ₁₅ showing both adsorption (filled symbols) and desorption (open symbols) curves for measuring SSA.	
.....	67
Figure 4.2. OMC ₁₅ , Pt/OMC ₁₅ , and 20% Pt/Vulcan (commercial) a) thermograms and b) derivative thermograms to determine Pt loading and residual silica template.	69
Figure 4.3. Scanning electron microscopy images of Pt/OMC ₁₅ and 20% Pt/Vulcan (commercial).	70
Figure 4.4. Overlaid X-ray diffraction patterns of Vulcan (commercial), OMC ₁₅ , 20% Pt/Vulcan (commercial) and Pt/OMC ₁₅ , including Miller Indices of FCC Pt and graphitic C facets.....	72
Figure 4.5. Cyclic voltammograms at 100 mV/s in a three-electrode cell configuration with 20% Pt/Vulcan and Pt/OMC ₁₅ deposited on a glassy carbon WE, a Pt wire CE and a Hg-HgSO ₄ RE tested in N ₂ (g) purged 0.5 M H ₂ SO ₄	74
Figure 4.6. Linear sweep voltammograms at 5 mV/s and a rotation rate of 900 RPM in a three-electrode cell configuration with 20% Pt/Vulcan and Pt/OMC ₁₅ deposited on a glassy carbon WE, a Pt wire CE and a Hg-HgSO ₄ RE tested in N ₂ (g) purged H ₂ SO ₄	75
Figure 4.7. Cyclic voltammograms at 100 mV/s in a three-electrode cell configuration with a) 20% Pt/Vulcan and b) Pt/OMC ₁₅ deposited on a glassy carbon WE, a Pt wire CE and a Hg-HgSO ₄ RE tested throughout AST in N ₂ (g) purged H ₂ SO ₄	77
Figure 4.8. ESCA patterns at each CV cycle number with displays of a) ECSA in m ² /g _{Pt} , and b) percent decay from initial ECSA.....	78

Figure 4.9. EIS comparison for 20% Pt/Vulcan (commercial) tested throughout AST in a three-electrode configuration displaying a) Nyquist, b) capacitance, and c) normalized capacitance plots measured at a DC bias of 0.425 V.	80
Figure 4.10. EIS comparison for Pt/OMC ₁₅ tested throughout AST in a three-electrode configuration displaying a) Nyquist, b) capacitance, and c) normalized capacitance plots measured at a DC bias of 0.425 V.	81
Figure 4.11. Comparison of EIS - derived data at a DC bias of 0.425 V displaying the a) total resistance and b) limiting capacitance of both 20% Pt/Vulcan (commercial) and Pt/OMC ₁₅	82
Figure 4.12. Linear sweep voltammograms at 5 mV/s and a rotation rate of 900 RPM in a three-electrode cell configuration with 20% Pt/Vulcan and Pt/OMC ₁₅ deposited on a glassy carbon WE, a Pt wire CE and a Hg-HgSO ₄ RE tested before and after AST in N ₂ (g) purged H ₂ SO ₄	84

LIST OF ABBREVIATIONS AND SYMBOLS

λ	Wavelength
θ	Angle
AST	Accelerated stress testing
BET	Brunauer-Emmett-Teller
BJH	Barrett-Joyner-Halenda
CCE	Ceramic carbon electrode
CE	Counter electrode
CL	Catalyst layer
CNT	Carbon nanotube
CV	Cyclic voltammetry
D.I.	Deionized
DC	Direct current
DMFC	Direct methanol fuel cell
DTG	Derivative thermogram
ECSA	Electrochemically active surface area
EDX	Energy dispersive X-ray
EG	Ethylene glycol
EIS	Electrochemical impedance spectroscopy
FCC	Face centered cubic
FCEV	Fuel cell electric vehicle
FCT	Fuel Cell Technologies, Inc.

FRA	Frequency response analyzer
GDE	Gas diffusion electrode
GDL	Gas diffusion layer
GHG	Greenhouse Gas
HC	Hydrocarbon
IPA	Isopropyl alcohol
IUPAC	International Union of Pure and Applied Chemistry
LSV	Linear sweep voltammetry
MEA	Membrane electrode assembly
MPL	Microporous layer
NBE	Nafion®-based electrodes
NP	Nanoparticle
OMC	Ordered mesoporous carbon
ORR	Oxygen reduction reaction
PEM	Proton exchange membrane
PEMFC	Proton exchange membrane fuel cell
PFSA	Perfluorosulfonic acid
®	Trademark registration symbol
RDE	Rotating disk voltammetry
RE	Reference electrode
RH	Relative Humidity
RHE	Reversible hydrogen electrode
R_{Σ}	Total resistance

SBA	Mesoporous silica
SEM	Scanning electron microscopy
SSA	Specific surface area
SS-CCE	Sulfonated-silica ceramic carbon electrode
TEOS	Tetra ethyl orthosilicate
TGA	Thermogravimetric analysis
™	Trademark symbol

Chapter 1. Introduction

1.1 Background

Less than 40 years after the battery was invented by Alessandro Volta, the first fuel cell was developed by a Welsh scientist, Sir William Robert Grove.¹ In 1842, Grove discovered the constituent of current fuel cell electrodes, the use of platinum. After many decades of study, the fuel cell started making progress in the 1960's, where phenomena, including difficulty with high temperature operations and cathode reaction limitations, were becoming understood and further studied. To date, the same limitations are the primary focus of research, along with the continuous attempt to reduce overall cost.

Throughout the past few decades, there has been a considerable amount of research towards clean energy production, with one being hydrogen power.^{2,3} Hydrogen is one of the main fuel sources used in the proton exchange membrane fuel cell (PEMFC). Creating sustainable, clean electricity is a major benefit of the fuel cell allowing it to be implemented in products such as automobiles, public transit vehicles and industrial equipment.⁴⁻⁶ The fuel cell shows great promise in being a low-greenhouse gas (GHG) emitting energy source, that cooperates within the terms of the 2016 Paris Agreement. This agreement was written to act as a global response towards climate change. The three main points of interest that this agreement includes:⁷

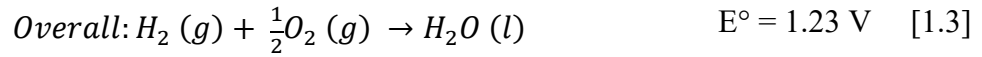
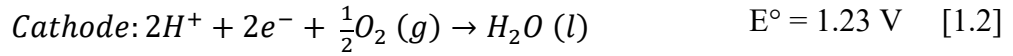
1. Holding the average global temperature increase well below that of 2 °C;
2. Placing adaptation programs for the future climate, as well as implementing further development to reduce production of greenhouse gases; and
3. Ensuring consistent financial flow towards the path of climate-resilient and low GHG development.

Although this agreement does not ensure global cooperation, it does bring awareness to the fact that succumbing to the threat of climate change has become a global realization. With that, we must be willing to work together in order to reduce the amount of GHG produced, as well as bring innovative ideas to surface, such as climate engineering, to fight this challenge.⁷⁻⁹ Roughly one third of the GHG emissions can be attributed to the transportation sector, with the largest emitter being the automobile.¹⁰ Around the world, goals have been set in order to reduce GHG emissions, which includes increased use of renewable resources and improved energy efficiencies, where possible. In order to comply to these efforts, the PEMFC is a promising replacement of current internal combustion engines used in automobiles. With more than two-times greater efficiency, fuel cells have potential for an increase of more than 80% efficiency for the heat and power systems, combined.¹¹

Despite continuous efforts over the years, the first PEMFC automobile wasn't produced until 1993, and commercialization did not occur until 2008, with the Hyundai Tucson/iX35 fuel cell electric vehicle (FCEV).¹⁰ From there, the FCEV has been put into production at numerous automobile companies, all using unique technology, in search of a more efficient and less expensive option. Although there is promise for improved catalysts and ionomers, state-of-the-art assemblies continue to use high-cost materials, including Pt and perfluorosulfonated ionomers, such as Nafion®.¹² The United States Department of Energy declared a target for FCEVs to have a durability of up to 5000 hours by 2025, which is equivalent to a lifetime of ca. 240,000 km.¹³ Therefore, efforts must continue to seek for more efficient and less expensive materials in the PEMFC.

1.2 The Proton Exchange Membrane Fuel Cell (PEMFC)

The fuel cell is a device used to convert chemical energy into electrical energy where Equations 1.1 and 1.2 describe the use of hydrogen and oxygen gasses in the device. The proton exchange membrane fuel cell (PEMFC) is a clean energy device because there are zero carbon emissions and, as seen in Equation 1.3, the only by-product is water.



The fuel cell is a device that converts chemical potential energy into electrical energy through use of hydrogen and oxygen redox reactions. Though there is a wide variety of fuel cell devices, the PEMFC has received the greatest attention. This configuration uses hydrogen and oxygen gases to produce electricity, with water, and some heat, as waste by-products. In this research, there are three main components of the PEMFC that are of interest; the anode, the cathode and the proton exchange membrane, also known as the membrane electrode assembly (MEA).

As seen in Figure 1.1, $H_2(g)$ is oxidized into protons and electrons at the anode, and $O_2(g)$ is reduced to produce water, at the cathode. The oxygen reduction reaction (ORR) is known as the “sluggish” reaction of the PEMFC due to poor reaction kinetics that lead to high overpotentials^{14,15}. Overpotential is the difference between theoretical and actual

potentials for an oxidation or reduction reaction, of which with lower overpotential comes more favourable redox reactions.

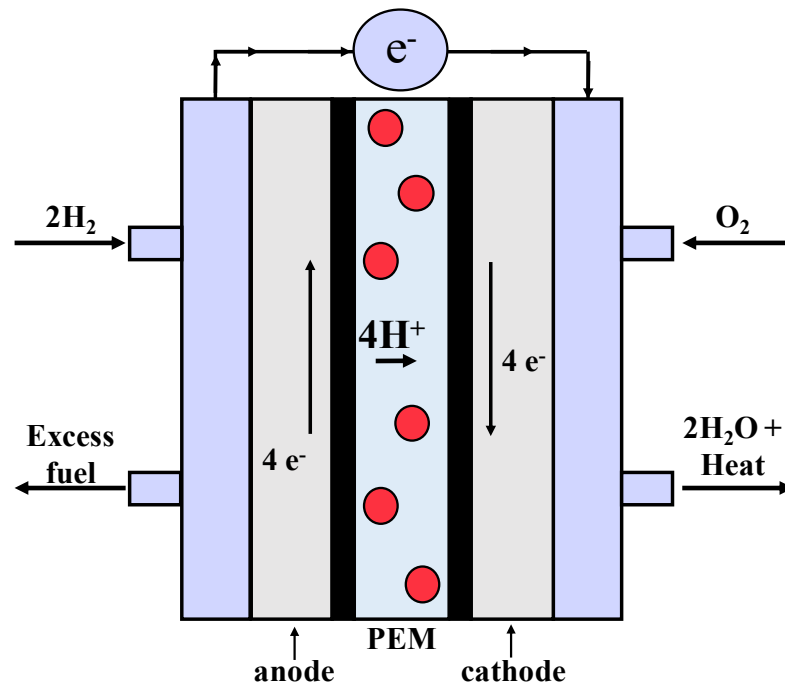


Figure 1.1. Schematic diagram of the proton exchange membrane fuel cell device.

1.3 The Membrane Electrode Assembly (MEA)

As seen in Figure 1.2, the membrane electrode assembly (MEA) is comprised of two electrodes and a membrane, typically a perfluorsulfonic acid membrane. The two electrodes, an anode and cathode, are layered on either side of the membrane.

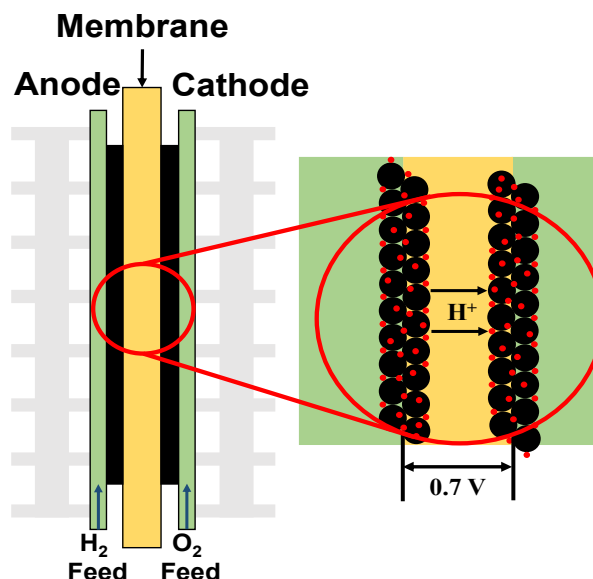


Figure 1.2. Schematic diagram of the membrane electrode assembly (MEA) in a PEMFC.¹⁶

1.3.1 The Proton Exchange Membrane (PEM)

The most common material used as a proton exchange membrane (PEM) is perfluorosulfonic acid (PFSA), with Nafion[®] being the most common. Also known as a polymer electrolyte membrane, Nafion[®] is widely used due to its durability and high proton conductivity.¹⁷ Seen in Figure 1.6 a), Nafion[®] has three main components: a Teflon[™] backbone, a perfluoro-ether sidechain and a sulfonic acid head group. Although variations of the Nafion[®] membrane have been studied, there remains set-backs including high cost and reactant gas crossover. The expense is primarily due to the use of fluorine, a very dangerous material, and reactant gas crossover is linked to membrane decomposition. Studies have shown that Nafion[®] membranes decrease in thickness, after testing, due to loss of fluoride ions and small organic compounds.¹⁸

In the past decade, several Nafion[®] alternatives have been studied, with a large amount of interest being put into a hydrocarbon membrane. Nafion[®]-polyvinyl alcohol complexes have shown promise towards the direct methanol fuel cell (DMFC)¹⁹. Nafion[®] tends to have a high permeability of methanol, but studies of these Nafion[®]-hydrocarbon hybrids have displayed methanol resistance and increased proton conductivity.¹⁹ Sulfonated hydrocarbon membranes generally have poor stability, but, after modification, they have been able to show high durability throughout accelerated stress testing, while maintaining high proton conductivity.¹⁷ Lastly, phosphorylated hydrocarbon membranes using lignin, one of the most abundant polymers in nature, have shown promise in high temperature fuel cells.²⁰

Although alternative materials have shown increased stability, while maintaining conductivity, the leading PEM remains to be Nafion[®]. Being that it can be produced at different thicknesses for use in specific fuel cell configurations, Nafion[®] has enough versatility, with its high durability and great proton conductivity, to remain at the top for PEMs in a range of fuel cell devices.

1.3.2 Electrode Materials

The PEMFC electrode consists of three components: the gas diffusion layer (GDL), a microporous layer (MPL), and the catalyst layer (CL), seen in Figure 1.3. Improvement in fuel cell electrode materials has been of interest in order to, both, increase performance, and decrease overall cost of fuel cell devices. One particular limitation is the use of expensive, and precious, platinum within the CL.

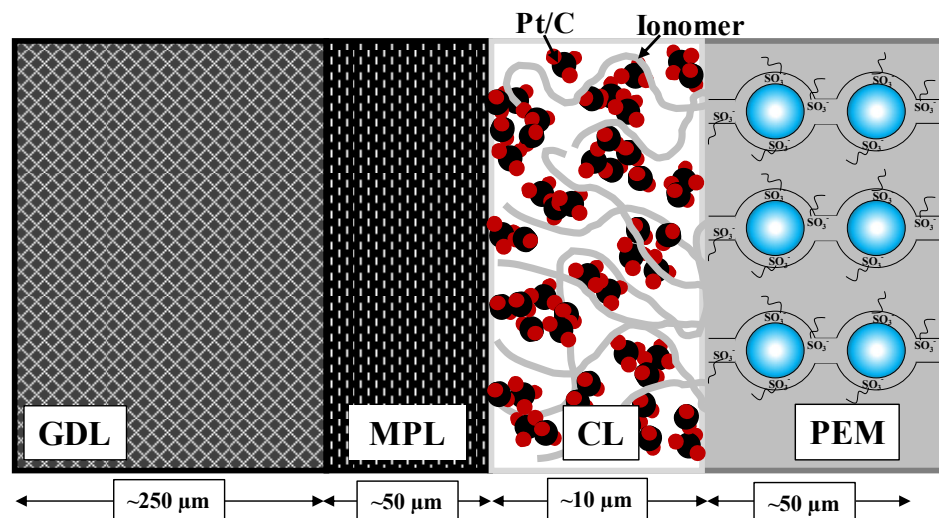


Figure 1.3. Representation of a typical PEMFC electrode (not to scale).

Each layer of the PEMFC electrode contains pertinent elements for overall functionality. The GDL is ca. 300 μm thick and made from carbon fiber (e.g. carbon cloth or carbon paper) and the MPL. This layer allows for efficient diffusion of reactant gasses, and has some permeability of water to reduce chances of flooding. Flooding occurs at the cathode, where water is a by-product. Materials with high water retention are able to support the water uptake and reduce chances of flooding complications. The MPL contains a blend of TeflonTM and carbon black, creating a porous hydrophobic layer between the GDL and CL, which assists with water management. The final component of a PEMFC electrode is the CL, which is typically ca. 10 μm thick. Both gasses and ions must be permeable through the CL and so large pores, between the catalyst agglomerates, as well as small pores, and an ionomer binder, are crucial for mass and ion transport. Once reactants reach the catalyst layer, the electrochemical reactions, and the basis of the device, begin to take place.

1.3.3 PEMFC Catalyst Layer

The catalyst layer is the porous 3-dimensional layer where the electrochemical reactions take place. As seen in Figure 1.4, it consists of a catalytically active metal, usually platinum, deposited onto a conductive support, typically carbon. The wt % of Pt deposited on the support ranges from 10 - 60%, with the most typical being 20% Pt/C, all of which can be purchased commercially or generated in-house. The catalyst is thoroughly mixed with an ionomer, in a water-alcohol dispersion media, to produce a catalyst ink. The ink can then be deposited onto the desired substrate. For MEA fabrication, this is done by spray coating, or casting, onto either the GDL, to create a gas diffusion electrode (GDE) or the membrane, making what is known as a catalyst-coated membrane.

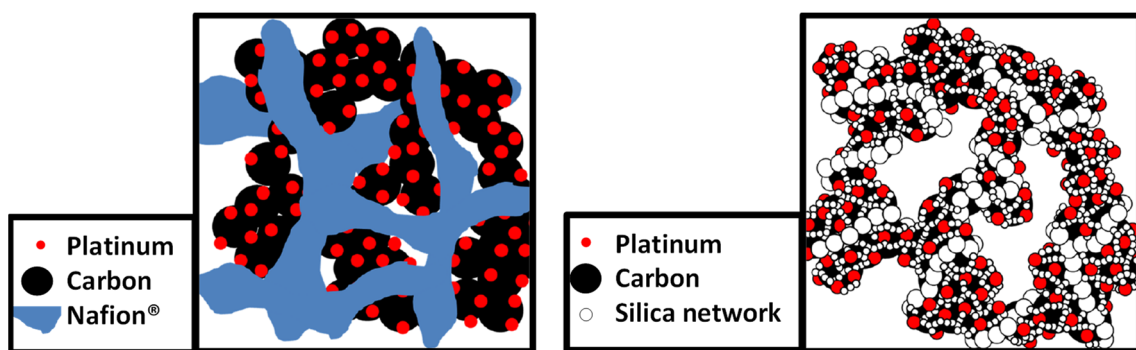


Figure 1.4. Diagram comparing a Nafion®-based and a sulfonated-silica ceramic carbon electrode CL, adapted from Alipour et al.²¹

1.4 PEMFC Catalyst Support

Carbon is the most common catalyst support due to its suitable conductivity and porosity. Carbon supports can be found in many different morphologies, including graphene, carbon nanotube (CNT) and carbon black. Most commonly, carbon black materials are used as catalyst supports which include Vulcan and Ketjen, each with unique physical and electrochemical properties. Carbon blacks are generally spherical nanoparticles, ranging in size from 30 to 1000 nm, and may have micro and mesoporosity.

Alternatives to carbon black supports have become of great interest in recent years due to limitations on carbon blacks, including corrosion mechanisms and poor utilization of the Pt catalyst.²² Graphene, for example, has proven to have high surface area and promising thermal stability and electrical conductivity.^{23,24} These characteristics are important for good catalyst dispersion and high durability, which when functionalized with heteroatoms can be even more beneficial to allow for uniform catalyst dispersion and greater catalyst utilization. Graphene is a single layer sheet of sp^2 -hybridized carbon atoms, which can be altered in small ways to change the morphology and produce materials with intrinsic differences. When layered, graphene can be converted into graphite, if rolled into a cylinder it can be made into CNTs and when wrapped up in a sphere it is a fullerene, i.e. a spherical Buckyball.²⁴

Aside from novel carbon structures, recent studies have been geared towards removing carbon from the catalyst layer altogether. Novel metal oxide supports with enhanced electronic conductivity have shown great promise as a PEMFC catalyst support, showing high performance and high durability.²⁵

1.4.1 Ordered Mesoporous Carbon (OMC)

Typical fuel cell catalysts are comprised of Pt deposited onto a carbon black material, such as Vulcan or Ketjenblack. Carbon is among the more common supportive materials due to its suitable physical and electrochemical properties. These properties can be finely tuned depending on the type of carbon material used.^{26–28} Ordered mesoporous carbon (OMC) is a material that obtains large specific surface area (SSA) and tunable pore sizes. Using a fairly straight-forward “nanocasting” approach, i.e. the hard-templating method shown in Figure 1.5,²⁹ they obtain mesopores which range from 2 - 50 nm in diameter and SSAs of 1000 m² g⁻¹ and higher.³⁰ The tunable properties along with high conductivity makes these materials suitable for numerous applications, including adsorption, gas storage, biosensing, selective sensing, batteries, supercapacitors, and fuel cells.^{29,31–33}

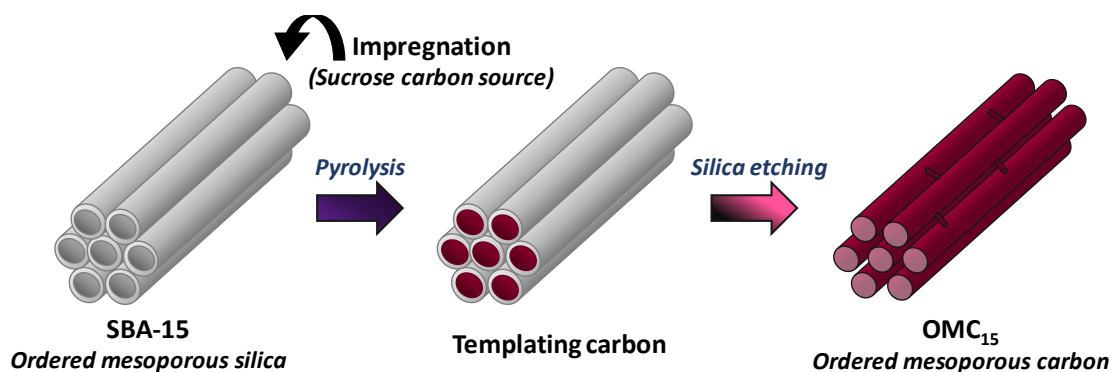


Figure 1.5. Display of steps for hard-templating method for synthesis of OMC₁₅.

The hard-templating method starts with the synthesis of a mesoporous silica, in this research SBA-15. This occurs through reactions between a nonionic surfactant, Pluronic® P123, a cationic co-surfactant, cetyl trimethylammonium bromide, and a silica precursor,

tetra ethyl orthosilicate (TEOS). To synthesize the two-dimensional OMC₁₅, a sucrose solution, mixed with H₂SO₄ (aq) as the carbonization agent, is put through a series of heating steps before obtaining the final product.²⁷ One focus of this project includes the incorporation of OMC₁₅ as a catalyst support. Due to large pores within OMC₁₅, it is envisioned that there will be better gas transport, as well as water retention, at the cathode, where flooding prominently occurs.³⁴ The larger pores will, presumably, allow for increased interaction between Pt and the ionomer which would increase oxygen reduction reaction (ORR) kinetics.

OMC₁₅ has been shown to exhibit greater catalytic activity when compared to other carbon blacks.^{27,34–36} This is likely due to the materials high surface area and large number of mesopores, which allow for a more uniform Pt dispersion. Two-dimensional OMC₁₅ is the morphology of most interest for this work, and has shown promising ORR performance seen in previous studies.³⁴

1.5 Ceramic Carbon Electrodes

A limitation of typical PEMFC CLs also includes the use of an expensive PFSA ionomer, Nafion[®]. Not only does Nafion[®] increase costs, but it is permeable to methanol, which reduces DMFC performance, and has a glass transition temperature at 90 – 110 °C, making it unusable at the preferred temperatures within automotive applications.^{12,17} Similar to alternative PEM materials, hydrocarbon-based (HC) ionomers, have been studied as a Nafion[®] replacement in the CL. Although HC ionomers show promise at moderate temperature, and relative humidity (RH), there remains challenges where they appear to be much more sensitive to RH change.^{37,38}

A growing interest has been placed upon a different type of electrode structure, the ceramic carbon electrode (CCE). Typically, a CCE is made by mixing a silicon alkoxide precursor (e.g. TEOS) with water. A hydrolysis reaction occurs when the reactants are in a mutual solvent media, generally methanol or isopropanol. When hydrolysis occurs, the silica precursor is converted into orthosilicic acid, $\text{Si}(\text{OH})_4$. Two silicic acid monomers can undergo a condensation reaction, with each other, forming a siloxane group, Si-O-Si .³⁹⁻⁴¹ This ethoxy bond is the basis of cross-linked polymeric growth that creates the silicate structure. The reaction can take place in either acid or based-catalyzed conditions. When this reaction occurs in the presence of carbon black (or Pt/C), the carbon is encapsulated into silicate matrix, creating a composite material which is referred to as a CCE. This type of electrode is shown to be rigid with high porosity and can be easily modified, depending on specific electrochemical demands.³⁹

For fuel cell applications, the CCE effectively replaces the CL Nafion[®] ionomer with a silica-based polymer mixture. CCEs have displayed increased durability and high surface area, due to the ceramic binder that is formed through a sol-gel process.^{39,42-44} The term sol-gel describes the specific process used to create a broad range of gels that are produced from colloidal suspensions, i.e. sols.⁴³ Sol-gel production has been widely studied, with tunable factors such as pH, temperature and reaction time, being a few examples, that allow for synthesis of very specific products.^{40,41} With the ability to fine-tune reaction parameters, to yield any given product, this process is widely used for application in numerous fields.

The CCE has demonstrated activity in biosensors, ion-selective electrodes, pH sensors and fuel cells.³⁹ Anderson et al. continued the CCE synthetic process by adding the silica sol-gel to the catalyst material, typically Pt/C, to form a composite aerogel.⁴² The

composite gel underwent ageing, heating and annealing before being dried into powder form. The powder was mixed with acetone and deposited onto a carbon-film support, to undergo fuel cell tests.⁴² Tests concluded that CCEs had potential to become a strong contender as a fuel cell ionomer, and the ability to be chemically modified only amplified that possibility. In a novel approach, Eastcott et al. synthesized the CCE in a one-pot method in order to enhance distribution of the ionomer on the catalyst support.⁴⁴ The TEOS precursor was added in monomer form to the solvent mixture containing Pt/C.⁴⁴⁻⁴⁷ After mixing for the prescribed time, the material was tested and showed promise for the high temperature fuel cell due to its great water retention capabilities.⁴⁴

1.5.1 Sulfonated-Silica Ceramic Carbon Electrode (SS-CCE)

After much research, the CCE underwent a rather spectacular transformation in the Easton group, creating the sulfonated-silica ceramic carbon electrode (SS-CCE). The monomer, TEOS, that underwent the polymerization reaction, for the CCE, was no longer the only silica precursor. A combination of TEOS and 3-trihydroxysilyl-1-propanesulfonic acid (TPS) monomers were used to form the SS-CCE polymer network. As seen in Figure 1.6, the SS-CCE materials obtain similar features to the commercial standard, Nafion[®], including the ether and the sulfonic acid groups. The TEOS to TPS mole ratio had previously been optimized to be 95:5, with a total silane loading of 35 wt%, when employed with a 20% Pt/C commercial catalyst.⁴⁵

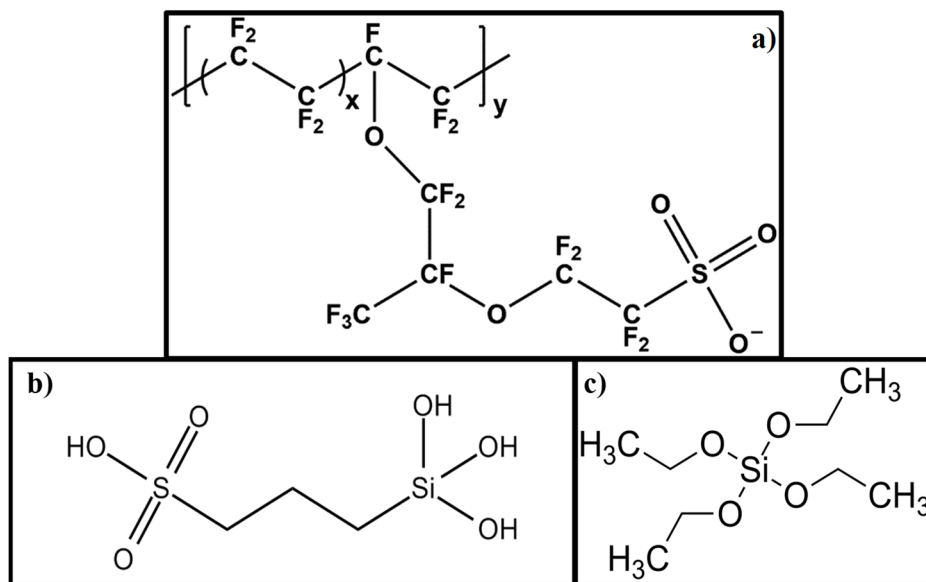


Figure 1.6. Chemical structures of a) Nafion[®], b) TPS, and c) TEOS.

Typical PEMFC catalysts, comprised of Pt/C mixed with Nafion[®], have poor durability; this is an area that SS-CCEs have shown to be better, for the PEMFC.^{21,48} This increase in durability can be attributed to mixing the ionomer in monomer form. This allows an ionomer network to grow around the Pt/C particles, and works as the ionomer, binder, and catalyst stabilizer. High water retention has been noted when testing the SS-CCE, which allows for greater stability when running at high operating temperatures and low relative humidity.⁴⁹

1.6 Objectives

Improving fuel cell electrode materials is required to increase performance and decrease cost of fuel cell devices. One particular limitation is the use of precious platinum within the catalyst layer. In this work, one focus is to work with 40 wt% Pt/C, at loadings

of $0.2 \text{ mg}_{\text{Pt}} \text{ cm}^{-2}$, with the hypothesis of a thinner catalyst layer that will increase reactant transport while reducing cost by lowering Pt mass required. In the past, only 20% Pt/Vulcan catalysts have been studied in the SS-CCE and have shown great durability with similar activity to commercial standards. A limitation of commercial standards includes the use of an expensive PFSA ionomer, Nafion[®]. SS-CCEs have demonstrated their ability to eliminate the use of Nafion[®] within the catalyst layer.⁴⁹ Previous work within this group, using 20 wt% Pt/C, has shown that a stoichiometric ratio of a silicate with a sulfonated organosilane can act as the ionomer/ binder, at a fraction of the cost of Nafion[®].⁴⁶ Due to the lower carbon content in 40 wt% Pt/C catalysts, the silane ratio must be optimized for enhanced fuel cell performance.

This work includes the synthesis, preparation, and PEMFC testing of 40% Pt/C SS-CCEs. Fuel cell performance and electroactivity will be tested against comparators, 40% Pt/C Nafion[®]-bound electrode (NBE) and 20% Pt/C SS-CCE. Using a 40 wt% Pt/C catalyst, it is predicted to have increased fuel cell performance due to thinner catalyst layers and the higher Pt-to-C ratio. This reduces the amount of carbon that could corrode throughout the duration of testing, as well as increases water retention, even further, and mass and ion transport.

The use of OMC₁₅ as a support should increase the ORR kinetics and reduce chances of flooding at the cathode. It also exhibits greater catalytic activity when compared to other carbon black materials, which is likely due to its high surface area and mesoporosity, allowing for a more uniform Pt dispersion.⁵⁰ Two-dimensional and three-dimensional OMC (OMC₁₅ and OMC₁₆, respectively) have shown promising ORR performance, which can be implemented in the PEMFC. This work displays activity of only Pt/OMC₁₅ catalysts.

Chapter 2. Experimental Synthesis and Characterization Techniques

2.1 Synthesis and Preparation of SS-CCE

The sulfonated silica ceramic carbon electrode (SS-CCE) was fabricated by first making a sol-gel mixture that was then deposited onto the gas diffusion layer (GDL). In a 150 mL beaker, 0.26 g of tetraethyl orthosilicate (98% TEOS, Sigma Aldrich), 0.03 g of 3-(trihydroxysilyl)-1-propanesulfonic acid (35% TPS, Gelest Inc.) and 4.3 μL of 6 M ammonium hydroxide (30%, Sigma Aldrich) were added together and rapidly stirred on a stir plate for 10 minutes. This mixture was added dropwise to 166.7 mg of 40 wt % Pt/C (40 wt% Pt on Vulcan XC-72, Premetek Co.), 6.2 g of deionized (D.I.) water and 0.6 g of methanol (99%, ACP Chemicals). The catalyst mixture was partially covered with Parafilm[®] M, sonicated for 10 minutes, then left to stir for 72 hours.

While the sol-gel mixture was stirring, the gas diffusion layer (GDL) was prepared for spray deposition of the catalyst layer (CL). A piece of commercial carbon paper (Sigracet 29 BC, Fuel Cell Store) that obtained a microporous layer (MPL) was cut to a specific measured area. Before deposition of the SS-CCE sol-gel, 29 BC was dusted with a very low loading of Nafion[®] (5 wt%, Ion Power), at ca. 0.018 mg/cm^2 , to increase hydrophilicity of the surface. Once the GDL was dry, the SS-CCE sol-gel ink was air brushed onto the surface until a total Pt loading of 0.2 mg cm^{-2} was achieved. To drive the SS-CCE polymerization reaction to completion, the sprayed electrode was dried in the oven at 120°C for 1 hour. Excess catalyst ink was also left to dry in the oven to be used for compositional analyses of the catalyst layer.

2.2 Fabrication of Nafion[®]-Bound Electrodes

For comparison, a mixture containing Nafion[®] as the ionomer and binder was also prepared. First, 670.2 mg of 5 wt% Nafion[®], 10 g of D.I. water and 2.5 g of isopropyl alcohol (IPA \geq 99.5%, Fisher Scientific) were added to a 150 mL beaker and stirred. In a separate 250 mL beaker, 142.9 mg of 40 wt % Pt/C (40 wt% Pt on Vulcan XC-72, Premetek Co.) and 3.0 g of D.I. water was stirred while slowly adding the Nafion[®], D.I. water, and IPA mixture. This mixture was vigorously stirred for 2 hours, sonicated for 1 hour, then left to stir for 24 hours, after covering the beaker with Parafilm[®] M to avoid loss of volatiles.

A similar procedure was carried out for fabrication of the Nafion[®]-bound electrode (NBE), as to the SS-CCE, except there was no dusting of Nafion[®] before spray deposition, and the sprayed electrode was cured at 90 °C, which is low enough to avoid decomposition, for 1 hour.

2.3 Synthesis of Pt/ OMC₁₅

2.3.1 Synthesis of OMC₁₅ using the Silica Template

In a 50 mL beaker, 1.25 g of sucrose (\geq 99.5%, Sigma Aldrich) was dissolved in 0.14 g of sulfuric acid (98%, ACP Chemicals) and 5.0 g of D.I. water and mixed with 18.1 mg of boric acid ($\text{H}_3\text{BO}_3 \geq$ 99.5%, Sigma Aldrich). In a separate 150 mL beaker, the sucrose solution was added dropwise to 1.0 g of SBA-15, stirred until uniform and heated to 100 °C for 2 hr. The mesoporous silica template, SBA-15, was supplied by Dr. A.H.A. Monteverde Videla of Politecnico di Torino and was synthesized using a method adapted from Zhao et al.⁵¹

The sample was left to dry over night before adding another dose of sucrose solution, at 70 wt% concentration, to ensure all pores were filled. The heating procedure was repeated before pyrolyzing the product at 900 °C for 3 hr in a tube furnace. The silica template was etched away using 30 mL of hydrofluoric acid (≥ 48 wt%, Sigma Aldrich). The left over OMC₁₅ was washed, until neutral pH, and dried at ~ 110 °C for 3 hr. Synthesis of OMC₁₅ adapted from Zeng et al.⁵⁰

2.3.2 Platinum Deposition onto OMC₁₅

To deposit a target of 20 wt% Pt onto OMC₁₅, the microwave-assisted polyol method⁵² was performed by adding 42.0 mg of chloroplatinic salt ($\text{H}_2\text{Cl}_6\text{Pt} \cdot \text{H}_2\text{O} \geq 99.9\%$, Sigma Aldrich) and ca. 75 mL of ethylene glycol (EG, Sigma Aldrich) to a 250 mL beaker. To that beaker, 82.2 mg of OMC₁₅ was added then stirred for 10 minutes. With 0.1 M sodium hydroxide (NaOH > 95%, Fisher Scientific), the pH was adjusted to 9.5 followed by sonication of the mixture for 30 minutes. The pH was again adjusted to 9.5 with 0.1 M NaOH before microwaving the reaction mixture on high power for 2 minutes. The beaker was covered with Parafilm[®] M and left to cool over night, while stirring. The EG was gravity filtered off of the Pt/ OMC₁₅, which was then washed three times each with D.I. water and acetone. The final Pt/ OMC₁₅ catalyst was dried at 80 °C over night.

2.3.3 Preparation of Pt/ OMC₁₅ Ink and Electrode

To be able to test the catalyst electrochemically, 8.0 mg of the catalyst powder was added to a mixture of 30 μL Nafion[®] (5 wt%, Ion Power), 400 μL of D.I. water and 200

μL of IPA. The mixture was sonicated for 45 minutes until uniform, then 4 μL of the ink was drop-coat deposited onto a 5 mm glassy carbon rotating disk electrode (RDE, Pine instruments) for three-electrode testing.

For comparison, commercial catalyst 20 wt % Pt/C (20 wt% Pt on Vulcan XC-72, Premetek Co.) was used to make an ink of similar Pt loading to be tested electrochemically.

2.4 Materials Characterization Techniques

Each catalyst was physically characterized to obtain compositional and morphological analyses.

2.4.1 Thermogravimetric Analyses (TGA)

Thermogravimetric analyses (TGA) were performed on a TA Instruments SDT Q600 to determine composition through analysis of mass loss at specific temperatures. Samples that were comprised of Vulcan carbon were tested under 50 mL/min of extra dry air at a ramp rate of 20 $^{\circ}\text{C}/\text{min}$, to a temperature of 1000 $^{\circ}\text{C}$. Samples made with OMC₁₅ were tested under 50 mL/min of extra dry air at a ramp rate of 2 $^{\circ}\text{C}/\text{min}$, to reduce sample loss, to a temperature of 1000 $^{\circ}\text{C}$. All data was analyzed using TA Thermal Advantage software, including derivative thermograms (DTG) which displays the derivative of wt % loss, relative to temperature.

2.4.2 Brunauer-Emmett-Teller (BET) Surface Area and Pore Size Analyses

The Brunauer-Emmett-Teller (BET) surface areas and Barrett-Joyner-Halenda (BJH) pore sizes of each sample were measured using Quantachrome Instruments NOVA 1200e Surface Area & Pore Size Analyzer. All samples were measured under N₂ atmosphere at 77 K, after being degassed at 200 °C for 6 hours. Approximately 160 data points were collected for adsorption/ desorption isotherms. The relative pressure in the system was allowed to equilibrate for at least 70 seconds before a data point was recorded. All data, including BET surface area and BJH pore size distributions, was analyzed using NovaWin software.

2.4.3 Scanning Electron Microscopy (SEM) and Energy Dispersive X-Ray

Spectroscopy (EDX)

All samples were imaged using a Hitachi FlexSEM 1000 system with an energy dispersive X-ray (EDX) analyzer. Powder samples were coated onto aluminum sample holders using graphite ink, whereas GDE's were placed on top of double-sided carbon paper to be attached to the sample holder. Each sample was electron imaged at a working distance of 5 mm, whereas EDX spectra were measured at 10 mm.

2.4.4 X-Ray Diffraction (XRD)

For compositional determination, an X-ray diffractometer (Rigaku Ultima IV) was used with a Cu K α radiation source ($\lambda = 0.15418$ nm). Samples were tested at operating conditions of 10 kV and 44 mA from $2\theta = 10^\circ$ through to 100° . Powder samples were

prepared by evenly filling and pressing them into XRD zero-background sample holders and placing in an automated ten sample attachment. All data was analyzed using PANalytical X'Pert HighScore software. Average Pt crystallite sizes were estimated using the Scherrer equation (Equation 2.1).

$$D = \frac{K\lambda}{\beta \cos\theta} \quad [2.1]$$

Where D is the true crystallite size, K is the Scherrer constant (for full width half max (FWHM) measurements, K = 0.94), λ is the X-ray wavelength, β is FWHM in radians and θ is Bragg's diffraction angle in degrees.

2.5 Electrochemical Measurements

All catalyst samples were electrochemically tested using a Pine Instruments WaveDriver 20 coupled with the MSR electrode rotator and/ or a Solartron 1470 multichannel potentiostat coupled with a Solartron 1260 frequency response analyzer (FRA).

2.5.1 Three- Electrode Testing for OMC₁₅ Catalysts

A rotating disk electrode (RDE) was used with the Pine potentiostat to measure cyclic voltammetry (CV) and linear sweep voltammetry (LSV), which was used to measure oxygen reduction reaction (ORR) activity. The Solartron instrument was used for accelerated stress testing (AST) measurements, which included CV and electrochemical impedance spectroscopy (EIS).

2.5.1.1 Cyclic Voltammetry (CV)

Three-electrode tests were studied at room temperature in N₂-purged 0.5 M H₂SO₄ (aq) (98%, Fisher Scientific) electrolyte. Seen in Figure 2.1, a glassy carbon electrode (area = 0.196 cm²) with catalyst ink deposited acted as the working electrode, a Pt wire was the counter electrode and a mercury/ mercury sulfate reference electrode (Bioanalytical Systems, Inc.) was used to measure catalytic activity. The reference electrode was calibrated to be ca. 701 mV vs reversible hydrogen electrode (RHE) by measuring the electrode's potential in H₂-purged 0.5 M H₂SO₄.

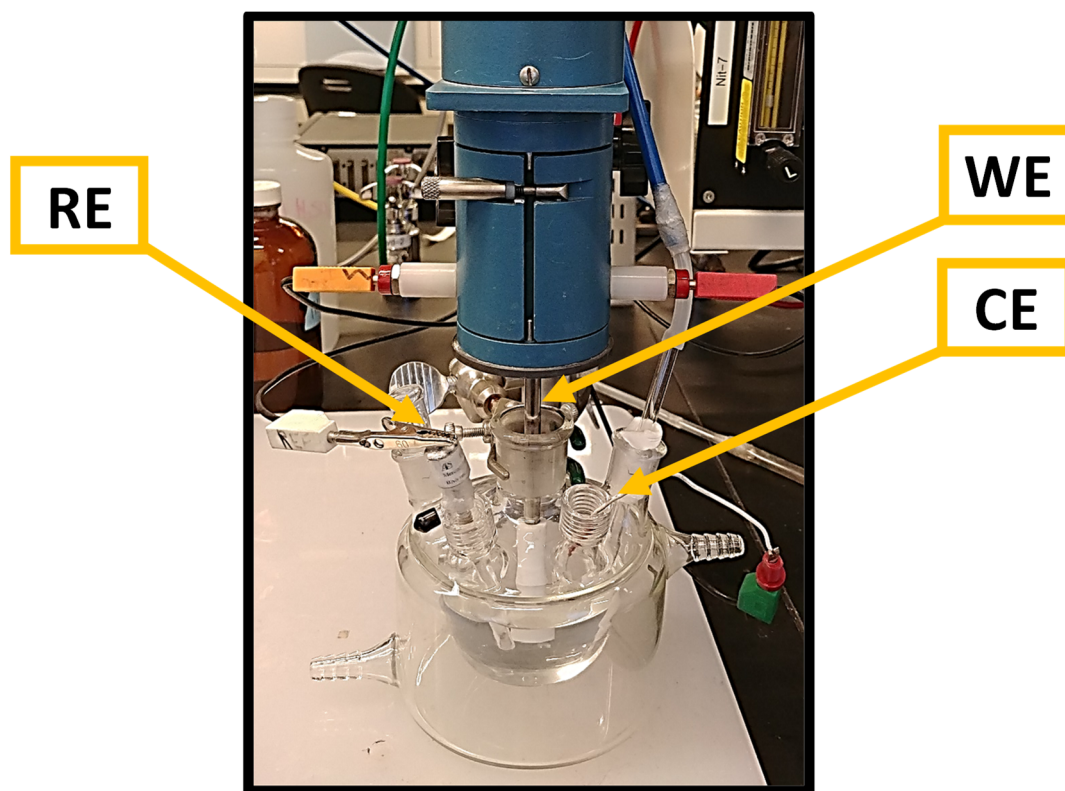


Figure 2.1. Three-electrode set up on the Pine Instruments potentiostat showing the reference electrode (RE), the counter electrode (CE), and the working electrode (WE) in contact with the MSR rotator.

Cyclic voltammograms were collected at 100 mV/s to obtain the electrochemically active surface area (ECSA) of Pt within the tested catalyst layers. The area under the H₂-desorption region (Figure 2.2) was integrated using AfterMath software to find charge, which was then translated into surface area of Pt using the previously determined constant of 210 $\mu\text{C cm}^{-2}\text{Pt}$.

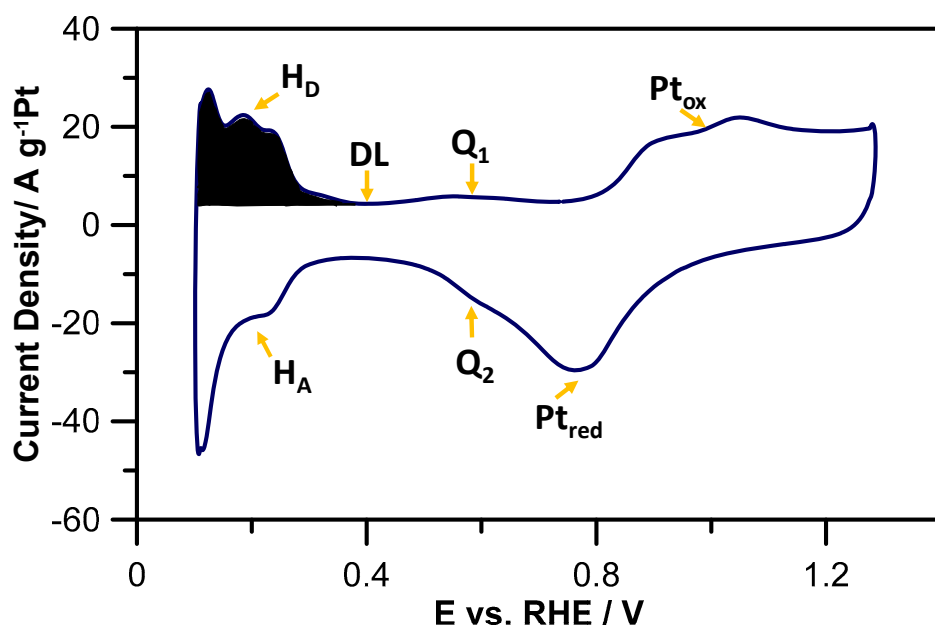


Figure 2.2. Example cyclic voltammogram of 20 wt% Pt/C (Johnson Matthey) in 0.5 M H₂SO₄ at 20 mV/s displaying characteristic features of a Pt cyclic voltammogram.

The regions labelled H_D and H_A, in Figure 2.2, are characteristic of hydrogen desorbing and adsorbing on the Pt surface, respectively. The region labelled DL shows the electrical double layer of the system, and Q_{1&2} show the redox reactions of the hydroquinone/ quinone within the carbon support. Finally, the regions labelled Pt_{ox} and Pt_{red} are characteristic of Pt oxide formation and removal on the surface of the catalyst layer.

2.5.1.2 Electrochemical Impedance Spectroscopy (EIS)

Electrochemical impedance spectroscopy (EIS) was measured using the Solartron potentiostat/ FRA system, with the electrolyte being N₂-purged 0.5 M H₂SO₄ (aq), in the configuration seen in Figure 2.1. EIS data was collected between the frequency of 100 kHz and 0.1 Hz at a direct current (DC) bias potential of 0.425 V vs. RHE, which is within the double layer region. Data was analyzed through use of ZView software (Scribner Associates, Inc.). As seen in Figure 2.3, through plotting the real impedance (Z') versus the imaginary impedance (Z'') a Nyquist plot is produced. This allows for extraction of the Warburg impedance (Z_W) to be translated into total resistance of the electrochemical system (R_Σ , where $R_\Sigma = R_{\text{ionic}} + R_{\text{electronic}}$) using Equation 2.2.^{53,54}

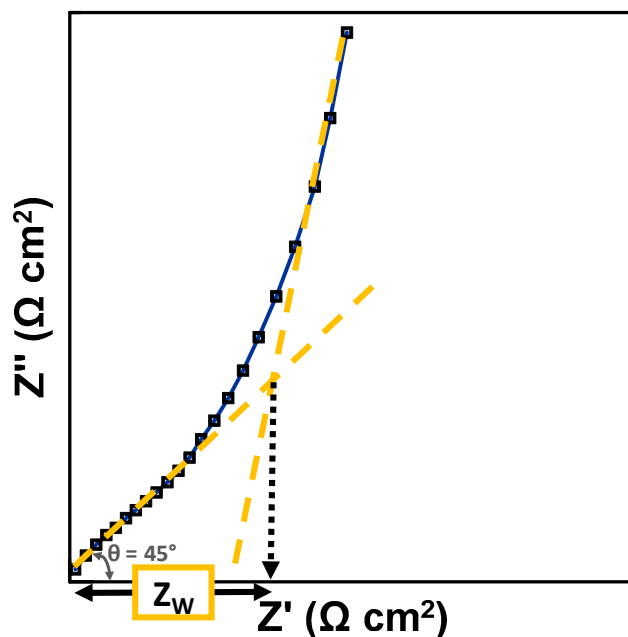


Figure 2.3. Typical EIS measurement for fuel cell catalysts.

$$R_\Sigma = 3 \times Z_W \quad [2.2]^{55}$$

2.5.1.3 Accelerated Stress Testing (AST) with Oxygen Reduction Reaction

(ORR) Activity

Oxygen reduction reaction (ORR) activity was measured in O₂-saturated 0.5 M H₂SO₄ using the Pine Instruments potentiostat by running linear sweep voltammetry (LSV). The LSV was ran at a rotation rate of 900 rpm from 0 V to 1.2 V at a sweep rate of 5 mV/s. Before each measurement, the electrolyte was purged with O₂ (g) for 10 minutes.

Accelerated stress testing (AST) was performed on the catalysts using the Solartron potentiostat, where the system ran the catalyst through 5000 CVs at 200 mV/s with 3 CV at 100 mV/s initially and after every 1000 cycles. EIS measurements were also taken initially and after every 1000 cycles at a DC bias potential of 0.425 V. ORR activity was measured before and after AST under the same conditions as above. Capacitive current for each run was subtracted to correct the initial current density to zero.

2.5.2 Hydrogen Fuel Cell Testing for SS-CCE Catalysts

The prepared GDE was punched into 5 cm² pieces to be used as the anode and the cathode in the membrane electrode assembly (MEA). The MEA was made by first drying a piece of cleaned Nafion[®] 212 membrane (Ion Power) in the oven at 90 °C. The MEA was then assembled in a Fuel Cell Technologies, Inc. (FCT) single fuel cell with the use of Teflon gaskets. The cell was closed and tightened to a torque of 45 inch-pounds (5.08 N·m) before being connected to the FCT testing station, seen in Figure 2.4. The components of the FCT station include stainless steel humidification bottles with temperature that is computer controlled to adjust relative humidity of inlet gases. There is a DC electronic load

as well as mass flow controllers for either gas, and manual controls for adjustment of back pressure.

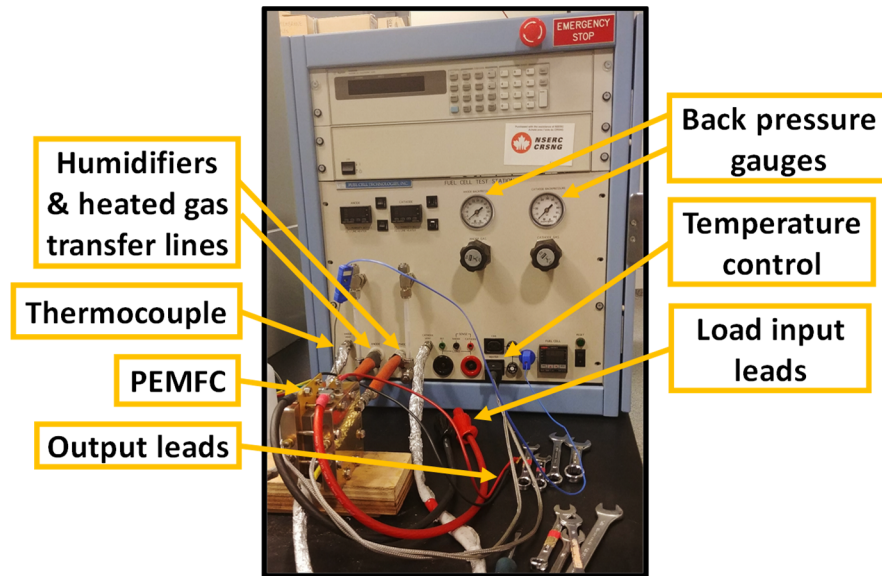


Figure 2.4. The Fuel Cell Technologies, Inc. testing station at Ontario Tech University.

Before performance testing, the MEA had to go through a break-in protocol until electrochemical results were stable and reproducible.⁵⁶ The basis of the break-in protocol included flowing H_2 (g) at the anode and O_2 (g) at the cathode with no back pressure while holding the cell at an operating temperature of $80\text{ }^\circ\text{C}$. Once the cell reached the desired temperature, the potential would be altered between 0.4 V and 0.6 V for a minimum of 3 hours until reproducibility of the polarization curve was observed.

Once the break-in was complete, the cell temperature remained at $80\text{ }^\circ\text{C}$, or $30\text{ }^\circ\text{C}$, and both the anode and cathode temperatures were increased to reach 100% relative humidity (RH). For each electrochemical test the following RH were used at both the anode and the cathode simultaneously: 100%, 80%, 60%, 40% and 20%. Back pressure of 10 psi ($6.9 \times 10^4\text{ N/m}^2$) was implemented at both the anode and the cathode during all tests.

2.5.2.1 Cyclic Voltammetry and Electrochemical Impedance Spectroscopy

The fuel cell was connected to Solartron potentiostat leads to measure CV and EIS of the MEA, with H_2 (g) at the anode and N_2 (g) at the cathode. Tests were performed at varying RH and an operating temperature of 80°C , as well as initial measurements at room temperature. Similar to the three-electrode configuration, the Pt ECSA and R_{Σ} was obtained from data analyses using CView and ZView software by Scribner.

2.5.2.2 Fuel Cell Performance Testing

The fuel cell was connected to the FCT testing station leads to obtain performance polarization curves under conditions of H_2 (g) at the anode and O_2 (g), or air, at the cathode. The typical polarization curve (Figure 2.5) describes the reactions that occur during the life of a fuel cell run. The power density of the curve can also be determined through manipulation of the current density and cell voltage for any given point.

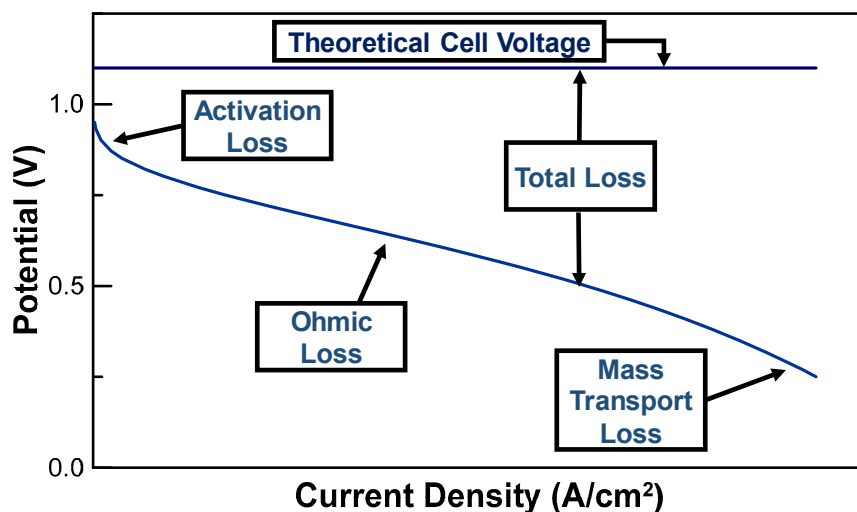


Figure 2.5. Typical fuel cell operation polarization curve comparing to the theoretical performance.

Chapter 3. Investigating the Ionomer in Vulcan-based Catalysts

3.1 Compositional Analyses of Fuel Cell Catalyst Materials

Once the fuel cell catalyst materials were prepared, and before performance testing, the catalysts and preparatory materials were analyzed to determine composition, in particular the desired ionomer loading of ca. 20 wt%. Thermogravimetric analysis (TGA) curves were obtained for the 40% Pt/C (Premetek) SS-CCE and NBE catalysts from oven-dried catalyst mixtures. As seen in Figure 3.1, derivative thermograms (DTG) were created to allow for a clear representation of each mass loss. A control sample of 40% Pt/C (Premetek) catalyst was analyzed which shows a carbon combustion temperature of ca. 340 °C and a Pt loading of 39.65%.

As seen in the DTG curve, the NBE catalyst had an initial mass loss at ca. 320 °C, which is the total decomposition of Nafion[®], in particular the sulfonic acid groups.⁵⁷ The second mass loss, observed at ca. 380 °C, is due to the combustion of the carbon support, which left Pt remaining as the final weight percent of 32.31%. With this information and the total mass of catalyst tested, the amount of Nafion[®] within the catalyst layer was calculated to be 19.23%, which is within the desired range.

The TGA of 40% Pt/C SS-CCE has an initial mass loss beginning at ca. 400 °C and ranging to 600 °C, which is slightly higher than the comparators. This is attributed to the combustion of the carbon within the catalyst layer, where the stabilizing silica network is a factor of the temperature increase. Overall, the remaining mass of this catalyst was 52.40%, which is the fraction of Pt and silica network ($\text{SiO}_2 + \text{SiO}_{1.5}$) within the catalyst. Through use of total catalyst mass and the final weight percent, approximate silica and Pt

loadings were calculated to be 20.65% and 31.75%, respectively, which proves that the final product has an ionomer loading within the desired range.

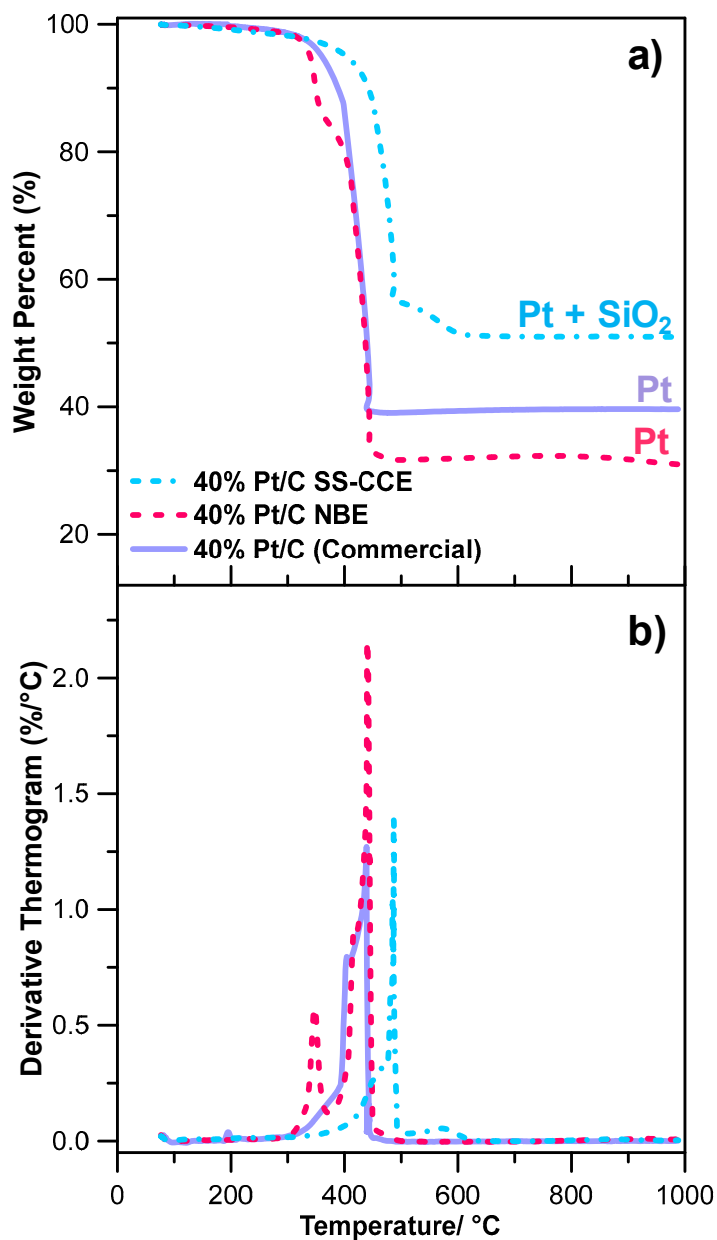


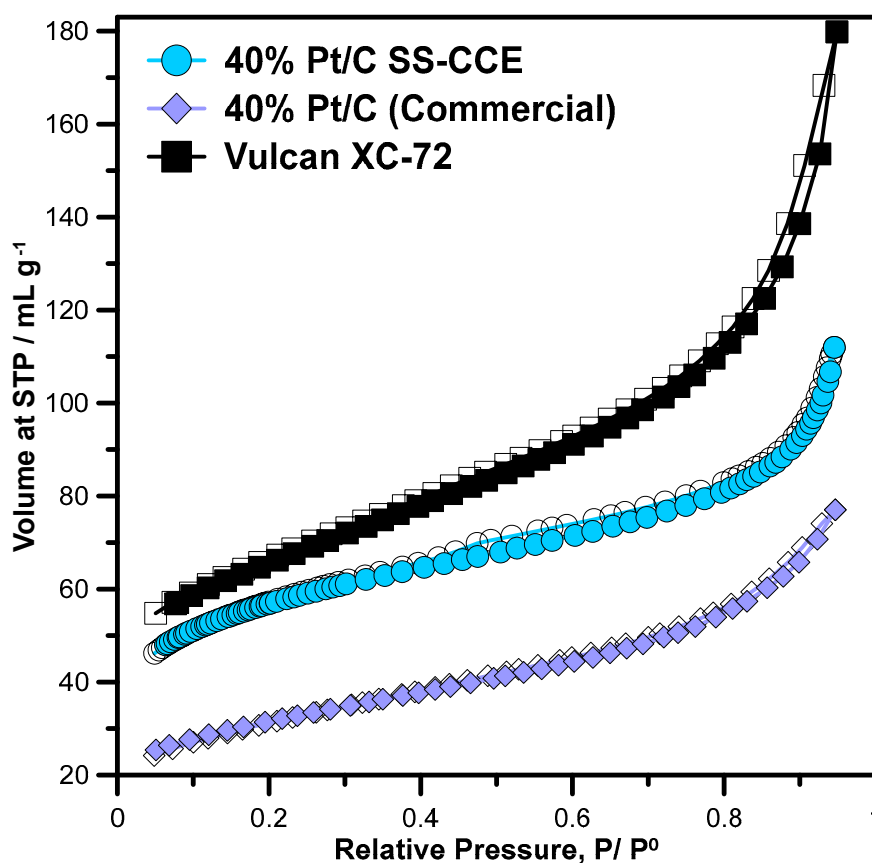
Figure 3.1. 40% Pt/C SS-CCE, commercial 40% Pt/C (Premetek), and NBE material made with 40% Pt/C a) thermograms and b) derivative thermograms to determine Pt catalyst and ionomer loading.

Brunauer-Emmett-Teller (BET) analyses were performed to determine the specific surface area (SSA) of the SS-CCE catalyst materials. The N₂ adsorption-desorption curves are shown in Figure 3.2 and the data is summarized in Table 3.1. Vulcan XC-72 displays the highest SSA at 219 m²/g due to its microporous structure, which is comparable to literature.⁵⁸ With a 40 wt% loading of Pt on the Vulcan XC-72 support, the 40% Pt/C (Premetek) material exhibited a lower SSA of 102 m²/g due in part to the mass of Pt particles that occupy space on the carbon support. The curing process contributed by reducing the amount of pores and ultimately reducing the SSA.⁵⁸ After introducing the silica network to the 40% Pt/C material, SS-CCE was analyzed to have a SSA of 209 m²/g. The difference in SSA between the commercial catalyst and the SS-CCE material is due in part to the silica network that forms a porous structure throughout the catalyst, which in turn would increase SSA of the material. Along with the extracted SSA values, the BET curves exhibit no hysteresis loop along with, according to IUPAC classifications, a type II isotherm. This is typical for materials having primarily micropores and very minimal or non-existent mesopores.⁵⁹

Table 3.1. Summary of physical properties of the studied fuel cell catalyst materials.

Material	Ionomer	SSA	Average Pt	Catalyst Layer
	Loading (%)	(m ² /g)	Crystallite Size (nm)	Thickness (μm)
Vulcan XC-72	N/A	219	N/A	N/A
40% Pt/C (Comm.)	N/A	102	2.86 ± 0.11	N/A
40% Pt/C NBE	19.23	N/A	3.97 ± 0.28	8.35 ± 0.88
40% Pt/C SS-CCE	20.65	209	4.42 ± 0.52	4.39 ± 0.88
20% Pt/C SS-CCE ^a	32%	227	2 – 3	12.66 ± 2.20

^a Ionomer loading, BET SSA and average Pt crystallite size for 20% Pt/C SS-CCE obtained from R. Acheampong dissertation.⁶⁰

**Figure 3.2.** Brunauer-Emmett-Teller analyses of three fuel cell catalyst materials 40% Pt/C SS-CCE, commercial 40% Pt/C (Premetek), and commercial Vulcan XC-72 showing both adsorption (filled symbols) and desorption (open symbols) curves for measuring specific surface area.

Although the SS-CCE and NBE materials use the same 40% Pt/C (Premetek) catalyst, the synthetic processes of both have potential to alter Pt crystallite size. Figure 3.3 displays XRD patterns of the catalyst materials, all of which have the characteristic peaks for the five facets of face-centered cubic (FCC) Pt particles and the {002} facet in carbon.⁶¹ The Pt {220} and {111} peaks were analyzed using the Scherrer equation to calculate the average Pt crystallite size, listed in Table 3.1. The Pt crystallite size for each material ranges from 2.86 nm to 4.42 nm, where the slight differences can be attributed to the processes required to prepare the catalyst materials.

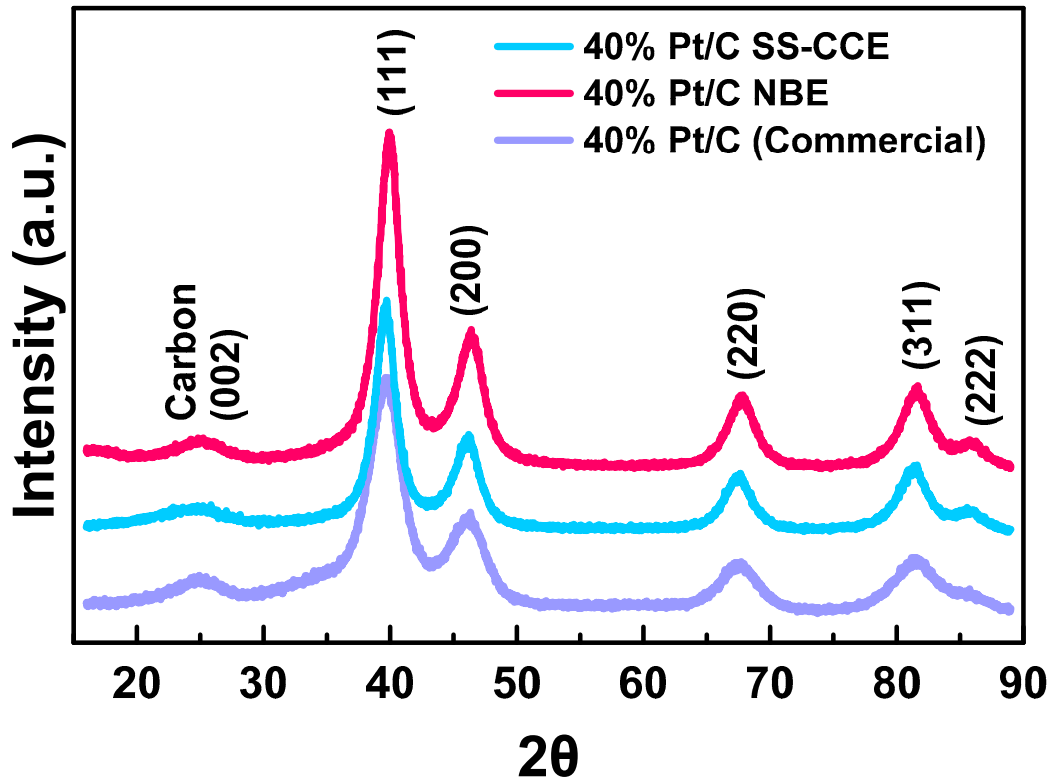


Figure 3.3. Overlaid X-ray diffraction patterns of three fuel cell catalyst materials commercial 40% Pt/C (Premetek), 40% Pt/C NBE material, and 40% Pt/C SS-CCE, including Miller Indices of Pt and C facets.

The cured electrodes were studied under scanning electron microscopy (SEM) combined with energy dispersive X-ray (EDX) spectroscopy analyses. The cross-sections of the electrodes were imaged to view the layers including the CL, MPL, and GDL, depicted in Figure 3.4. The EDX-mapping images (Figure 3.5) allow for a more accurate determination of the catalyst layer thickness due to the visibility of the highly concentrated area of Pt in the CL. The thickness of the catalyst layer for three comparable electrodes is displayed in Table 3.1: 40% Pt/C SS-CCE, 20% Pt/C SS-CCE, and 40% Pt/C NBE. The 40% Pt/C SS-CCE has the thinnest catalyst layer at 4.39 μm , with the next being the 40% Pt/C NBE at 8.35 μm , each having relatively uniform surfaces as seen in the measurement deviations. Both catalyst layers obtaining 40% Pt/C were thinner than the 20% Pt/C SS-CCE (12.66 μm) due to the decreased amount of ionomer and catalyst used in the preparatory steps. The 20% Pt/C SS-CCE appears to have sharp fractures along the cross-section of Figure 3.6 c), which is due to increased silica content creating a brittle CL.

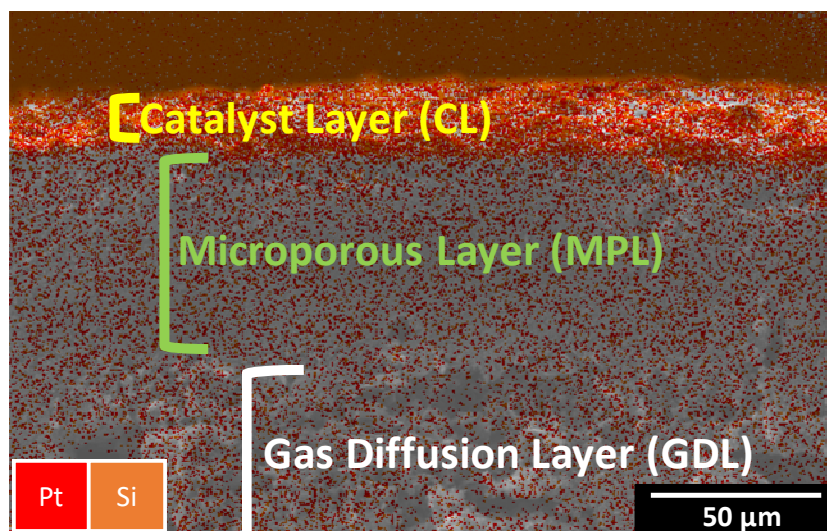


Figure 3.4. Definitive EDX sample image of a SS-CCE fuel cell electrode for determination of catalyst layer thickness.

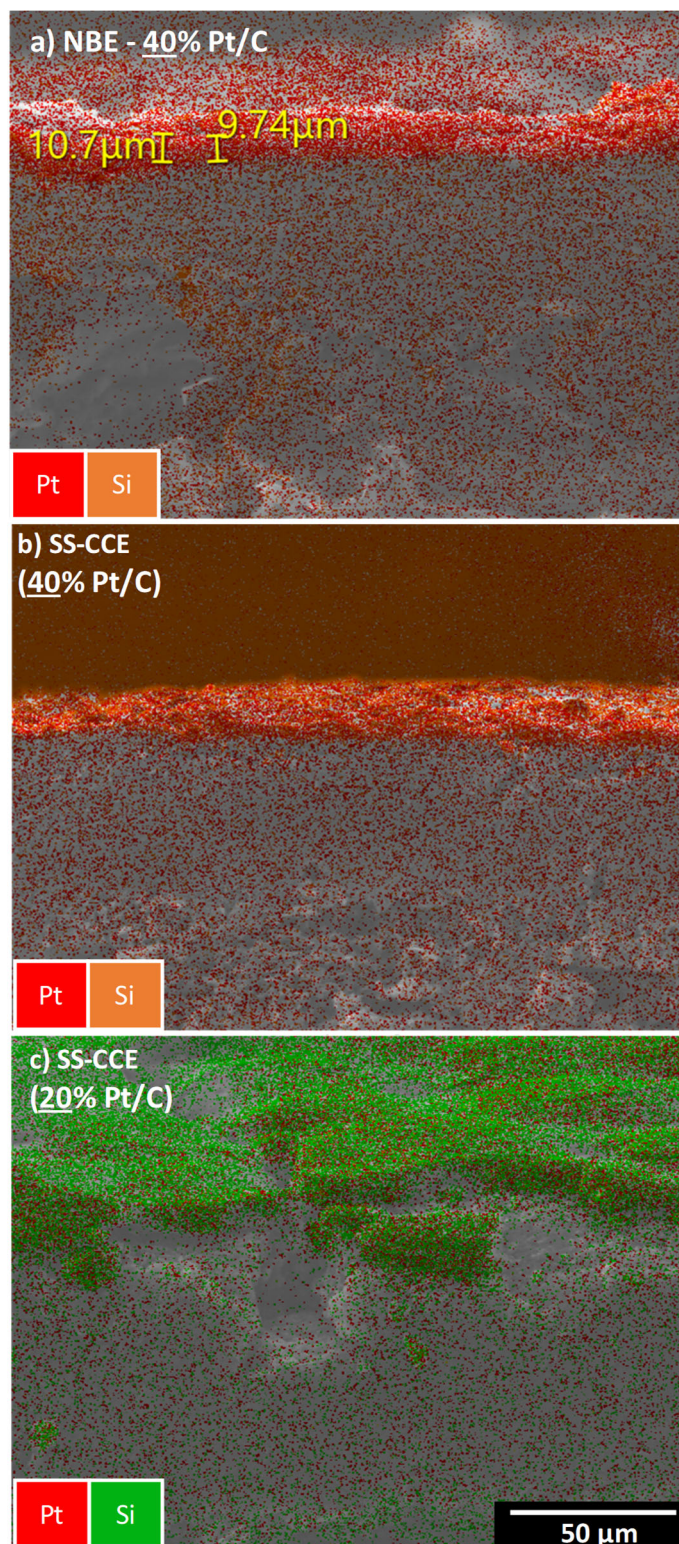


Figure 3.5. Energy dispersive X-ray spectroscopy mapping of three fuel cell electrodes a) 40% Pt/C Nafion[®]-bound electrode, b) 40% Pt/C SS-CCE, and c) 20% Pt/C SS-CCE.

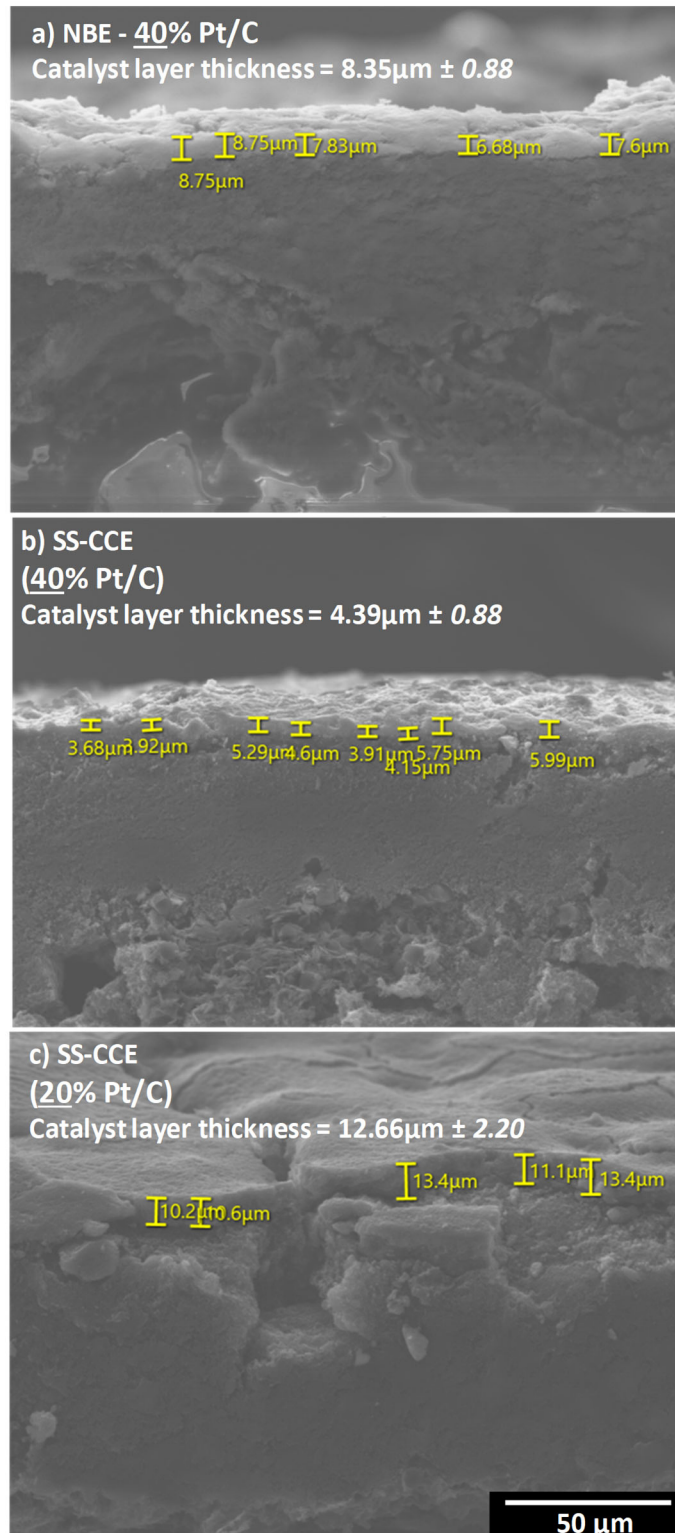


Figure 3.6. Scanning electron microscopy images of three fuel cell electrodes a) 40% Pt/C Nafion[®]-bound electrode, b) 40% Pt/C SS-CCE, and c) 20% Pt/C SS-CCE.

3.2 Comparison of SS-CCEs Fabricated from 20% Pt/C versus 40% Pt/C

In order to investigate if a thinner catalyst layer will enhance fuel cell performance, electrochemical properties of materials with differing C-to-Pt ratio have been compared. When reducing the amount of carbon black support within the catalyst material, a relative reduction in ionomer loading occurs. The catalyst material of interest is composed of 60% carbon whereas standard materials are comprised of 80% carbon. A comparison is shown in Figure 3.7 displaying fuel cell performance of each material.

The polarization and power density output curves for each MEA display that 40% Pt/C SS-CCE has a maximum power density of ca. 475 mW/cm², whereas 20% Pt/C SS-CCE only reaches 400 mW/cm². This means that less carbon black within the catalyst layer produces higher power output in the H₂/O₂ fuel cell configuration. The activation, ohmic, and mass transport regions on the polarization curves show that the 40% Pt/C SS-CCE is the superior catalyst by maintaining voltage as each region is crossed. Overall, this comparison provides evidence that, with less carbon in the catalyst layer, the fuel cell performance is enhanced.

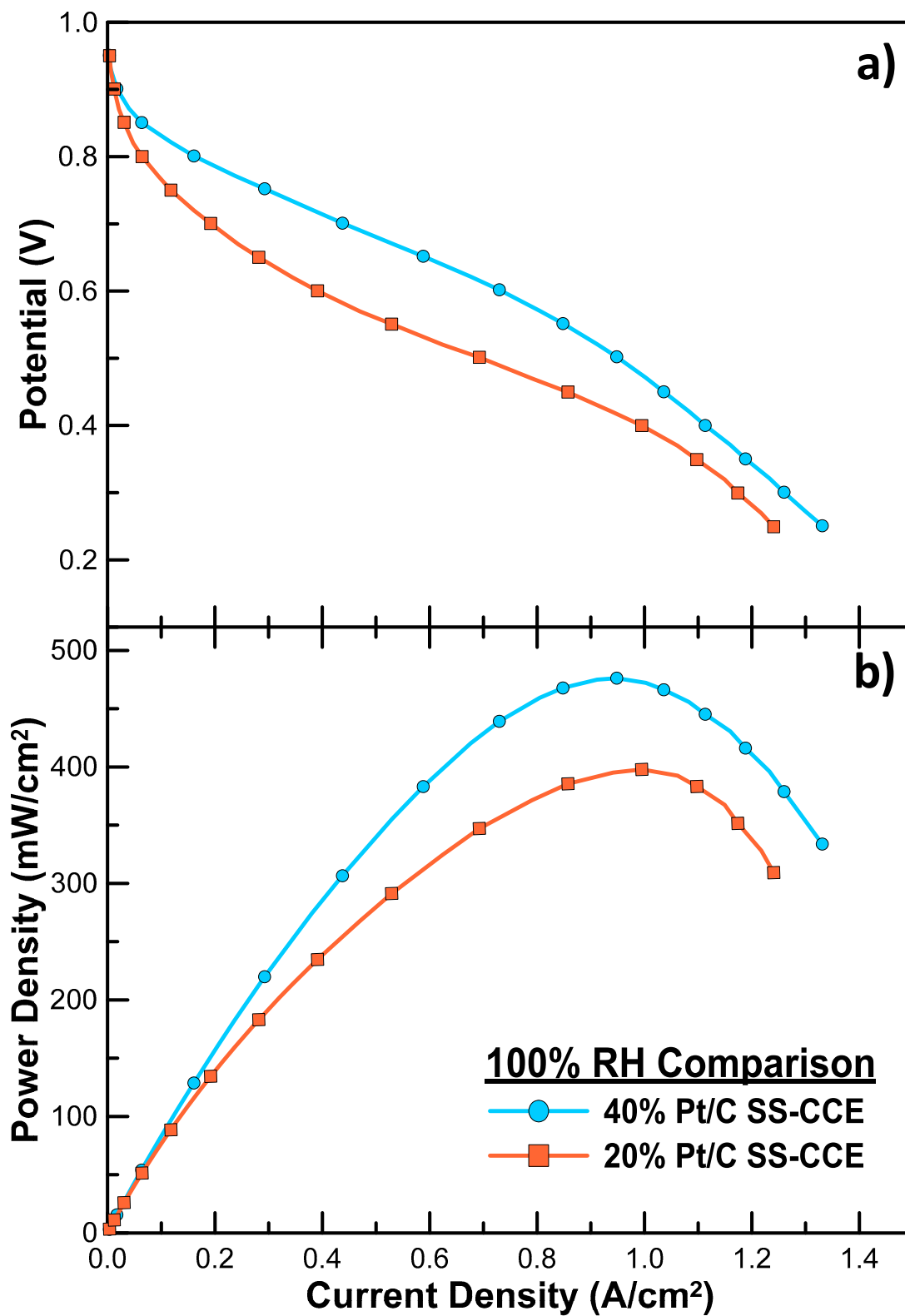


Figure 3.7. H₂/O₂ fuel cell polarization curves comparing current density against a) cell potential and b) power density, operating at 80°C for the symmetric MEA comprised of 40% Pt/C SS-CCE versus 20% Pt/C SS-CCE, both with loadings of 0.2 mg_{Pt}/cm².

Electrochemical diagnostic tests were performed, in the H₂/N₂ configuration, on both 40% and 20% Pt/C SS-CCE materials starting with cyclic voltammetry (CV). Data was interpreted and summarized into Table 3.2. 40% Pt/C SS-CCE had an electrochemically active surface area (ECSA) of 40.81 m²/g whereas the 20% catalyst has an ECSA of 34.62 m²/g. The pattern in the data is that as temperature increases, and relative humidity decreases, the ECSA decreases due to poor membrane hydration and proton conductivity.⁶²

Table 3.2. ECSA values from integrated hydrogen desorption region of CV's for 40% Pt/C SS-CCE and 20% Pt/C SS-CCE, at operating cell temperatures of 30°C and 80°C.

Cell Temperature (°C)	SS-CCE Pt Content (%)	ECSA (m ² /g)
30	40	40.81
	20	34.62
80	40	18.37
	20	25.76

Electrochemical impedance spectroscopy (EIS) was performed, where both Nyquist and capacitance plots are shown in Figure 3.8. Data was analyzed and R_Σ, at both cell temperatures, was calculated. With knowledge that electron transport is rapid, the resistance in the system, due to electron transport, is negligible and so from here on in it can be assumed that R_Σ = R_{ionic}.⁶³ Analyses provided values of R_Σ and limiting capacitance for each electrode material which was summarized in Figure 3.9.

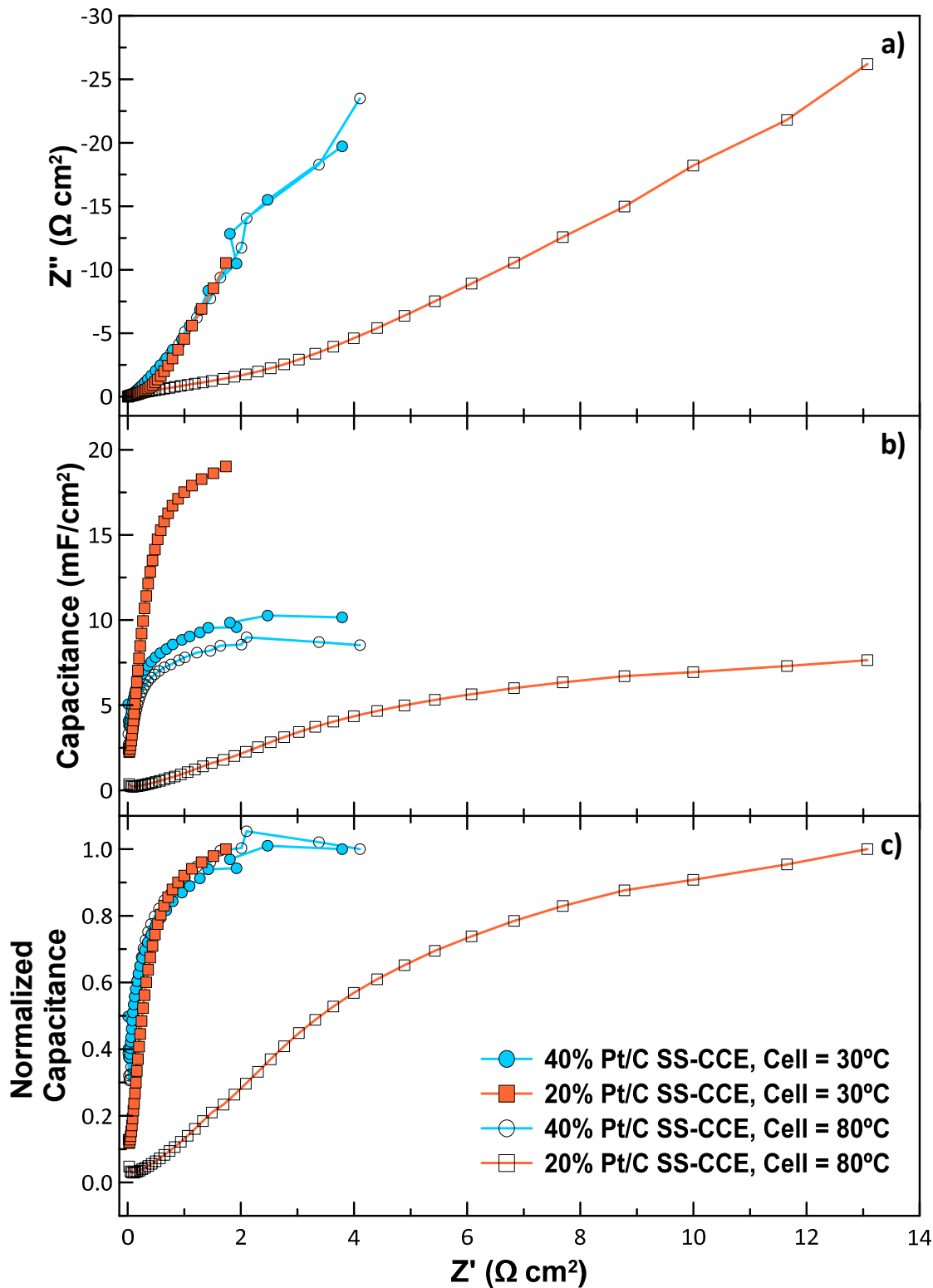


Figure 3.8. EIS data interpreted to display a) Nyquist, b) capacitance and c) normalized capacitance plots for symmetric MEA comprised of 40% Pt/C SS-CCE versus 20% Pt/C SS-CCE, at operating cell temperatures of 30°C and 80°C and a DC bias of 0.425 V.

It is evident that when performing under less humid conditions, 40% Pt/C SS-CCE has greater ability to maintain performance levels. Whereas, 20% Pt/C SS-CCE material shows an increase in resistance when tested at lower RH and higher temperature, 80°C. This is due to the phenomenon that a thicker catalyst layer with 20% Pt/C cannot stay as well hydrated as a thinner one, leading to higher resistance within the material. A similar trend was observed for the limiting capacitance data, where the 20% Pt/C material reached much higher capacitances than 40% Pt/C SS-CCE, at low cell temperature/ high RH. The lower capacitance in 40% Pt/C SS-CCE can be attributed to the reduction in ionomer, as well as the material containing less carbon, both of which are highly capacitive materials. Overall, 40% Pt/C SS-CCE displays higher stability at the two operating temperatures and increased performance. This conclusion supports the hypothesis that using a catalyst with a higher Pt loading/ lower C content allows for thinner catalyst layers and enhances performance capabilities.

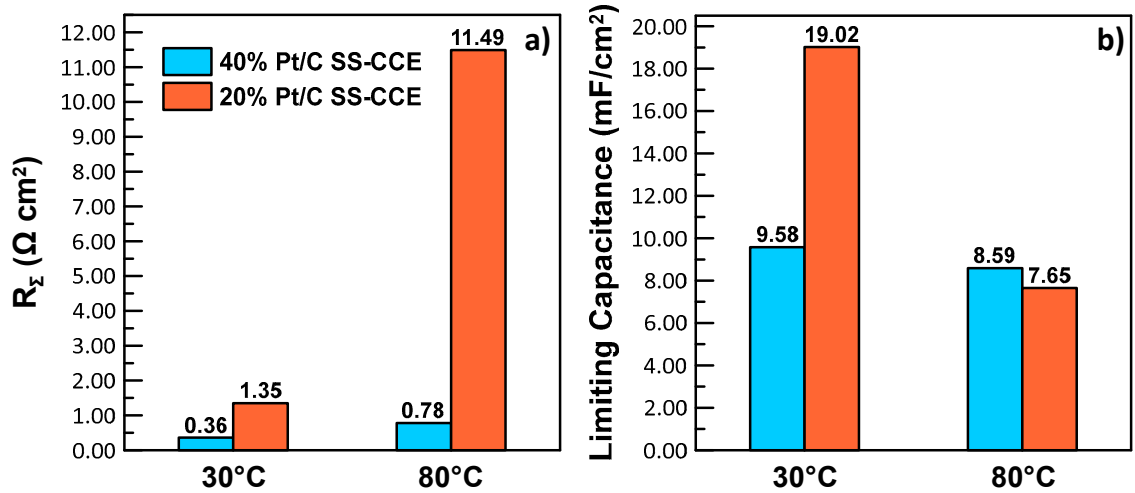


Figure 3.9. Comparison of EIS-derived data showing a) total resistance and b) limiting capacitance for the symmetric MEA comprised of 40% Pt/C SS-CCE versus 20% Pt/C SS-CCE at cell operating temperatures of 30 °C and 80 °C.

3.3 Electrochemical Comparison of Ionomers in 40% Pt/C Catalyst Layers

3.3.1 Studying Temperature Dependence on Different Ionomers

As previously shown, a thinner catalyst layer increases fuel cell performance of the SS-CCE. To gain a better understanding of the 40% Pt/C SS-CCE material it will be compared to a standard Nafion[®] containing electrode, 40% Pt/C NBE. Both materials of interest were analyzed through CV and EIS at room temperature (ca. 30 °C) to observe performance at low temperature and high RH. The cyclic voltammograms for both materials are displayed in Figure 3.10 and were analyzed to find the ECSA of SS-CCE and NBE to be 40.81 m²/g and 43.93 m²/g, respectively, as seen in Table 3.3.

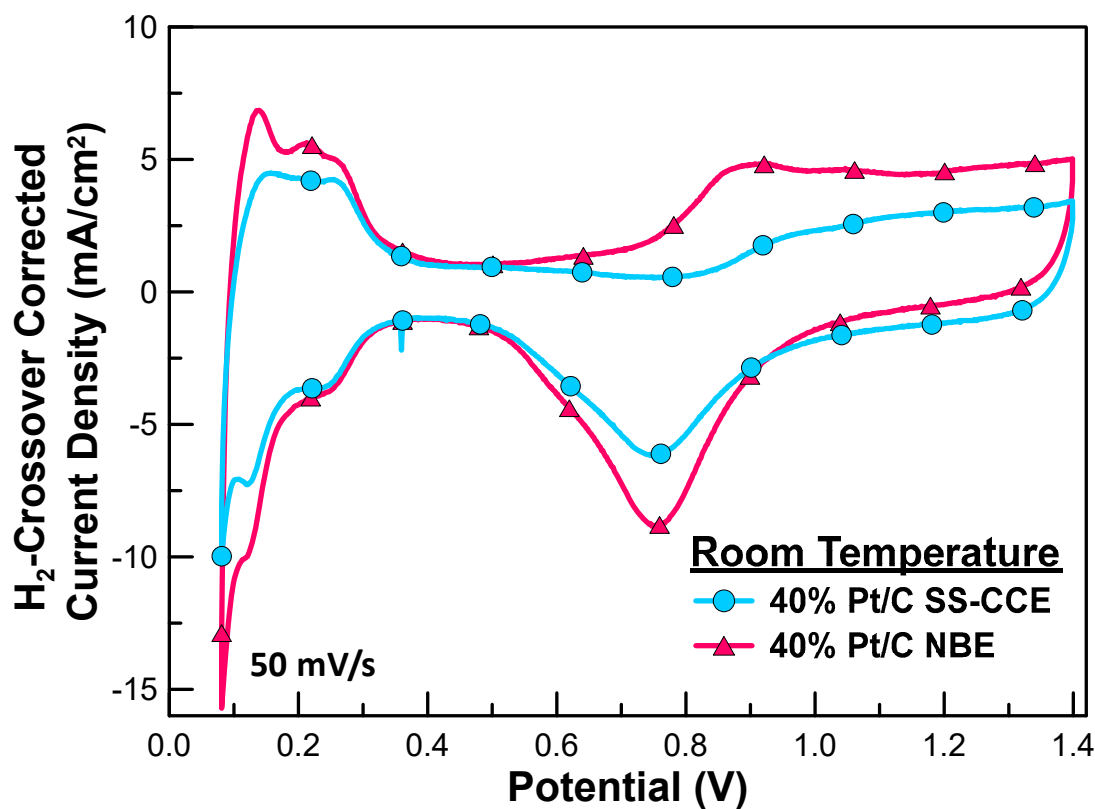


Figure 3.10. Cyclic voltammetry of symmetric MEAs with 40% Pt/C SS-CCE and NBE tested at room temperature under conditions of H₂(g) at the anode and N₂(g) at the cathode.

EIS data at room temperature is shown in Figure 3.11 which displays that NBE and SS-CCE materials obtain similar capacitance and resistance. This is due to both ionomer materials obtaining similar functionalities, such as the sulfonate groups. Normalized capacitance plots displayed in Figure 3.11 c) provide a visual representation of the different Warburg regions for each material which proves that each MEA obtains slightly different diffusion reaction relations due to the different microstructure of the materials, in particular the ionomer.

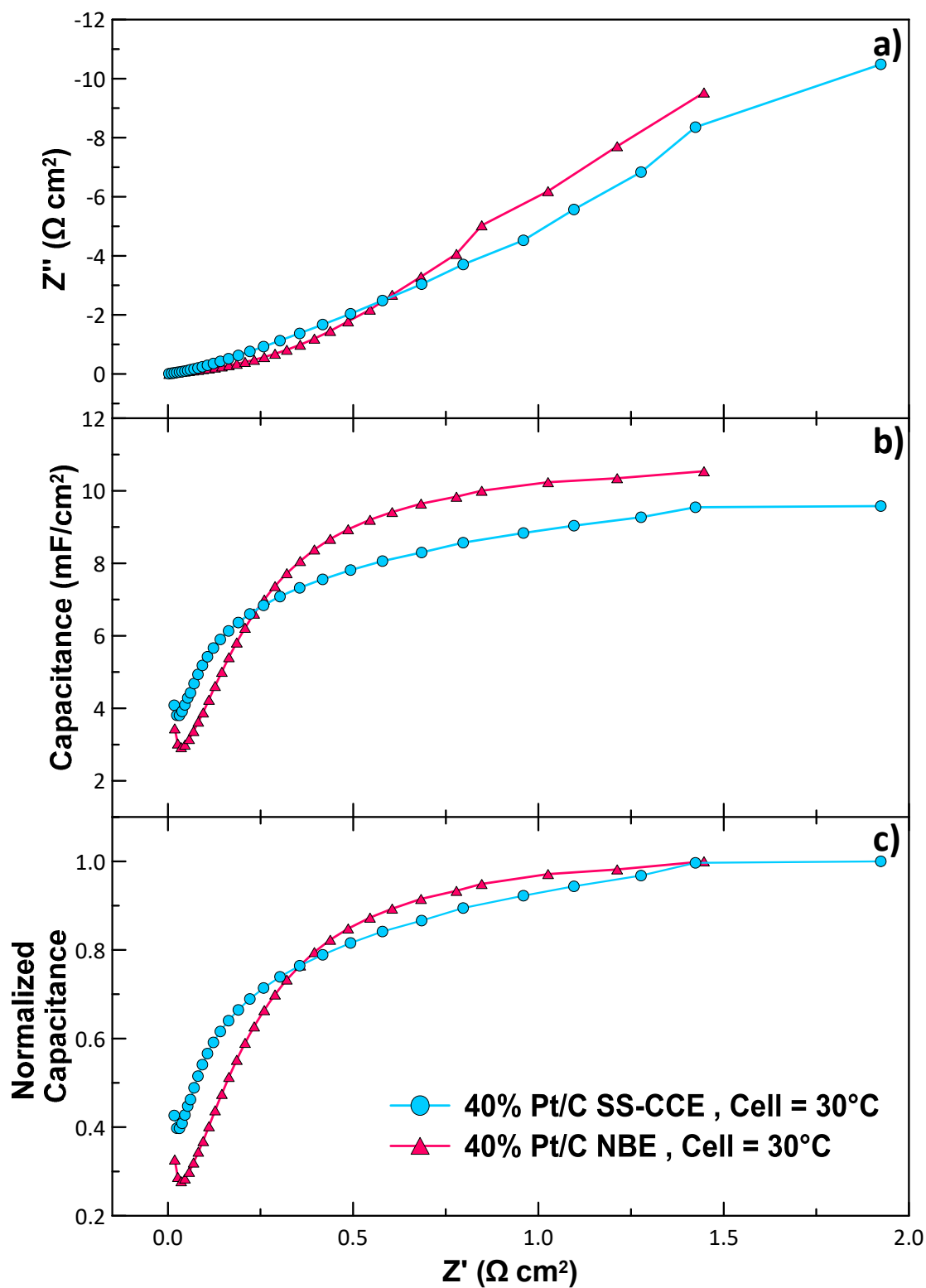


Figure 3.11. EIS of symmetric MEAs with 40% Pt/C SS-CCE and NBE tested at room temperature under conditions of $N_2(g)$ at the cathode and $H_2(g)$ at the anode at a DC bias of 0.425 V.

Cyclic voltammograms of each MEA, at 30 °C and 80 °C, are displayed in Figure 3.12. In general, at 30 °C the ECSA is larger than when tested at 80 °C. A contributing factor to this would be flooding that occurs at 80 °C cell temperature. This would inhibit mass and electronic transport within the MEA.⁶² Table 3.3 displays the ECSA's of each MEA at both cell temperatures. The difference in ECSA of 55.0% for SS-CCE and 37.8% for NBE from 30 to 80 °C can be attributed to the increased water content. SS-CCE is more hydrophilic, which explains the loss in ECSA due to flooding occurring, and causing degradation of the Pt catalyst.

Table 3.3. Electrochemically active surface area calculated from CV data for the symmetric MEA comprised of 40% Pt/C SS-CCE versus 40% Pt/C NBE at operating temperatures of 30°C and 80°C.

Cell Temperature (°C)	Catalyst	ECSA (m ² /g)
30	SS-CCE	40.81
	NBE	43.93
80	SS-CCE	18.37
	NBE	27.27

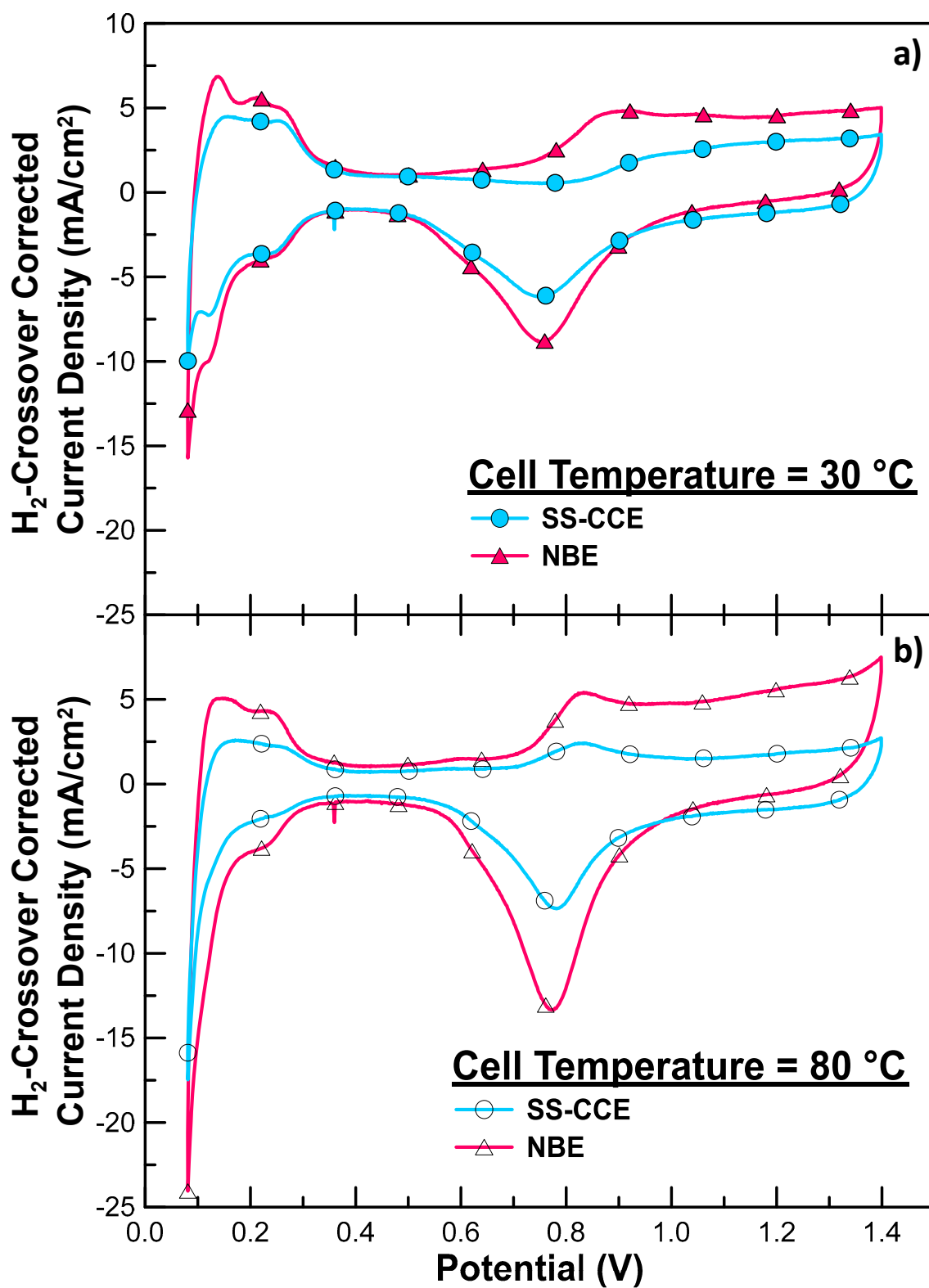


Figure 3.12. Cyclic voltammetry of symmetric MEAs with 40% Pt/C SS-CCE and NBE tested at room temperature and 80 °C under conditions of N₂(g) at the cathode and H₂(g) at the anode at a sweep rate of 50 mV/s.

Figure 3.13 shows that there are fewer differences in the EIS response of the SS-CCE when measured at 30 and 80 °C, which indicates its hydration state has not changed significantly. As seen in the Nyquist plot Figure 3.13 a), the SS-CCE data nearly overlaps at high and low operating temperatures. The similarity in SS-CCE at both temperatures is also seen in the Warburg region, being most visible in the normalized capacitance plot Figure 3.13 c), whereas the NBE material shows clear differences in this region. The shorter Warburg length at higher temperature indicates that the NBE has improved catalyst layer proton conductivity at elevated temperatures.⁵⁴ From the high and low cell temperature comparison, the SS-CCE catalyst layer shows far less variability and is more reliable when expected to perform at varying temperatures.

Both R_{Σ} and limiting capacitance were extracted from the EIS data and displayed in Figure 3.14. The resistance of the SS-CCE MEA remains much more stable than that of the NBE material when comparing the data at high and low temperatures. At 80 °C, the NBE material obtains the lowest resistance of the comparators. NBE displays slightly larger capacitive abilities than SS-CCE at 0.425 V at both operating temperatures. Since both electrodes contain similar amounts of capacitive materials, carbon support and ionomer, it is understandable that the capacitive abilities are near to each other. At both cell temperatures, water content remains to be a barrier for the SS-CCE catalyst layer.

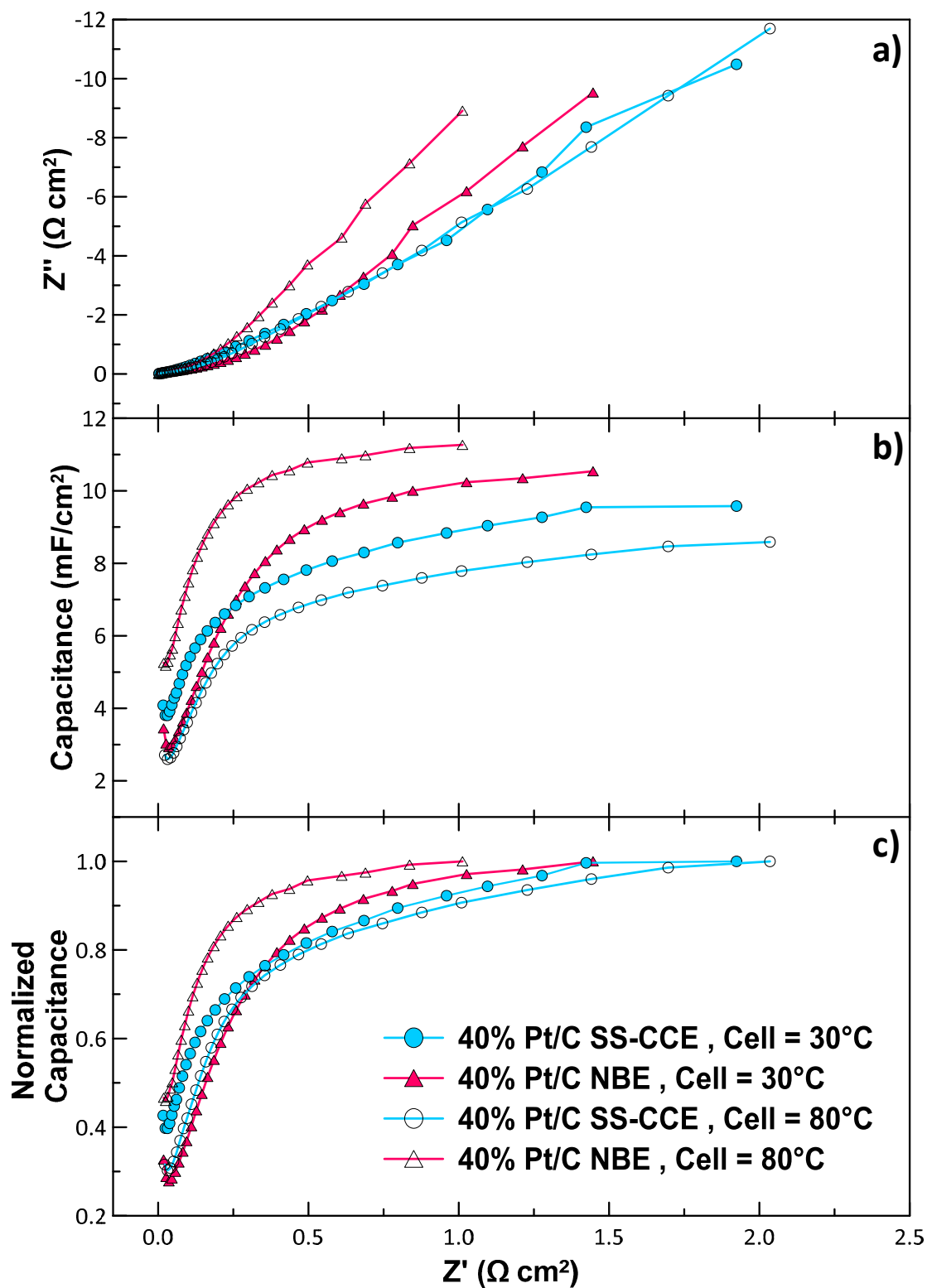


Figure 3.13. EIS of symmetric MEAs with 40% Pt/C SS-CCE and NBE tested at room temperature and 80°C under conditions of $N_2(g)$ at the cathode and $H_2(g)$ at the anode at a DC bias of 0.425 V.

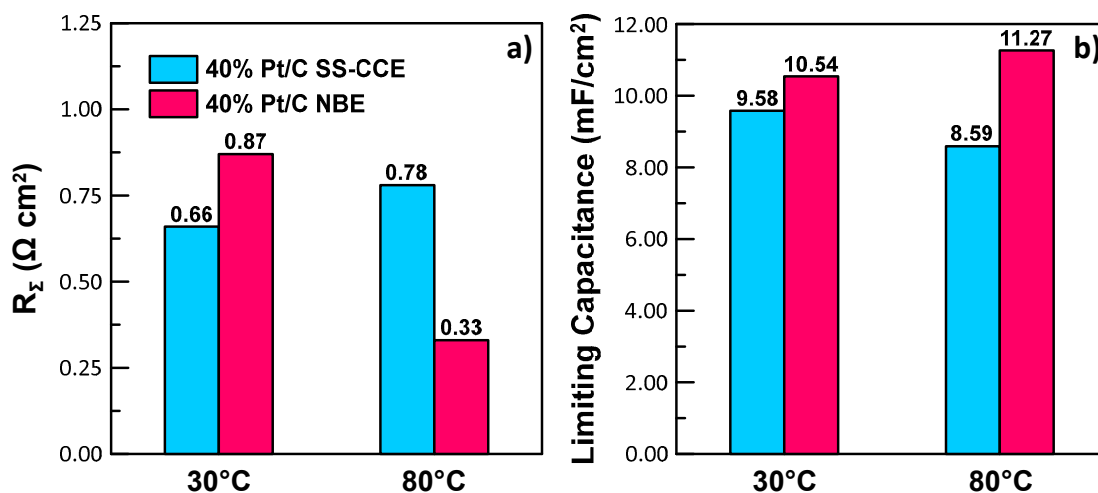


Figure 3.14. Comparison of EIS-derived data showing a) total resistance and b) limiting capacitance for the symmetric MEA comprised of 40% Pt/C SS-CCE versus NBE at cell operating temperatures of 30 °C and 80 °C.

As predicted, both materials perform similarly in the fuel cell at low operating temperature. Although NBE has a larger ECSA and lower resistance at 80 °C, the SS-CCE is more stable when cell temperature is altered. Due to the Pt/C catalyst being surrounded with an integrated sulfonated – silica network, there is greater durability than NBE. Nafion® is not able to form a network, like that of SS-CCE, being that the ionomer is commercially prepared prior to mixing with the Pt/C catalyst.

3.3.2 Studying Relative Humidity Dependence on Electrochemical Characteristics

In the full cell, symmetric configuration, both materials were tested through CV to determine the ECSA. Figures 3.15 a) and b) display cyclic voltammograms at varying relative humidity (RH) of the input gases, for SS-CCE and NBE materials. Although there was not a vast range in variation, both materials at low RH display a plateau in ECSA values. This pattern can be seen in Figure 3.15 c) which compares ECSA versus RH for

both SS-CCE and NBE materials. The ECSA decreases as the RH decreases due to low proton conductivity. Also visible in the comparison is that the NBE generally maintains higher ECSA than the SS-CCE system at all RH. Since the Pt loadings were verified to be nearly equivalent through TGA, the difference in ECSA can be attributed to SS-CCE having poorer proton conductivity than the NBE.

In Figure 3.13, the EIS data for NBE at varying RH showed data at 20% RH to be incomprehensible, since it exceeded the limits for the rest of the data. A similar occurrence was seen for SS-CCE at both 20% and 40% RH, where EIS data was outside reasonable limits, leading to the inability to accurately calculate R_{Σ} .

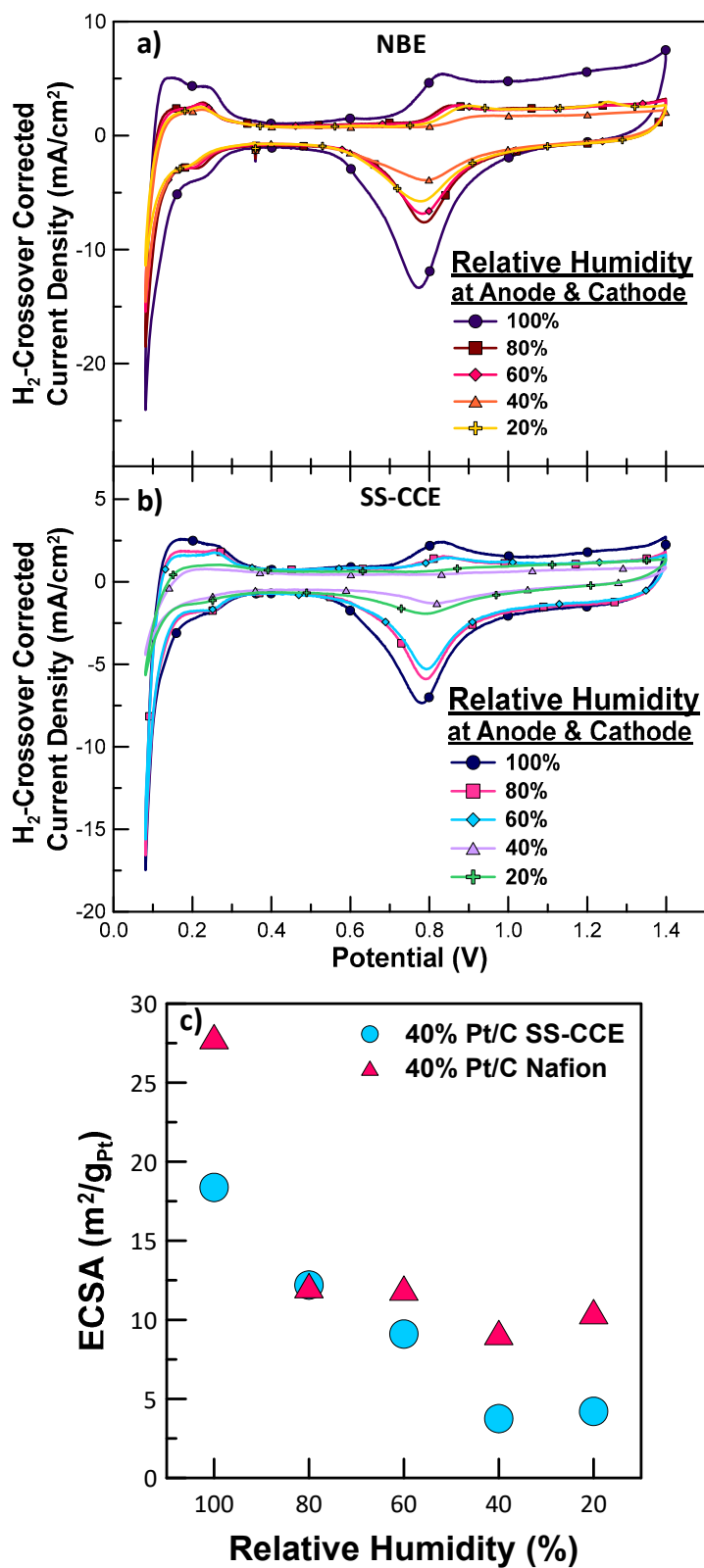


Figure 3.15. Cyclic voltammograms at 50mV/s for symmetric MEA tested at 80 °C made with 40% Pt/C a) NBE and b) SS-CCE tested at varying relative humidity with N_2 (g) at the cathode and H_2 (g) at the anode, with c) summarized ECSA data versus RH for each MEA.

EIS data, for NBE materials at RH 40% to 100% and for SS-CCE at RH 60% to 100%, is displayed in Figures 3.16 and 3.17, respectively. The NBE material reacts similarly at 80% and 100% RH which is apparent when looking at the Warburg region, but reactions differentiate at RH 60% and 80%, as visible in the Nyquist plots. The capacitance decreases as the RH decreases, due in part to the decreased water content. This is similar to the lower capacitance seen at lower temperature in the previous temperature dependence study. The NBE material conducts ions and fuel gasses with fewer barriers than SS-CCE at a cell temperature of 80 °C.⁶⁴

In comparing the SS-CCE data, the Warburg region appears similar to the NBE material, but does not show much variation when the RH increases from 60% to 100%. This coincides with previous data showing that the silica network is less sensitive to variation in the testing conditions, i.e. RH.

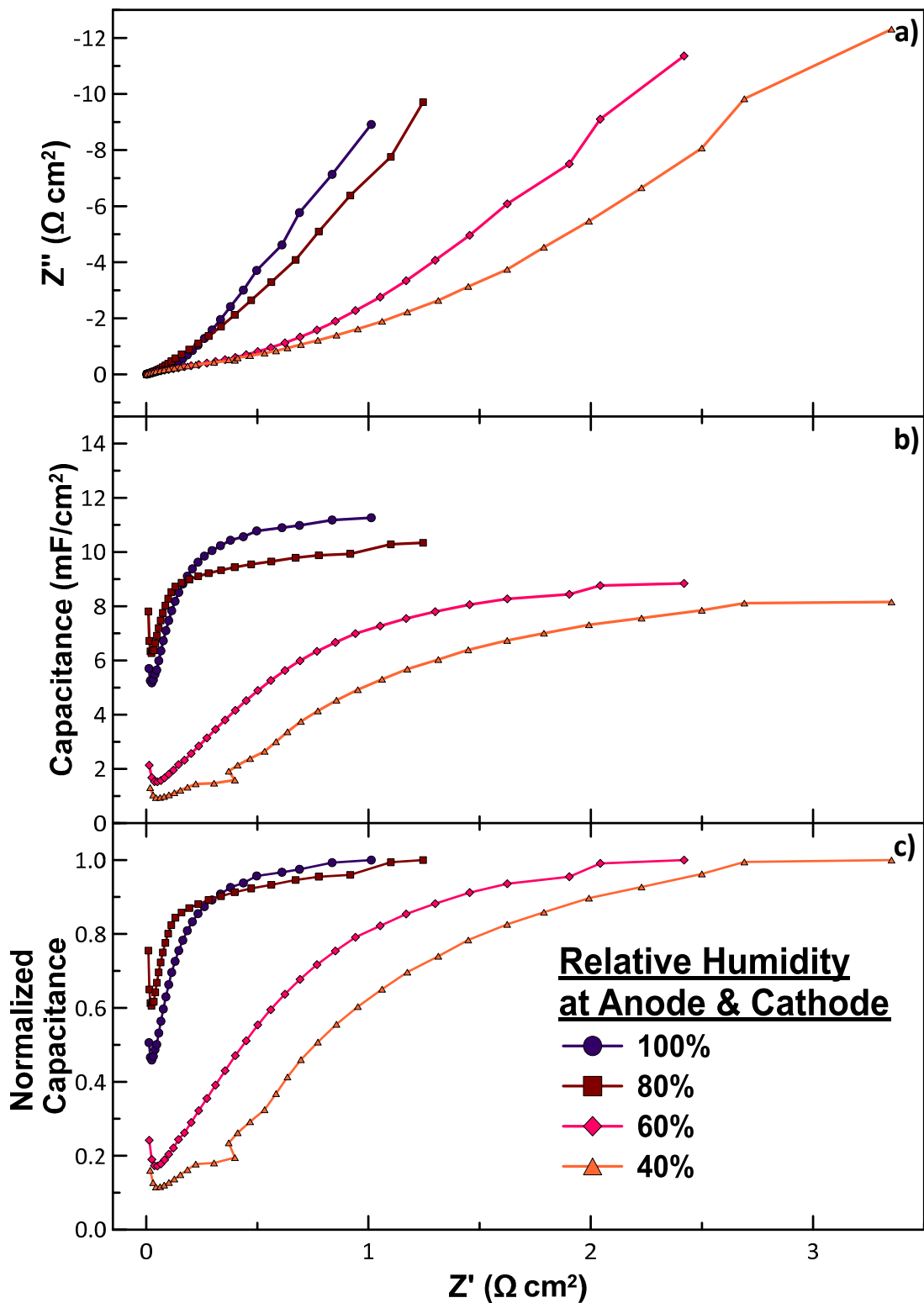


Figure 3.16. EIS comparison for NBE tested at varying relative humidity in $N_2(g)$ / $H_2(g)$ configuration displaying only high RH a) Nyquist, b) capacitance and c) normalized capacitance plots measured at a DC bias of 0.425 V.

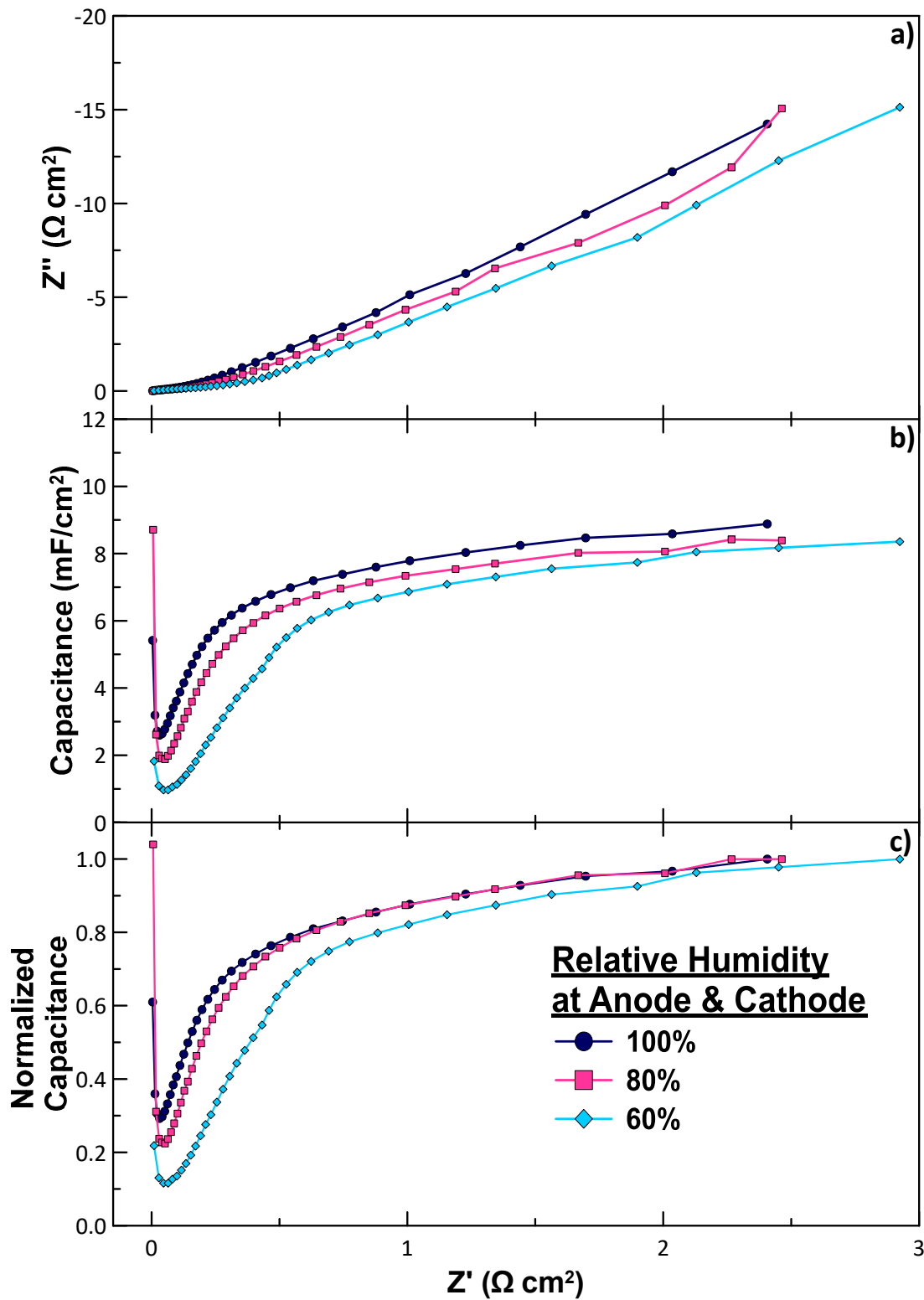


Figure 3.17. EIS comparison for SS-CCE tested at varying relative humidity in $N_2(g)$ / $H_2(g)$ configuration displaying only high RH a) Nyquist, b) capacitance and c) normalized capacitance plots measured at a DC bias of 0.425 V.

The data interpreted from the EIS plots is summarized in Figure 3.20 and compared at each RH, where R_{Σ} could not be accurately determined at low RH. Within the NBE, R_{Σ} decreases as RH increases, whereas R_{Σ} for the SS-CCE appears to remain stable at varying RH. This further proves that the SS-CCE material can provide more reliable performance when altering the RH of the inlet gas, at a cell temperature of 80 °C. The limiting capacitance values display that SS-CCE has similar but low capacitance compared to the NBE at all RH. Through this comparison, it is clear that NBE shows a steady incline of capacitance at 0.425 V as RH increases. It is also observable that the SS-CCE displays stability in capacitance capabilities at higher RH values. Therefore, SS-CCE is able to provide steady results at varying RH meaning it obtains materials of greater stability with similar performance capabilities as NBE.

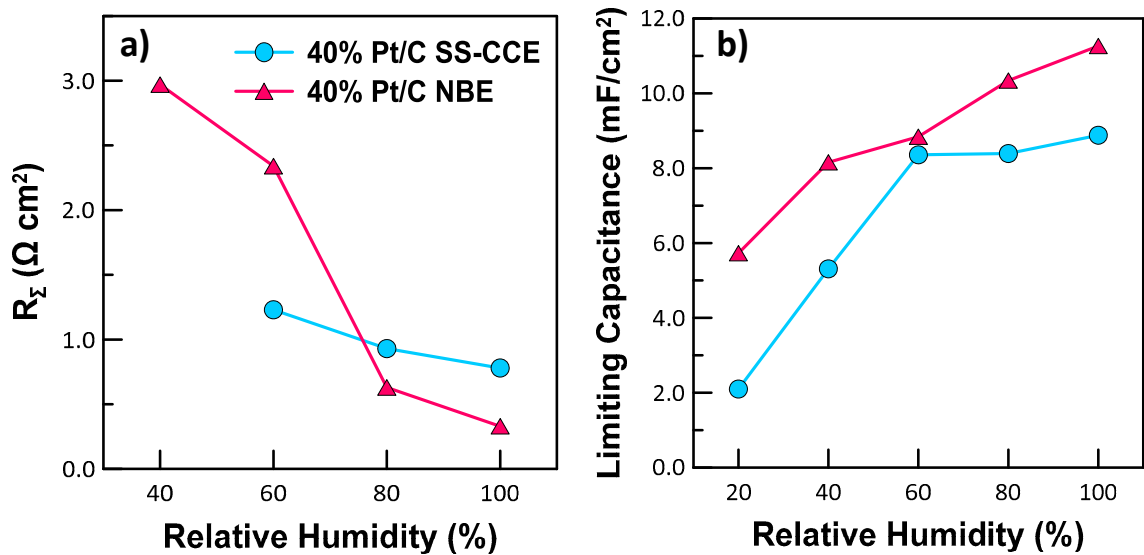


Figure 3.18. Comparison of EIS - derived data at a DC bias of 0.425 V and a cell temperature of 80 °C displaying the a) total resistance and b) limiting capacitance of symmetric MEAs with 40% Pt/C SS-CCE and NBE.

3.3.2.1 Studying the Effects of Cathodic Inlet Gas on Fuel Cell Performance

Fuel cell performance was assessed by feeding H_2 (g) at the anode and O_2 (g), or air, at the cathode, while scanning from 1.0 V to 0.2 V and measuring current output. Figures 3.19 and 3.20 display the current density versus cell potential, and power density, polarization curves for the NBE material with O_2 (g), and air at the cathode, respectively. For both cathodic gasses, it is apparent that decreasing RH also decreases the peak power density. This trend shows that, with less humidity, there is less water content to aid in mass and ion transport.

The primary difference in the collected data is that the peak power density decreases ca. 45%, at 100% RH, when flowing air at the cathode, versus O_2 (g). The decrease in output when testing under air is due to the decrease in O_2 (g) that is available to react at the Pt active sites. Although the air flow input is five times greater than that of oxygen, there remains inefficiencies which mimic complications seen when implemented in real-world applications, such as fuel cell electric vehicles.

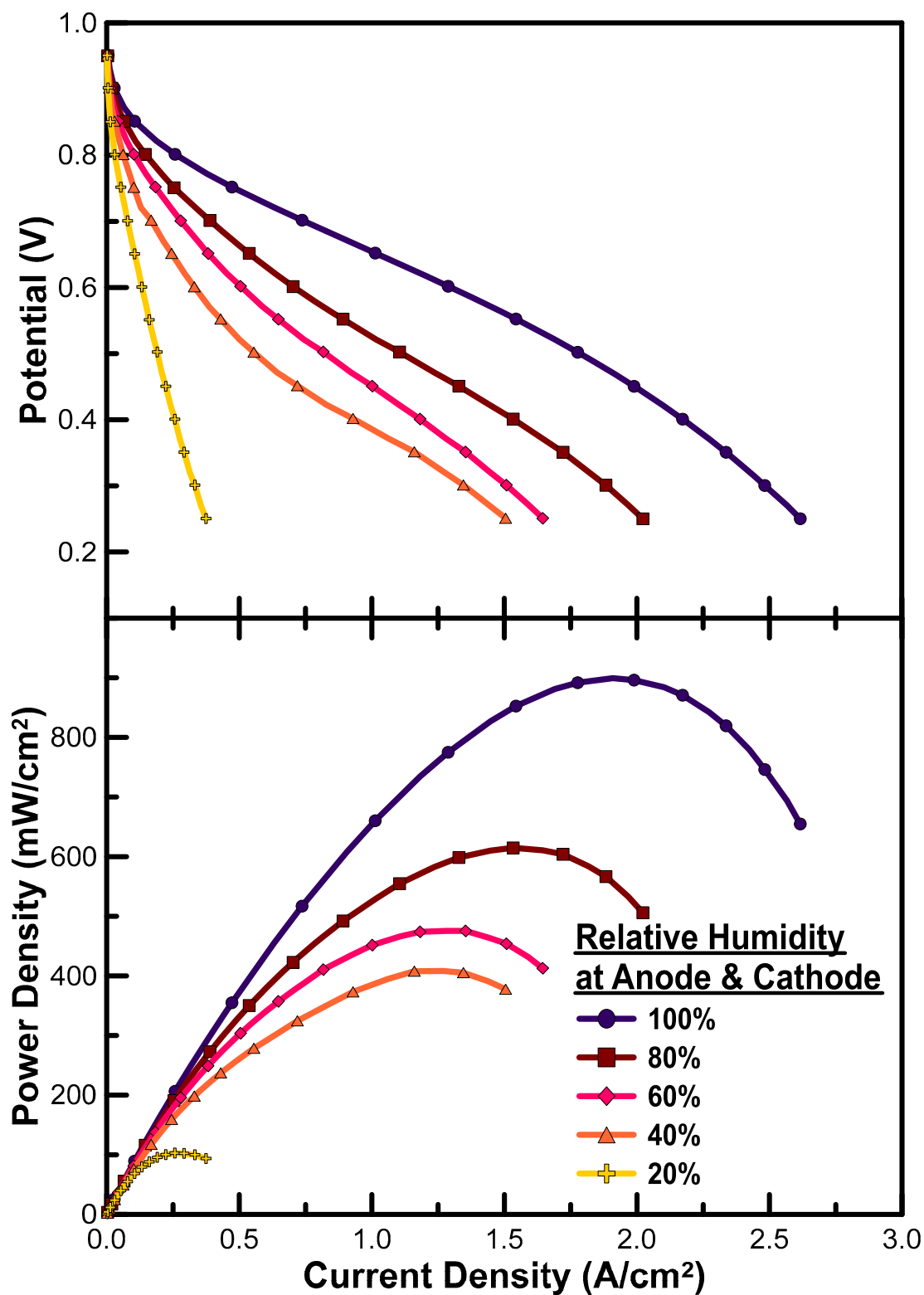


Figure 3.19. Performance curves of current density versus a) cell potential and b) power density for a symmetric MEA with 40% Pt/C NBE tested at varying relative humidity with O_2 (g) at the cathode and H_2 (g) at the anode at a cell temperature of 80 °C.

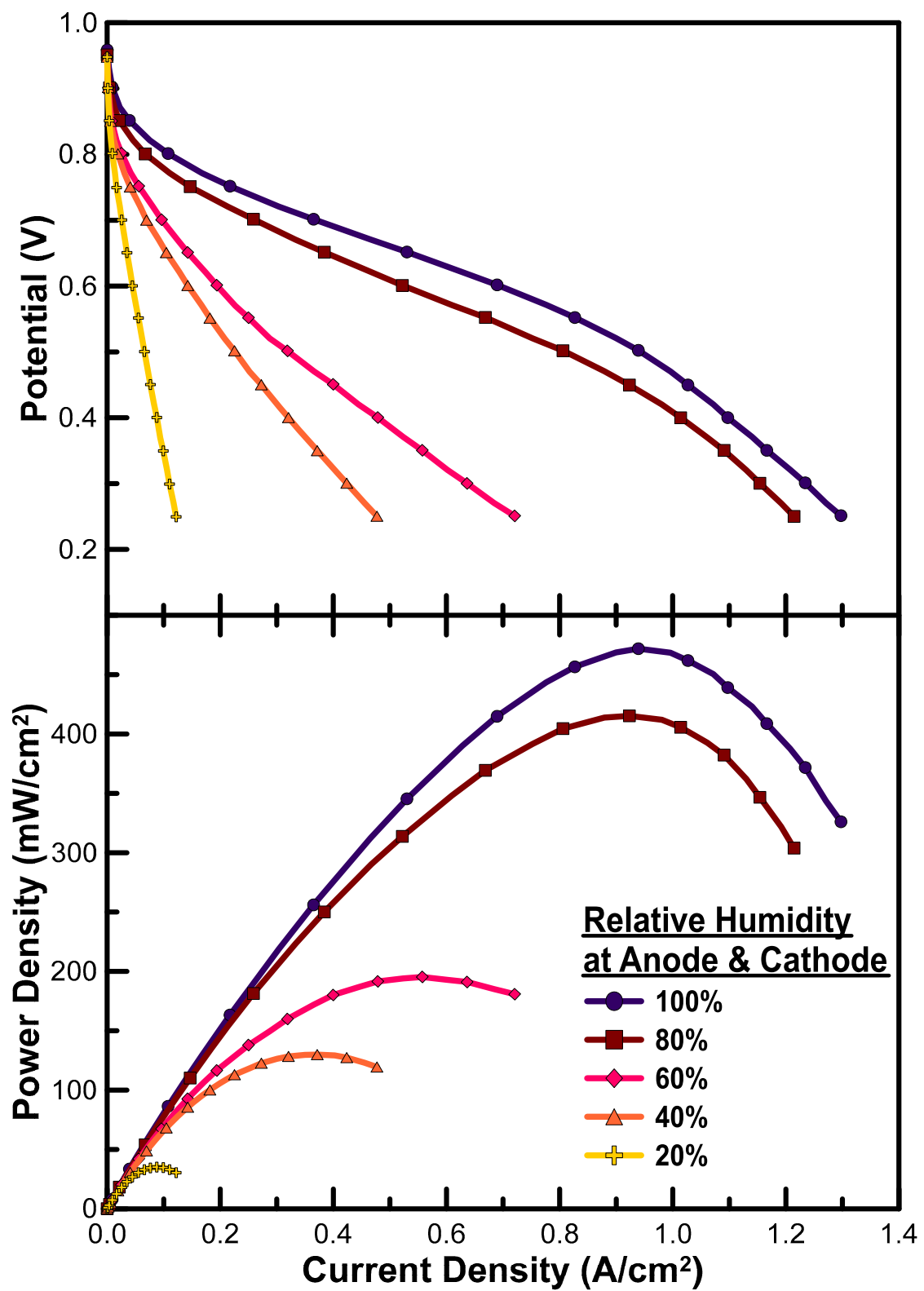


Figure 3.20. Performance curves of current density versus a) cell potential and b) power density for a symmetric MEA with 40% Pt/C NBE tested at varying relative humidity with air at the cathode and H_2 (g) at the anode at a cell temperature of 80 °C.

Identical to the NBE fuel cell testing protocol, the SS-CCE material was tested with O_2 (g) and air at the cathode, as seen in Figures 3.21 and 3.22. The polarization curves for both cathodic gases display that activity is poor at low RH and it remains stable at high RH. This trend is seen in the electrochemical studies in the H_2/N_2 configuration, where at higher RH the material was able to put out comparable performance without much decline in activity. Once tested at lower RH, 40% and 20%, a decrease in activity was present due to reduced water content.

The decline in peak power density between cathodic gases is slightly lower than that of the NBE with a ca. 38% decrease when changing the cathode gas from O_2 (g) to air. This decline in activity can be explained by the lower O_2 (g) percentage present for the ORR to occur, at the cathode.

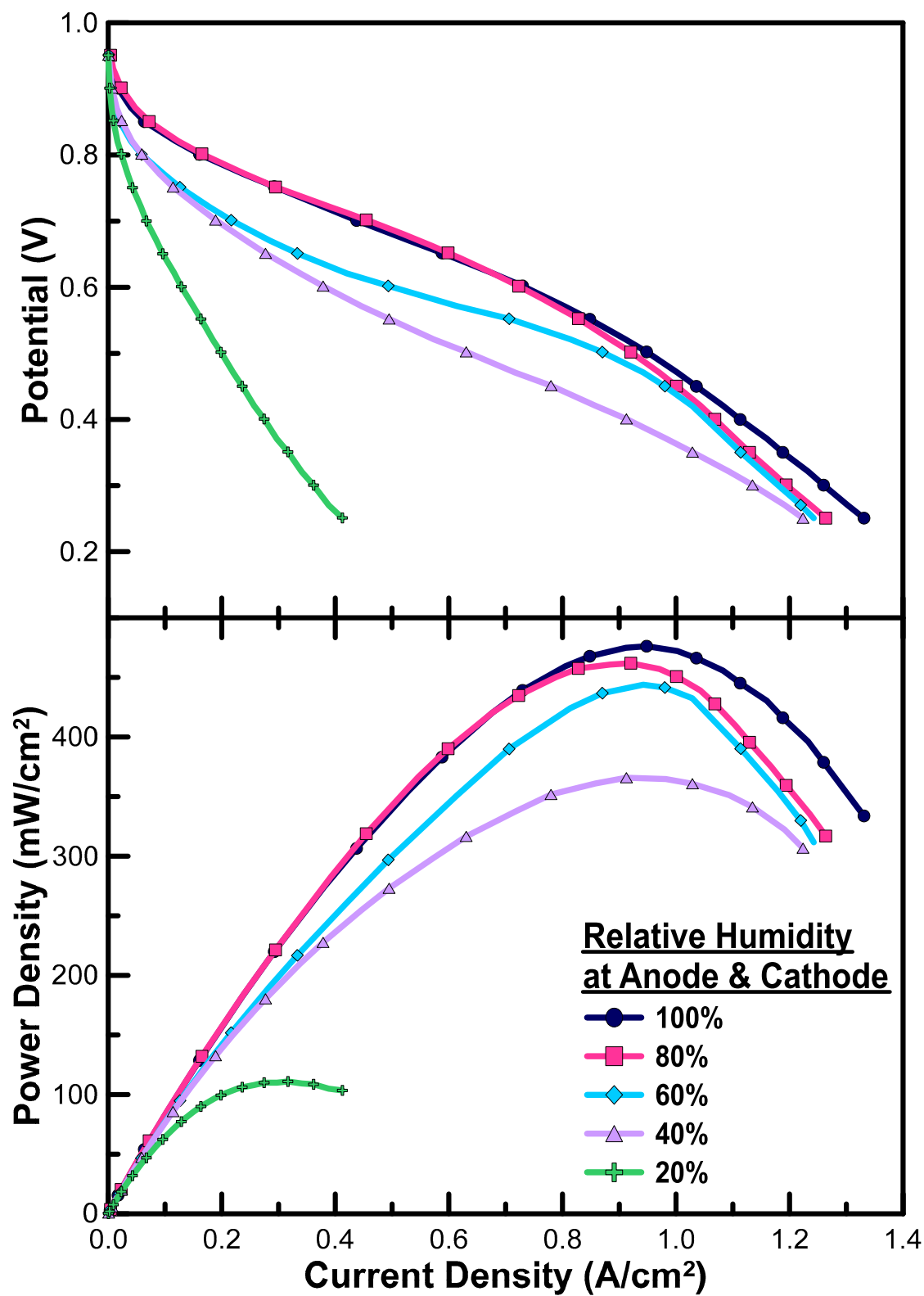


Figure 3.21. Polarization curve comparison of current densities for a symmetric MEA with 40% Pt/C SS-CCE tested at varying relative humidity with O₂ (g) at the cathode and H₂ (g) at the anode at a cell temperature of 80 °C.

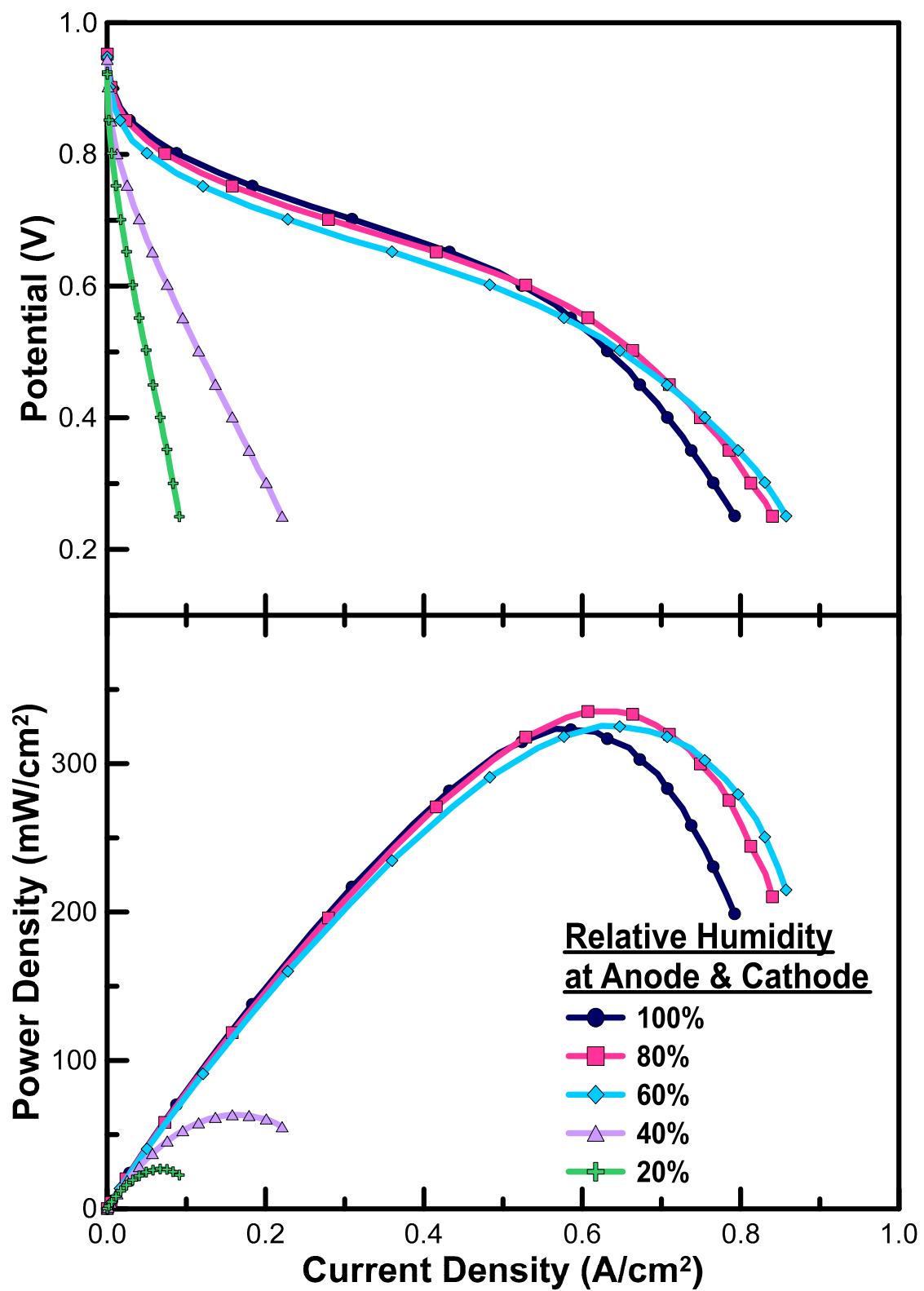


Figure 3.22. Polarization curve comparison of current densities for a symmetric MEA with 40% Pt/C SS-CCE tested at varying relative humidity with air at the cathode and H₂ (g) at the anode at a cell temperature of 80 °C.

The peak power density for each material under both cathode gas conditions are compared in Figure 3.23. The NBE observed a ca. 47% decline from pure O₂ (g) flowing at the cathode to air. For SS-CCE materials, the decline in maximum power density from O₂ (g) to air was ca. 32%. Although NBE materials out-perform SS-CCE, under both cathodic gas conditions, there is a major difference in the performance of the NBE when provided different amounts of O₂ (g). This provides an example of the enhanced versatility of the SS-CCE material, when compared to conventional Nafion[®]-bound materials. SS-CCE is capable of maintaining activity when tested with pure O₂ (g) as well as when reducing the amount of O₂ (g) available to the cathode (i.e. flowing air).

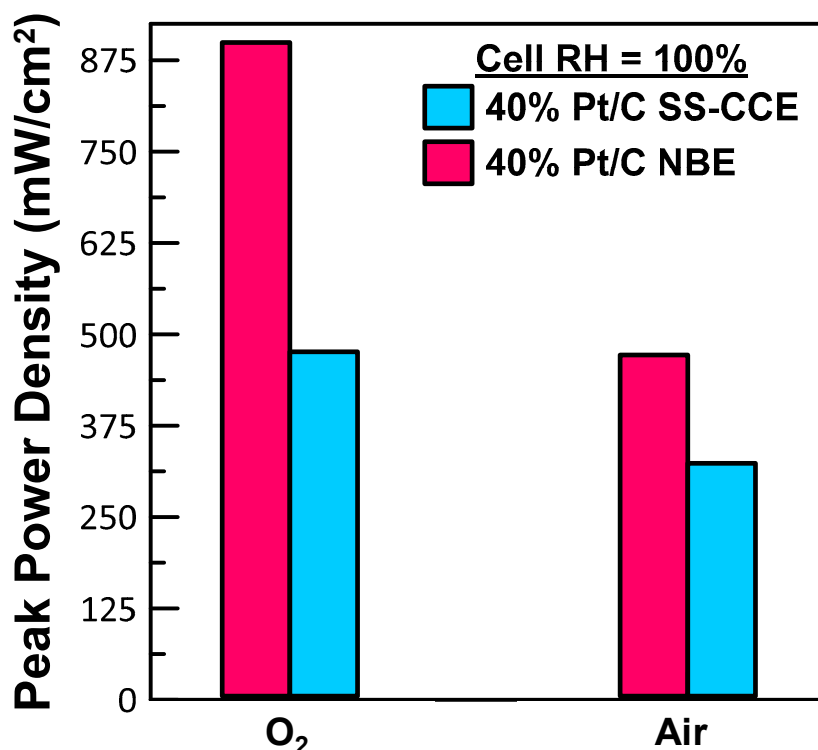


Figure 3.23. Maximum power densities of symmetric MEAs with 40% Pt/C SS-CCE and NBE tested at an operating temperature of 80°C with 100% relative humidity comparing O₂ (g) versus air at the cathode.

Peak power density for both electrode materials, displayed in Figure 3.24, and ECSA normalized peak power density is compared at every RH of interest. When comparing raw power density in both O₂ (g) and air, it is evident that the SS-CCE material obtains a higher tolerance to RH variation. At lower RH there is a decline in activity seen for both electrode materials, where NBE has a steady decline through all RH, at both cathodic gases.

When comparing, ECSA normalized, peak power density, the SS-CCE material acquired similar peak power density as the NBE, at most cell RH. This pattern is seen for both O₂ (g) and air at the cathode. It obtains minimal variation, throughout each RH, in peak power density output, per mass of Pt. These data prove that the SS-CCE material provides comparable activity per ECSA of the material and is on par with activity of conventionally-used NBE materials. Therefore, the SS-CCE is a suitable replacement for Nafion[®] within the catalyst layer, at both the anode and the cathode of a PEMFC.

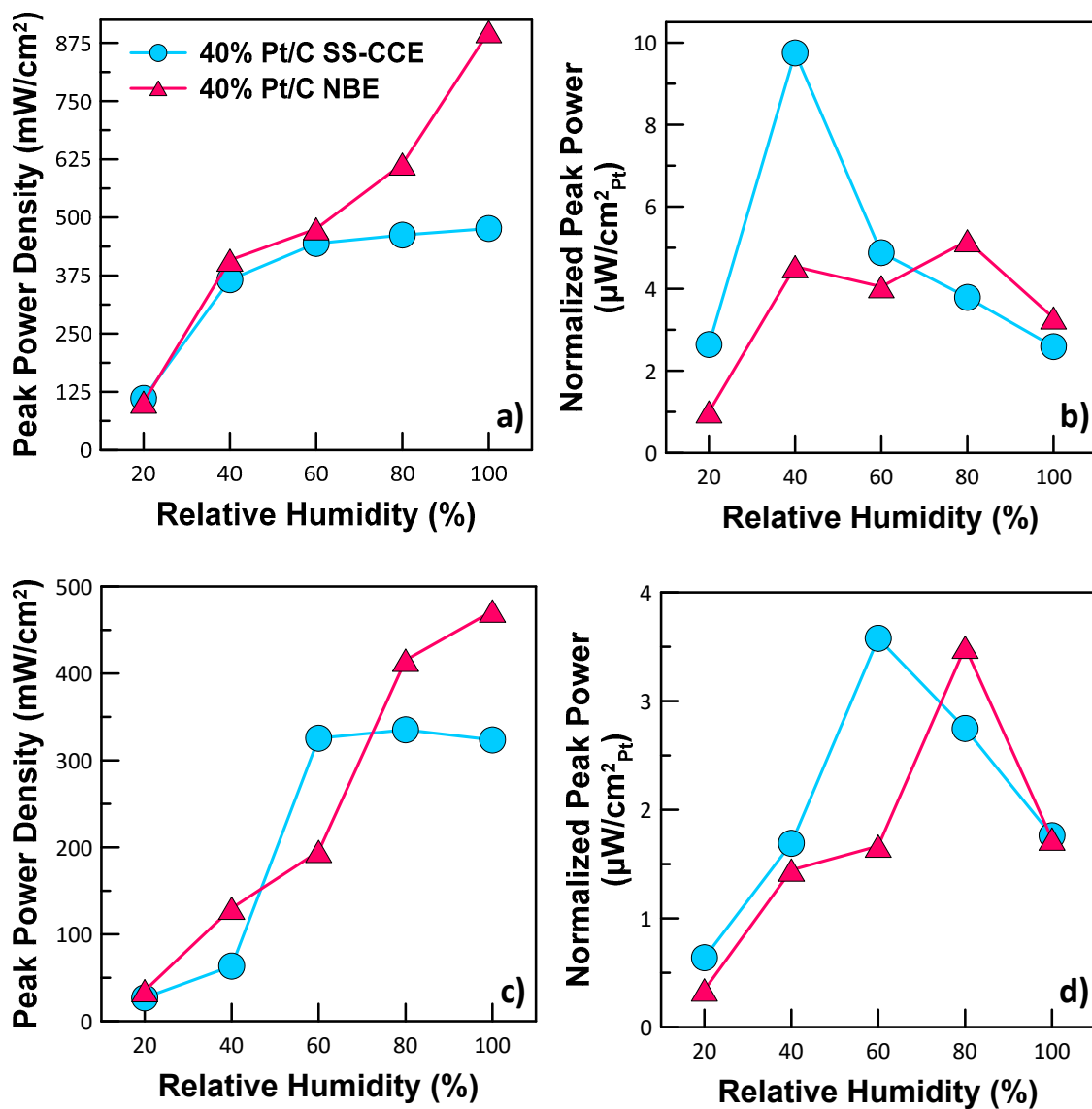


Figure 3.24. Comparison between a) peak power density, and b) normalized peak power density with O₂ (g) at the cathode. Along with c) peak power density, and d) normalized peak power density with air at the cathode. Tested in symmetric configuration using MEAs of 40% Pt/C SS-CCE, and NBE, tested at varying relative humidity with H₂ (g) at the anode.

3.4 Summary

The ionomer loading for 40% Pt/C SS-CCE was determined to be ca. 20 wt%. BET analyses showed that the SS-CCE material had a higher SSA than that of the commercial catalyst, proving that it had a highly open structure which should provide good access to catalyst sites. SEM measurements showed that the CL thickness for 40% Pt/C SS-CCE was considerably thinner than the 20% Pt/C SS-CCE. Because of this, the 40% Pt/C SS-CCE had higher PEMFC performance and showed less variation. The ionomer and carbon network in 40% Pt/C SS-CCE display great stability in EIS data at both cell temperatures. Less resistance is seen in the 40% Pt/C SS-CCE, as well as low capacitance. Since 40% Pt/C contains less carbon than 20% Pt/C, less carbon support and ionomer are present, leading to lower capacitance at the double layer region.

At 100% RH, both 40% Pt/C SS-CCE and NBE materials have a lower ECSA, when tested at 80 °C compared to room temperature. This is due to higher water content within the system, which affects transport efficiency, that is not seen as readily when tested at room temperature. At both temperatures, SS-CCE shows to have low variation in catalyst layer resistance, while the NBE showed more significant variation.

The SS-CCE was also more stable than the NBE when the RH was varied (at constant cell temperature). Although ECSA was generally lower than that of NBE, SS-CCE proved to have less variability in results when tested using varied RH of inlet fuel and oxygen. When varying the percent of oxygen present at the cathode, the SS-CCE showed greater stability, again, throughout fuel cell performance testing. While the 40% Pt/C NBE displayed higher maximum performance than the SS-CCE, the SS-CCE material showed greater durability and its performance was far less sensitive to variation in operating

conditions. This could be an important benefit in real-world operation of PEMFCs, where the temperatures and operating conditions are less controlled.

Overall, 40% Pt/C SS-CCE is superior to the predecessor 20% Pt/C SS-CCE, and has similar capabilities to 40% Pt/C NBE MEA. Due to the thinner catalyst layer, that utilizes a uniform, and stable ionomer, 40% Pt/C SS-CCE is able to transport mass and ions more efficiently. Although hydrophilicity remains the barrier of the SS-CCE, the MEA is able to perform with stable power output throughout a range of testing conditions. This includes cell temperature, RH and O₂ (g) content at the cathode. The material of interest, SS-CCE, is the more reliable choice when looking at the fraction of carbon support, as well as the ionomer network, within the CL.

Chapter 4. Studying Non-Vulcan Based Catalyst Support

The other component of interest, in this work, is the carbon support and understanding how its morphology and surface area influence catalyst activity. To examine this, an ordered mesoporous carbon (OMC₁₅) was synthesized and compared with the conventional Vulcan XC-72 carbon support. For these experiments, Nafion[®] was used as the ionomer, after which we can ascertain if OMC₁₅ has potential for use in a SS-CCE.

4.1 Morphology and Composition of Carbon Materials

BET analyses were performed to determine SSA and average pore size of the OMC₁₅ materials. Figure 4.1 displays the N₂ adsorption-desorption isotherms for OMC₁₅ and Pt deposited onto OMC₁₅.

When analyzing the BET isotherms, the first indication of a high surface area material is volume of N₂ (g) that has been adsorbed per mass of material, at standard temperature and pressure. The isotherms provided BET SSA's, tabulated in Table 4.1, being 1129 and 778 m²/g for OMC₁₅ and Pt/OMC₁₅. In comparison, SSA values for commercial carbon materials were 219 and 210 m²/g for Vulcan XC-72 and 20% Pt/Vulcan, respectively.⁶⁵ The major contributor to such a large SSA for the OMC₁₅ is its high porosity. This affirms synthesis of the desired material. With Pt deposited onto OMC₁₅, the SSA is reduced due to synthesis methods and Pt particles blocking available pores. Barrett-Joyner-Halenda (BJH) analysis was used to estimate average pore size of OMC₁₅ to be 3.6 nm, whereas literature states that Vulcan XC-72 has a mean pore diameter of 10.4 nm.⁶⁶ This is due to OMC₁₅ having primarily mesopores, and Vulcan a combination

of micro- and mesopores.⁶⁷ The isotherm for OMC₁₅ has a Type II IUPAC classification and shows to have a type H₄ hysteresis loop. The hysteresis indicates the presence of mesopores that obtain a narrow-slit shape.⁵⁹

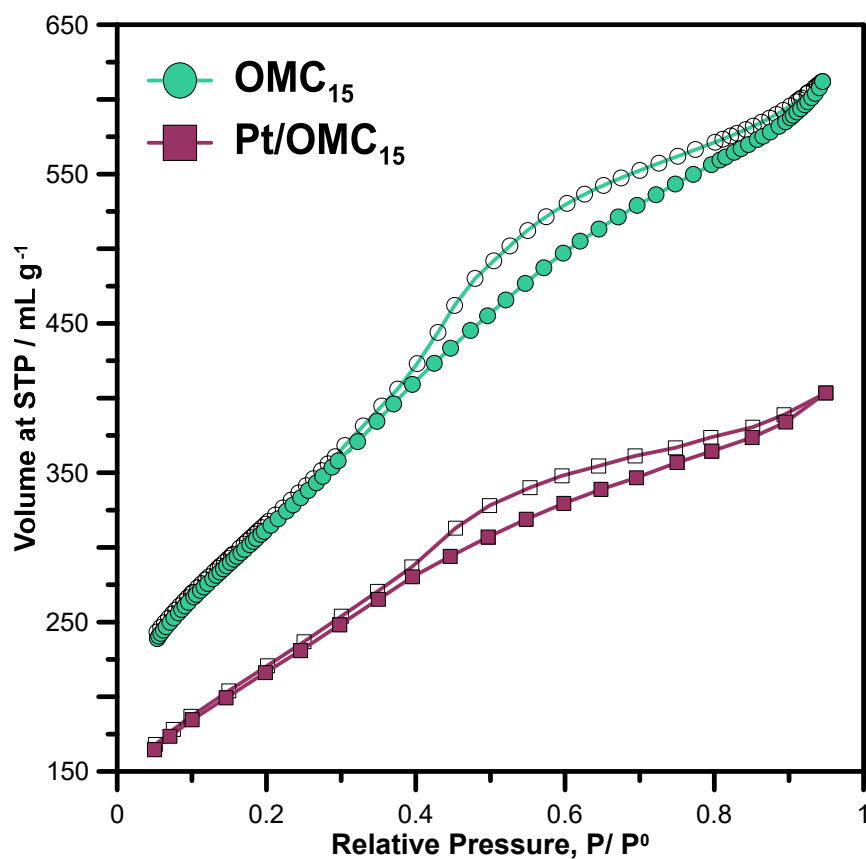


Figure 4.1. Brunauer-Emmett-Teller analyses of OMC₁₅ and Pt/OMC₁₅ showing both adsorption (filled symbols) and desorption (open symbols) curves for measuring SSA.

Table 4.1. Summary of physical properties of the studied catalyst materials.

Catalyst	SSA (m²/g)	Weight Percent Pt on Carbon Support (%)	Average Pt Crystallite Size (nm)
Vulcan XC-72 (Comm.)	219	N/A	N/A
20% Pt/Vulcan (Comm.)	210 ^a	22.90 ± 2.37	2.37 ± 0.43
OMC₁₅	1129	N/A	N/A
Pt/OMC₁₅	778	31.65 ± 2.62	3.25 ± 0.13
^a BET SSA for 20% Pt/Vulcan obtained from J. Kaiser et al. ⁶⁵			

Figure 4.2 displays thermograms, and their derivatives, for OMC₁₅ materials and the commercial Pt/Vulcan comparator. After combustion at 1000 °C, OMC₁₅ had a residual mass of 0.02 wt% ± 6.25, which was attributed to the non-combustible SBA-15 template, that was utilized in the OMC₁₅ synthesis. Pt/OMC₁₅ was determined to have 31.65 wt% ± 2.62 of Pt deposited, which is higher than the desired 20 wt%. Pt/Vulcan (commercial) was determined to have 22.90 wt% ± 2.37 deposition, which is near the provided value of 20 wt%.

The carbon combustion temperatures for each material varies due to the amount of Pt deposited on the support. With Pt deposited onto carbon, the carbon combustion temperature decreases. The onset of combustion for OMC₁₅ occurred at ca. 450 °C, whereas the onset of combustion within Pt/OMC₁₅ occurred at ca. 300 °C. Similarly, 20% Pt/Vulcan has a carbon combustion temperature at ca. 300 °C. The derivative thermograms display that OMC₁₅ and 20% Pt/Vulcan have similar rates of carbon combustion, which are quite rapid. On the contrary, 32% Pt/OMC₁₅ has a carbon combustion rate much slower and more gradual over the temperature increase.

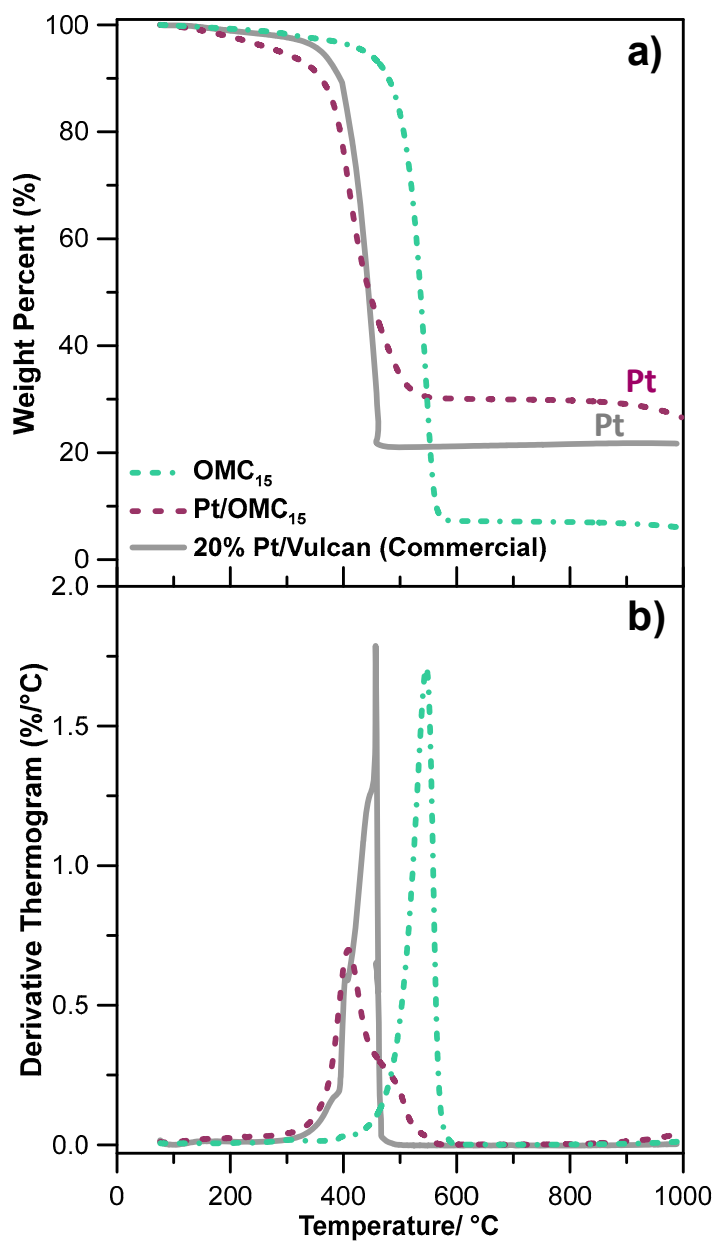


Figure 4.2. OMC₁₅, Pt/OMC₁₅, and 20% Pt/Vulcan (commercial) a) thermograms and b) derivative thermograms to determine Pt loading and residual silica template.

A comparison of SEM imaging for the different carbon supports, OMC₁₅ and Vulcan XC-72, is seen in Figure 4.3. The OMC₁₅ morphology appears to have more rod-like agglomerates that have visibly larger pores between them. These agglomerates have a wide variation in size and shape, with evidence of wide-mouthed surface pores. Vulcan

carbon appears to have a uniform surface with spherical shaped particles, which is similarly seen in literature.⁶⁸

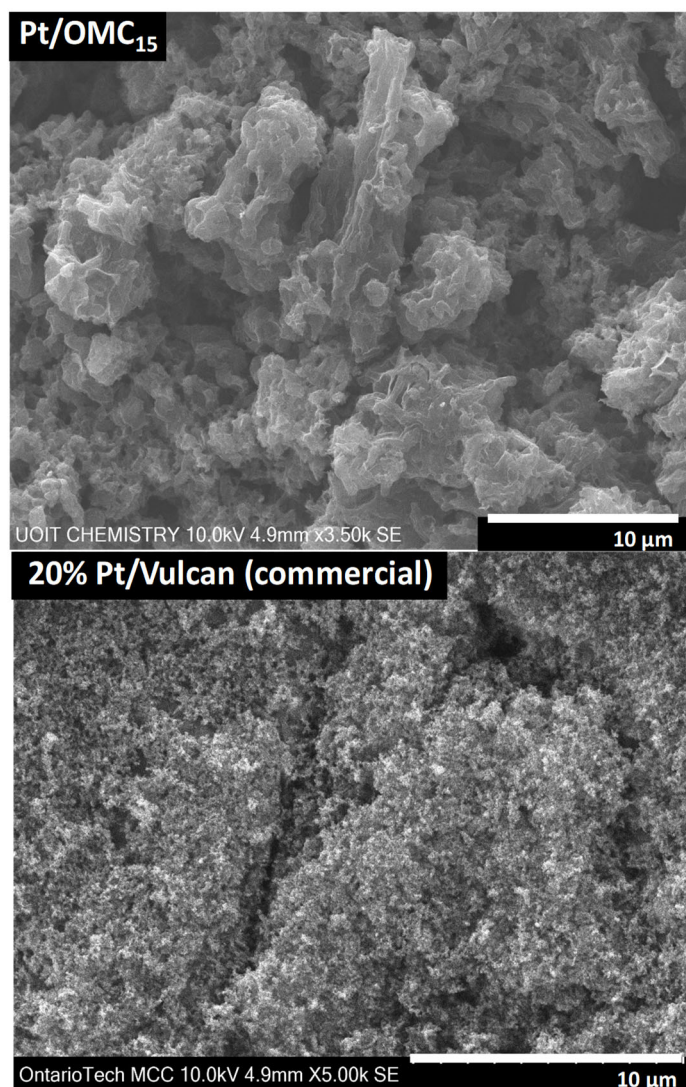


Figure 4.3. Scanning electron microscopy images of Pt/OMC₁₅ and 20% Pt/Vulcan (commercial).

XRD patterns, in Figure 4.4, show that Pt face centered cubic (FCC) peaks are sharper and larger for Pt/OMC₁₅ than that of Pt/Vulcan. This indicates the Pt crystallite

sizes are larger.⁶⁹ Also present in the XRD patterns is the peak shift seen both in the OMC₁₅ {002} carbon facet and the Pt/OMC₁₅ {111} and {220} platinum facets. A shift in the XRD peak means that there is lattice strain. A peak shift towards a higher angle means there is compressive lattice strain, whereas a shift towards lower angles is indicative of expanded lattice strain.⁷⁰ OMC₁₅ is a less graphitic carbon than Vulcan XC-72, indicated by the peak sharpness at the C {002} peak.⁷¹ It also appears to have a lattice strain of expansion, whereas Pt/OMC₁₅ has a compressive lattice strain, compared to commercial material. Platinum crystallite size was estimated using the Scherrer equation for both Pt {111} and {220} peaks. The average crystallite size of Pt, seen in Table 4.1, was calculated to be 2.37 nm \pm 0.43 and 3.25 nm \pm 0.13 for 20% Pt/Vulcan and 32% Pt/OMC₁₅, respectively.

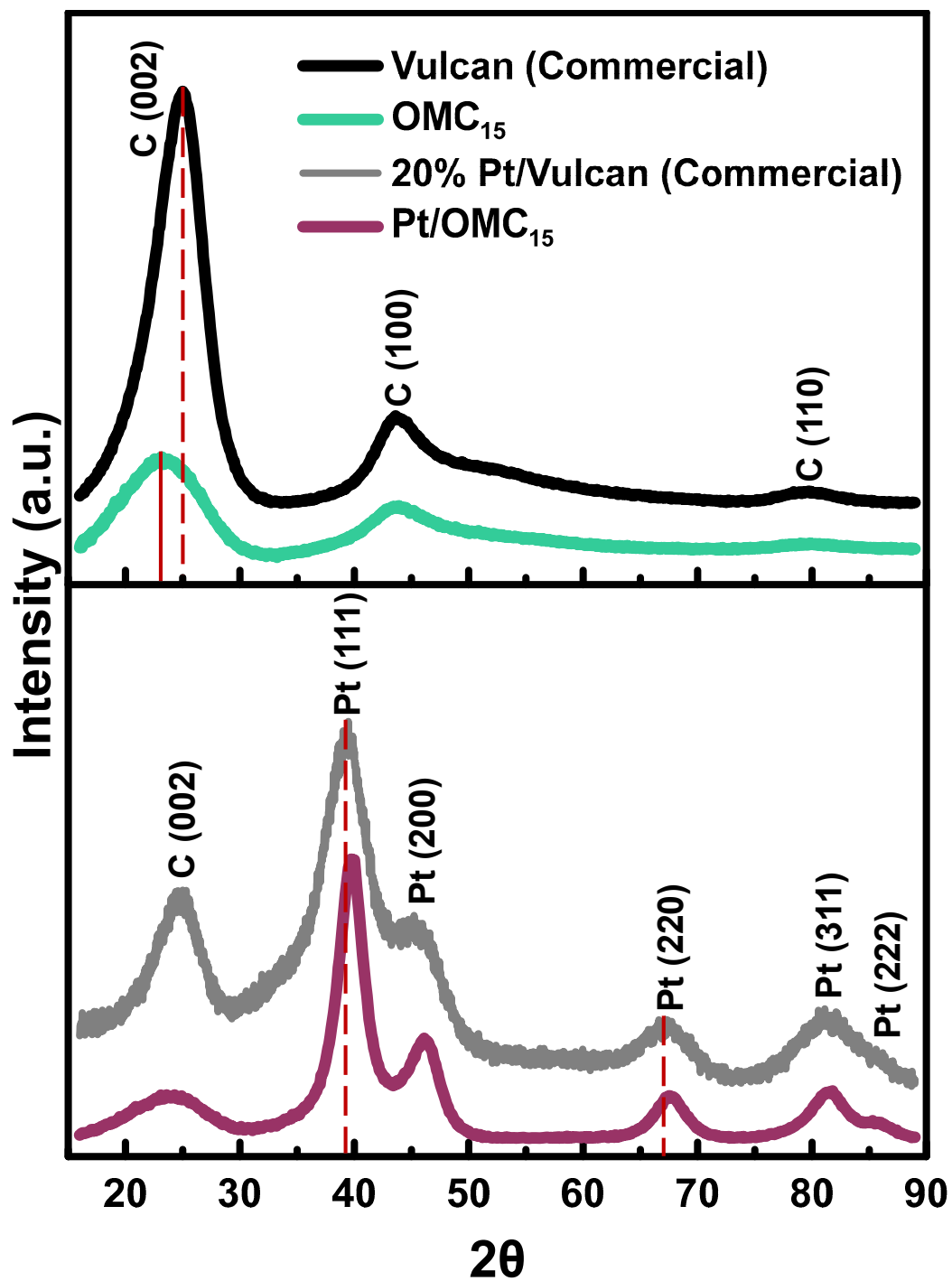


Figure 4.4. Overlaid X-ray diffraction patterns of Vulcan (commercial), OMC₁₅, 20% Pt/Vulcan (commercial) and Pt/OMC₁₅, including Miller Indices of FCC Pt and graphitic C facets.

4.2 Electrochemical Studies on OMC₁₅ Materials

Both platinized carbon materials were characterized through electrochemical testing. CVs of each are plotted in Figure 4.5, where each electrode employed the same mass of Pt, which led to a lower carbon content in the Pt/OMC₁₅ deposition. This is evident when looking at the double-layer region of the CV, with only half the amount of OMC₁₅ than Vulcan, in each deposition, the double-layer capacitance (i.e. 0.425 V vs RHE) is equal. This indicates a very large capacitance present within the Pt/OMC₁₅ catalyst.

The ECSA of each catalyst was calculated, where Pt/OMC₁₅ has an ECSA of 12.3 m²/g and Pt/Vulcan 76.7 m²/g, seen in Table 4.2. The difference in the ECSA of these two catalysts was quite surprising given that XRD analyses indicate the Pt crystallite sizes are similar in size. This indicates that the utilization of the Pt surface area, in the Pt/OMC₁₅, is quite poor. The reason for this poor utilization is not apparent from the CV.

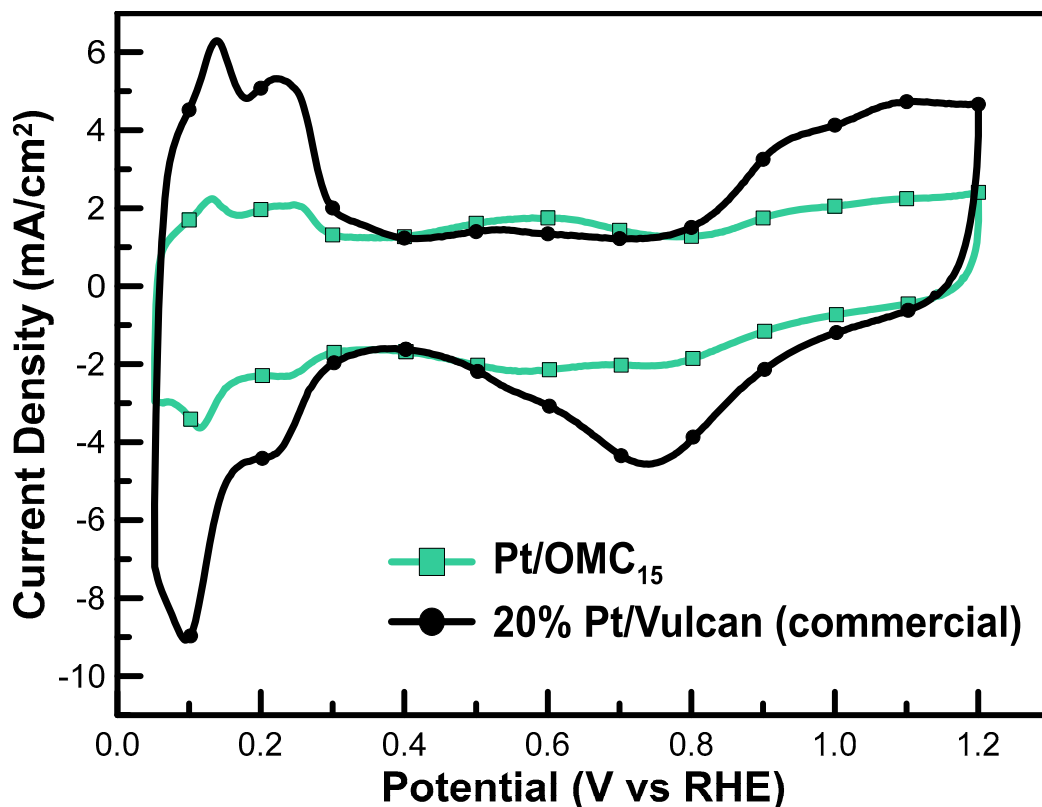


Figure 4.5. Cyclic voltammograms at 100 mV/s in a three-electrode cell configuration with 20% Pt/Vulcan and Pt/OMC₁₅ deposited on a glassy carbon WE, a Pt wire CE and a Hg-HgSO₄ RE tested in N₂(g) purged 0.5 M H₂SO₄.

RDE data for the ORR at the two catalysts is seen in Figure 4.6. This shows that the large difference in ECSA entails lower Pt/OMC₁₅ ORR activity, compared to commercial 20% Pt/Vulcan. Although ORR activity is low, it is better than expected given low Pt utilization. The onset potential for the ORR is determined by finding the potential at the current density of 0.1 mA/cm². Summarized in Table 4.2, the onset potential for Pt/Vulcan is 1.049 V, whereas that for Pt/OMC₁₅ is 0.991 V, with the theoretical oxygen reduction potential being 1.23 V vs RHE.^{72,73} This ORR onset overpotential of ca. 0.2 V vs RHE is commonly observed with Pt catalysts. This is thought to be due to the strong

binding theory, where adsorbed *O and *OH species, from the reduction reactions, are adsorbed on the Pt surface, rendering those active sites unattainable for the O₂ (g).^{15,73}

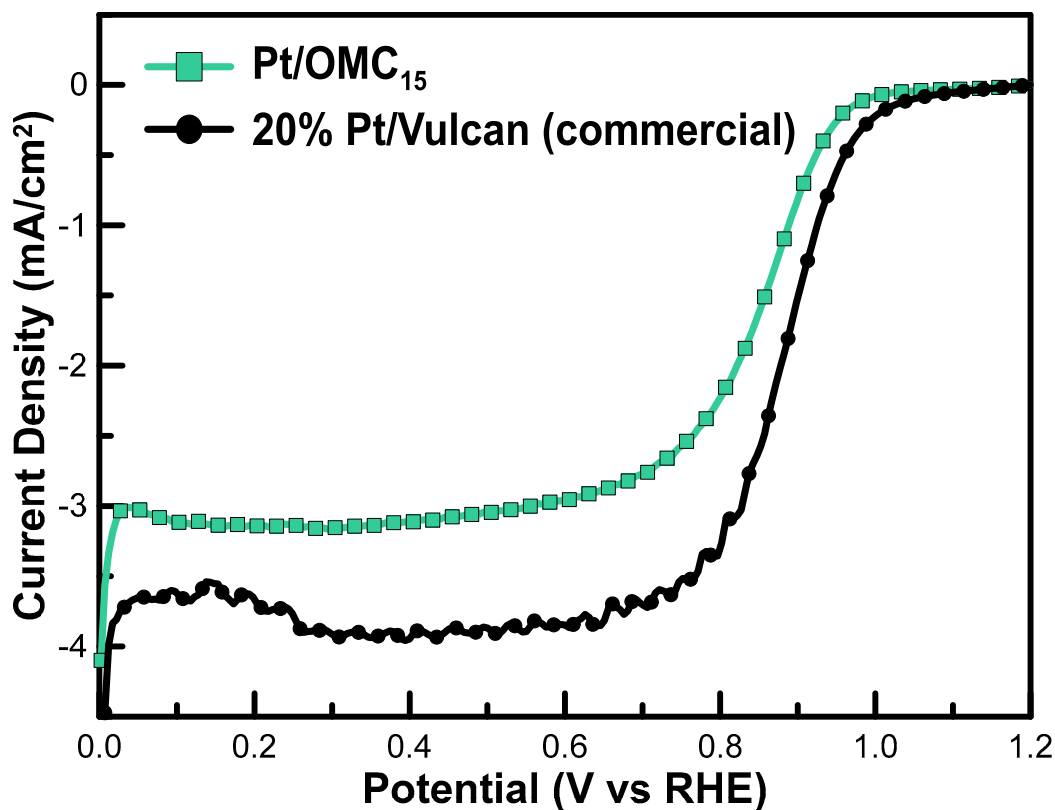


Figure 4.6. Linear sweep voltammograms at 5 mV/s and a rotation rate of 900 RPM in a three-electrode cell configuration with 20% Pt/Vulcan and Pt/OMC₁₅ deposited on a glassy carbon WE, a Pt wire CE and a Hg-HgSO₄ RE tested in N₂ (g) purged H₂SO₄.

Table 4.2. Summary of electrochemical results from CV and ORR LSV.

Catalyst Material	E _{onset}	E _{1/2}	ECSA	i ₉₀₀
	(V vs RHE)	(V vs RHE)	(m ² g ⁻¹)	(mA/cm ²)
Pt/OMC ₁₅	0.991	0.852	12.3	-0.816
20% Pt/ Vulcan	1.049	0.880	76.7	-1.510

With roughly 1/6th ECSA on Pt/OMC₁₅ than Pt/Vulcan, it is expected to have a lower activity towards ORR. Although Pt/OMC₁₅ does have lower activity, the current density at 900 mV (i_{900}) is half of that for Pt/Vulcan. This indicates that the *O and *OH species block more Pt active sites on Pt/Vulcan than on Pt/OMC₁₅. This could be due to the carbon support, OMC₁₅, allowing greater adherence of the reactant species. The half-wave potential for Pt/Vulcan, 0.880 V vs RHE, and Pt/OMC₁₅, 0.852 V vs RHE, continue to present a higher ORR activity with Vulcan as the catalyst support. Although ORR activity is higher with Pt/Vulcan, Pt/OMC₁₅ displays a promising comparison having similar activity even with a lower ECSA of Pt.

To test durability, each catalyst was subjected to an accelerated stress test (AST). The AST used here involved cycling the potential 5000 times between 0.0 and 1.2 V vs RHE, while periodically assessing electrode health by CV and EIS. Figure 4.7 displays CV assessments for each catalyst. As seen in the initial CVs, the ECSA for Pt/OMC₁₅ is considerably lower than Pt/Vulcan. A comparison of the ECSA values is displayed in Figure 4.8. This shows that both catalysts observe a decline in ECSA throughout AST. When compared at a percentage of initial ECSA over the cycle numbers, Pt/OMC₁₅ displays a ca. 79% loss, whereas Pt/Vulcan has an ECSA loss of 48% from initial.

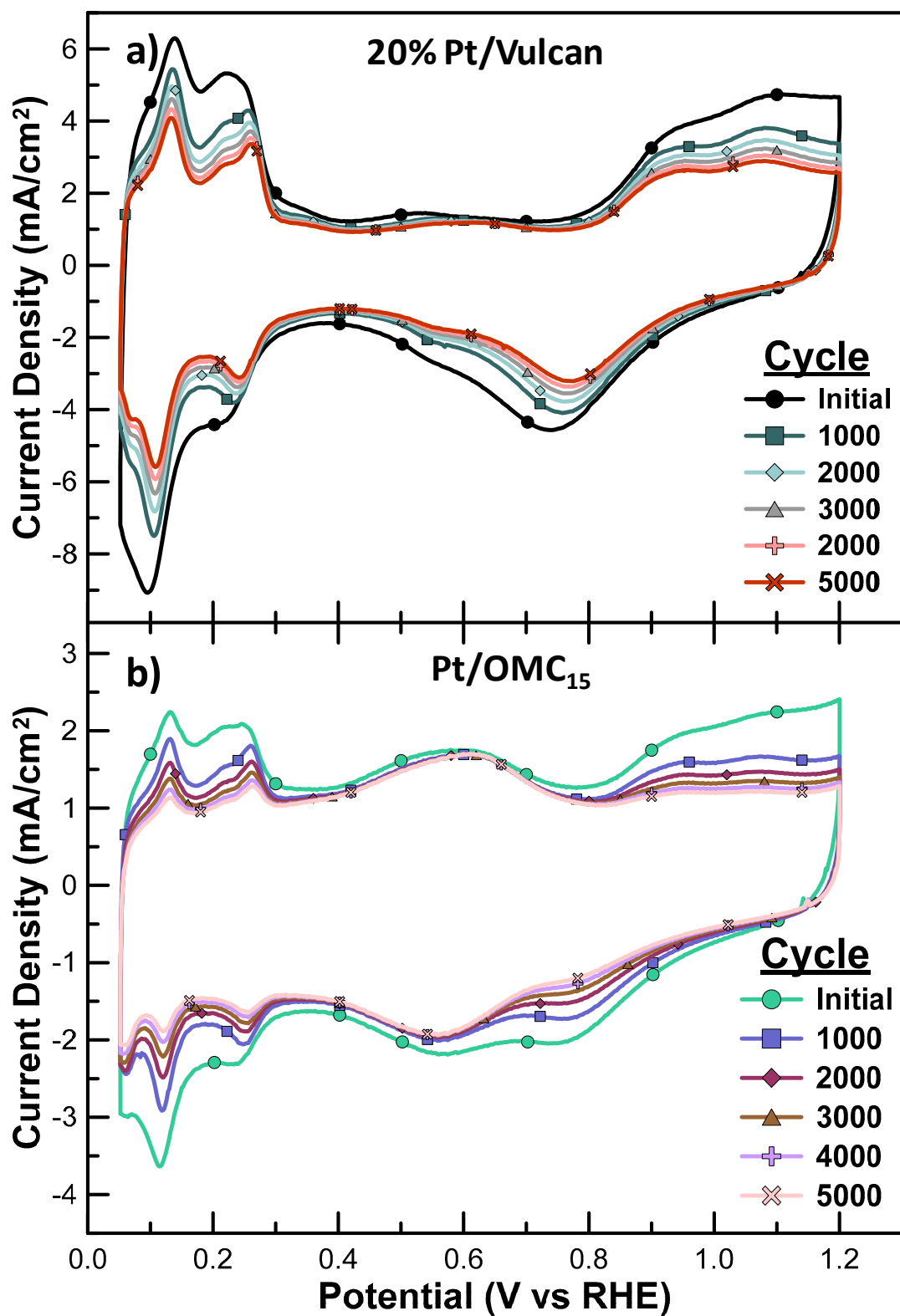


Figure 4.7. Cyclic voltammograms at 100 mV/s in a three-electrode cell configuration with a) 20% Pt/Vulcan and b) Pt/OMC₁₅ deposited on a glassy carbon WE, a Pt wire CE and a Hg-HgSO₄ RE tested throughout AST in N₂ (g) purged H₂SO₄.

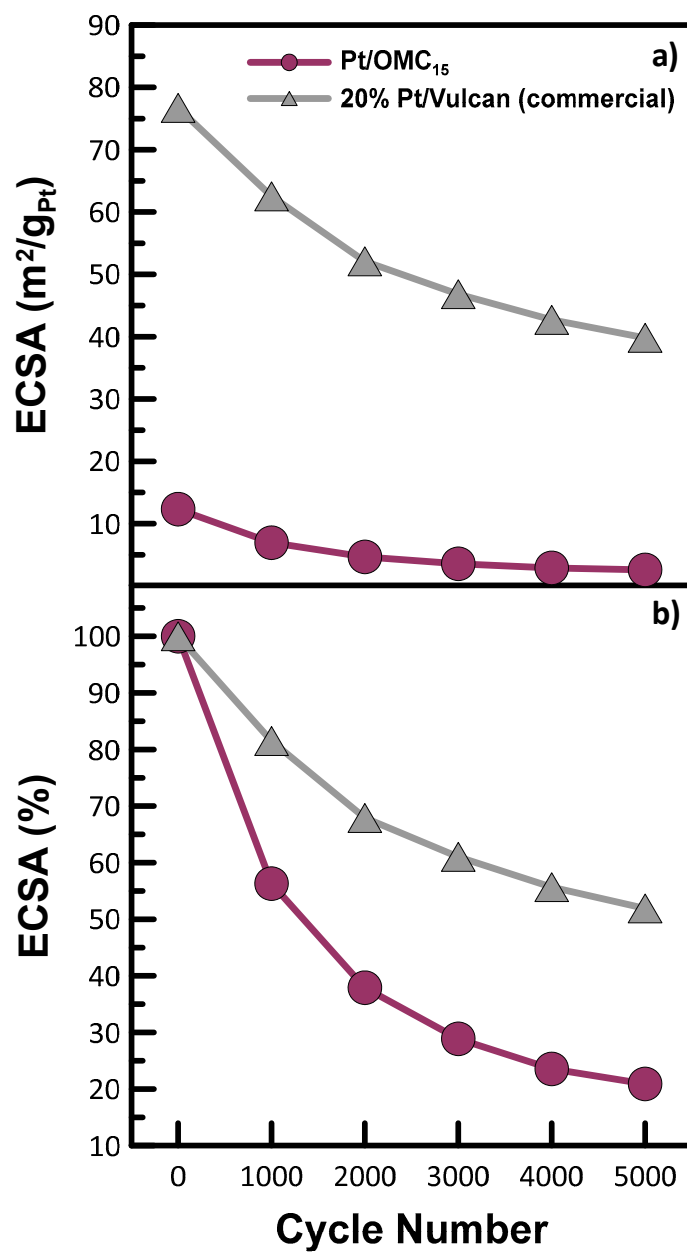


Figure 4.8. ESCA patterns at each CV cycle number with displays of a) ECSA in m²/g_{Pt}, and b) percent decay from initial ECSA.

EIS studies at the double layer region, seen in Figures 4.9 and 4.10, display Nyquist, capacitance, and normalized capacitance plots for Pt/Vulcan and Pt/OMC₁₅, respectively. There is not much change seen in the Nyquist plot for Pt/Vulcan, other than an initial decrease before hydration of the catalyst layer occurred.⁷⁴ The Warburg length remains

stable throughout AST. The capacitance plot displays a slight decrease in limiting capacitance, which is attributed to change within the Vulcan carbon support. The resistance within the carbon remains stable, as seen in the normalized capacitance plot.

Nyquist data from EIS testing of Pt/OMC₁₅ shows minimal change in resistance of OMC₁₅. Limiting capacitance remains stable throughout AST, which indicates high stability of OMC₁₅. Pt/OMC₁₅ acquires a much larger limiting capacitance, at ca. 12 mF/cm², than that of Pt/Vulcan, at an average of ca. 8 mF/cm². Normalized capacitance data further indicates no change to resistance within the carbon support throughout testing.

Summarizations of the EIS data is seen in Figure 4.11 a) and b), where the degradation patterns are displayed throughout each 1000 cycle step. Both carbon supports appear to have a slight increase in R_{Σ} (i.e. ionic resistance), but remain fairly stable over time. Limiting capacitance of each catalyst support also remain quite stable, with a slightly larger decrease in Vulcan after 5000 cycles. This comparison demonstrates that, although Vulcan is known to be a very stable material⁷⁵, the very high surface area OMC₁₅ has less degradation over a period of 5000 cycles.

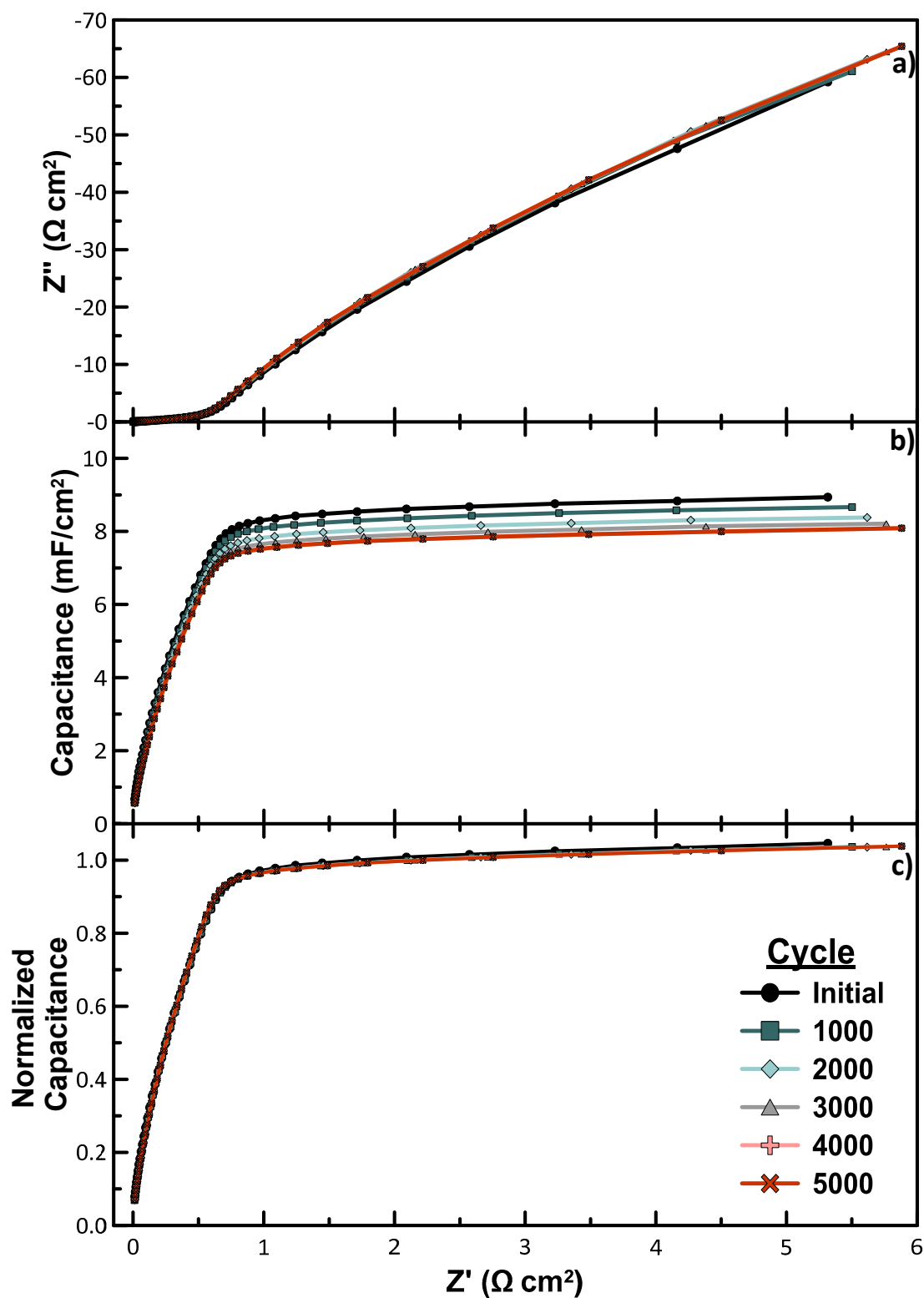


Figure 4.9. EIS comparison for 20% Pt/Vulcan (commercial) tested throughout AST in a three-electrode configuration displaying a) Nyquist, b) capacitance, and c) normalized capacitance plots measured at a DC bias of 0.425 V.

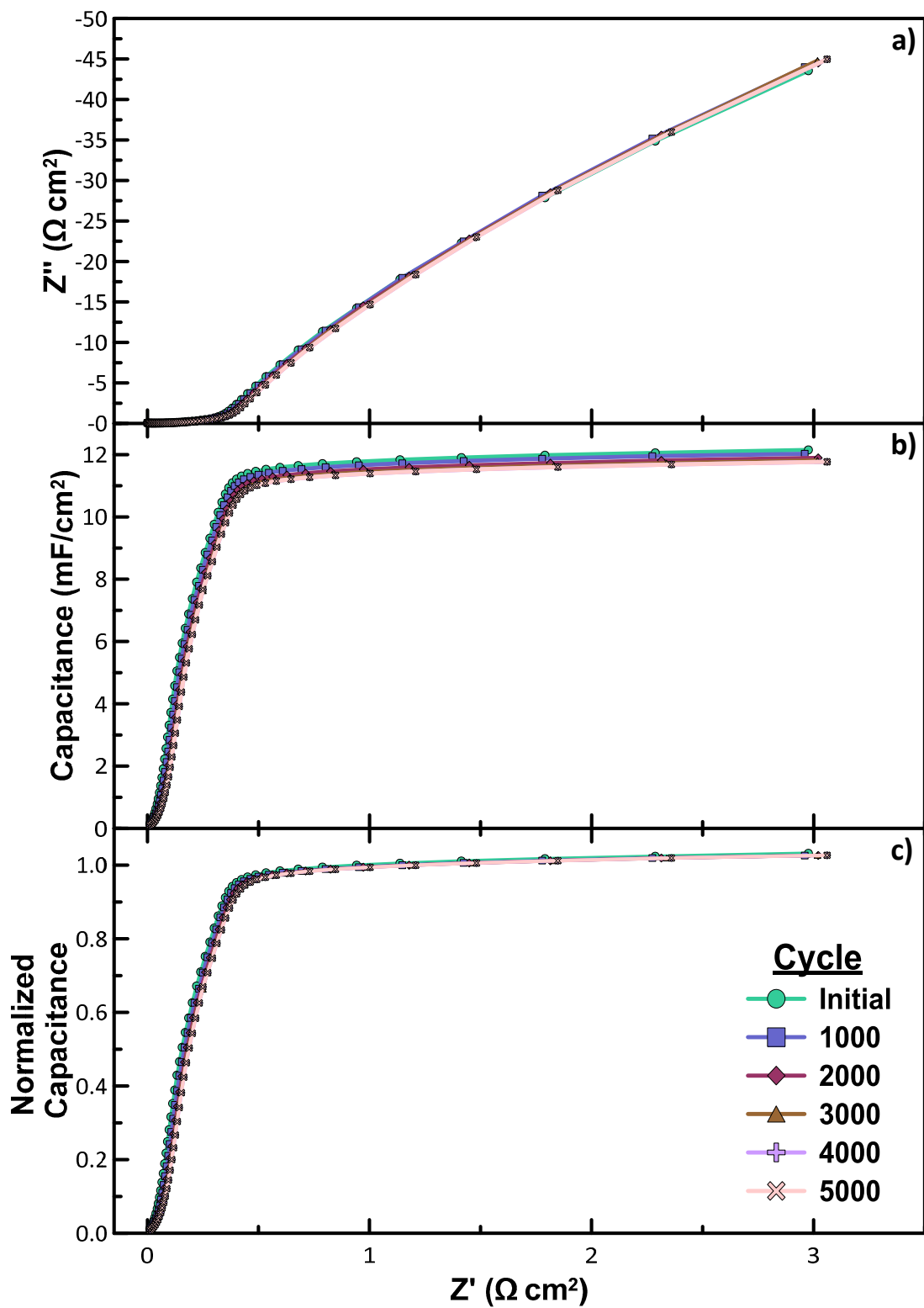


Figure 4.10. EIS comparison for Pt/OMC₁₅ tested throughout AST in a three-electrode configuration displaying a) Nyquist, b) capacitance, and c) normalized capacitance plots measured at a DC bias of 0.425 V.

Since the EIS data indicates a stable carbon support found within both catalysts, the decrease in ECSA must be attributed to Pt ripening, dissolution and agglomeration.^{75,76} This is explicitly apparent within the Pt/OMC₁₅ catalyst that shows a large decrease in ECSA, throughout AST, but obtains an inherently stable carbon support. This is likely due to the lack of defects on OMC₁₅. Defects are generally oxygen containing functional groups on the carbon surface. During deposition, Pt interacts with these sites, leading to stronger attachment of Pt nanoparticles (NPs) to the carbon surface. Without good adsorption of Pt onto OMC₁₅, the Pt will readily dissociate and either agglomerate to form larger and less active Pt NPs, or it will leach into the electrolyte solution.

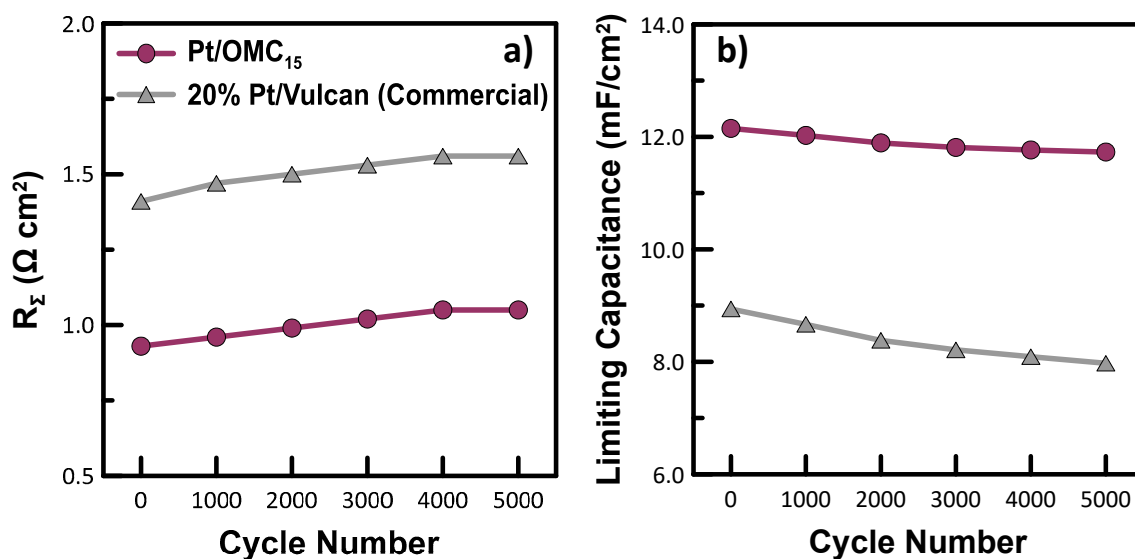


Figure 4.11. Comparison of EIS - derived data at a DC bias of 0.425 V displaying the a) total resistance and b) limiting capacitance of both 20% Pt/Vulcan (commercial) and Pt/OMC₁₅.

ORR activity was recorded before and after 5000 cycles of CV, summarized in table 4.3. A change in activity is observed for both catalysts, where both the onset potential and

half-wave potentials decrease. The half-wave potential for Pt/Vulcan declines by 0.035 V, after 5000 cycles, whereas Pt/OMC₁₅ has a decrease of 0.116 V. The difference in onset potential for Pt/Vulcan is 0.063 V, and that for Pt/OMC₁₅ is 0.045 V. Linear sweep voltammograms were analyzed to obtain the summary, seen in Figure 4.12.

Table 4.3. Summary of electrochemical results for testing Pt/OMC₁₅ and 20% Pt/Vulcan before and after AST.

	Pt/OMC ₁₅		20% Pt/ Vulcan	
	Before AST	After AST	Before AST	After AST
E_{onset} (V vs RHE)	0.991	0.945	1.049	0.986
ΔE_{onset} (V vs RHE)	0.045		0.063	
E_{1/2} (V vs RHE)	0.852	0.736	0.880	0.845
$\Delta E_{1/2}$ (V vs RHE)	0.116		0.035	
i₉₀₀ (mA/cm²)	-0.816	-0.253	-1.510	-0.814
Δi_{900} (mA/cm²)	-0.562		-0.696	

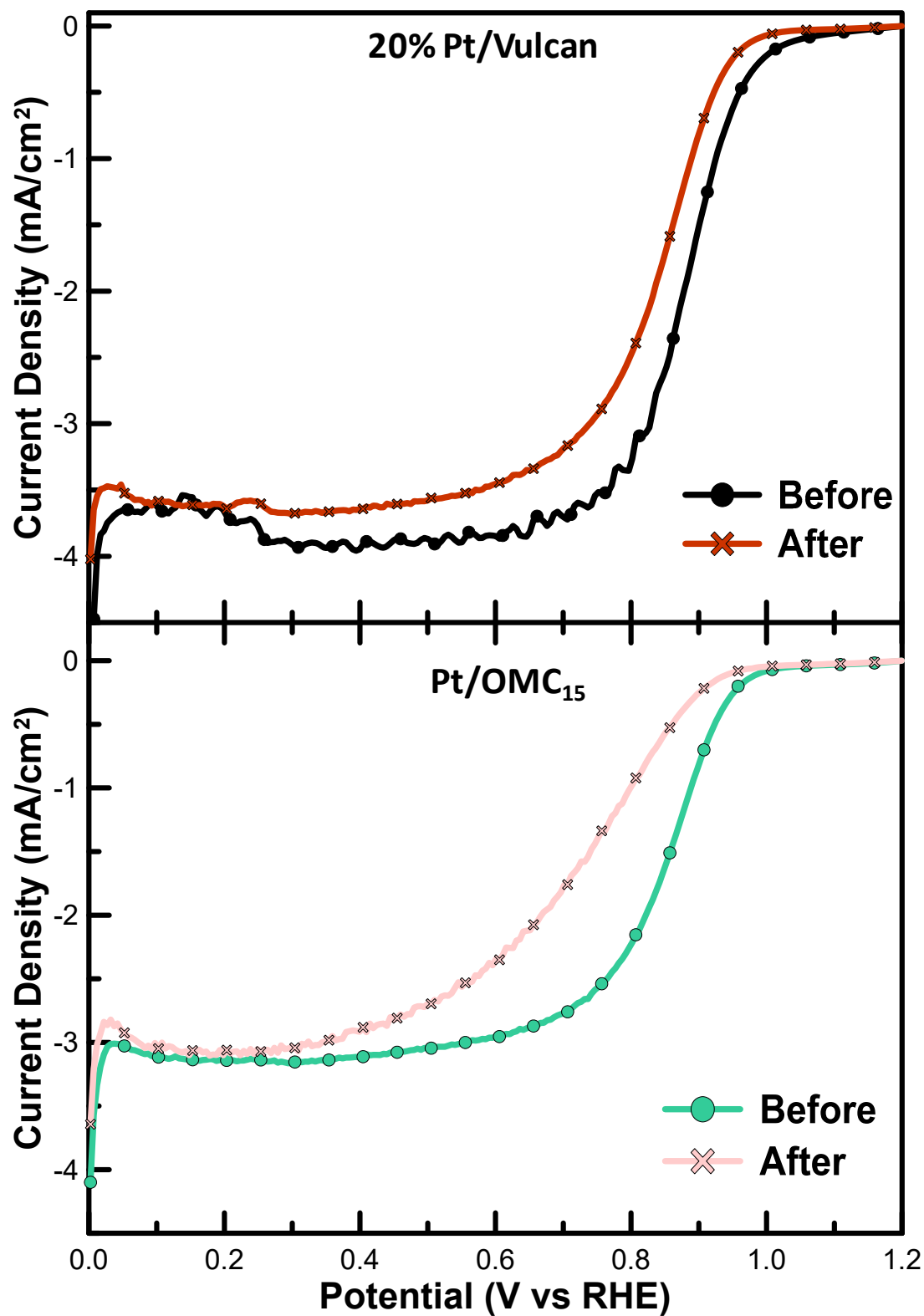


Figure 4.12. Linear sweep voltammograms at 5 mV/s and a rotation rate of 900 RPM in a three-electrode cell configuration with 20% Pt/Vulcan and Pt/OMC₁₅ deposited on a glassy carbon WE, a Pt wire CE and a Hg-HgSO₄ RE tested before and after AST in N₂ (g) purged H₂SO₄.

4.3 Summary

SEM images of OMC₁₅ show large vacancies and surface depth variations, making it an uneven surface. With a rougher surface, it might be difficult to deposit Pt, being that nucleation sites may be obstructed with other agglomerates, or hidden within the crevices. ECSA values indicate that Pt utilization appears to be low for Pt/OMC₁₅, due to either proton or electron transport inefficiencies, at the few available Pt sites. The lattice strain, seen in the XRD patterns, within OMC₁₅ may contribute to poor Pt anchoring to any available nucleation sites. This means there may not be enough defects on the OMC₁₅ surface, which ultimately would lead to the larger Pt particles forming.

Although synthesis is proprietary, the Vulcan surface appears to be highly uniform with greater accessibility to nucleation sites. The uniform surface is visible on the SEM image, showing few crevices and primarily micropores. This would benefit the Pt adsorption process during deposition, leading to great ECSA values of Pt/Vulcan. This provides grounds for a strong support-to-catalyst interaction, whereas OMC₁₅ displays low ECSA due to poor Pt anchoring.

Overall, OMC₁₅ shows to be a characteristically highly capacitive material. Although TGA concluded that the catalyst is 32% Pt/OMC₁₅, the Pt itself was not well anchored to the support. This led to Pt dissolution and agglomeration which ultimately gave poor ECSA. ORR activity was surprisingly unaffected by the low ECSA, which could be due to the lattice strain in OMC₁₅. The carbon support itself appeared to be stable when put under the electrochemical stress test. The issue is that the OMC₁₅ lacks defects and good nucleation sites, being heteroatoms, particularly O. Therefore, the OMC₁₅ may need to be doped with oxygen in order to enhance Pt adsorption so that it can perform as a fuel cell

catalyst. Along with this, the Pt NPs are very similar in size to the pore diameter. This could lead to difficulty in accessing any Pt within the pores of OMC₁₅. Whereas, Pt/Vulcan has good Pt utilization because the average pore diameter is about four times larger than the Pt NPs.

Given the lack of defect sites and the small pore sizes, OMC₁₅ appears to be a poor choice for an electrocatalyst support, for the PEMFC. In future, OMC's with larger mesopores, on the order of 10+ nm, may be better suited for fuel cells. However, due to the high surface area and large capacitance of OMC₁₅, this material has potential in supercapacitor applications. Being able to hold charge, while remaining stable, suggests that this very interesting high SSA carbon may be useful in other fields.

Chapter 5. Conclusions and Future Directions

The overall goal of this research was to better understand the role of carbon support within SS-CCEs. To do this, I first modified the Pt-to-C ratio in an SS-CCE using a Vulcan based catalyst. 40% Pt/C SS-CCE allowed for preparation of a thinner CL, which was able to out perform the MEA with a thicker CL, 20% Pt/C SS-CCE. This supported that the hypothesis of creating a smaller barrier for H^+ and e^- permeability provided increased efficiency, and therefore enhanced performance.

Continued studies on the SS-CCE compared the ionomer and binder to the conventionally Nafion[®]-bound electrode. While the performance of SS-CCE made from 40% Pt/C was not greater than that of the NBE, it did prove to be less sensitive to variation in operating conditions. Although 40% Pt/C SS-CCE displayed decent performance, and stability, over a wide range of operating conditions, accelerated stress tests (AST) will aid in further understanding the durability of the material. Recent AST studies on 20% Pt/C SS-CCE have shown that the silica network indeed increases durability, through stabilizing the catalyst which reduces carbon corrosion reactions in the CL.⁷⁷ In order to test durability of the material, a similar AST method, as the one implemented for OMC₁₅, could be applied. The scanned potential of 0.05 to 1.35 V vs RHE would provide appropriate conditions to study carbon corrosion and Ostwald ripening of Pt NP.⁷⁸ Performing the AST in a PEMFC configuration would also be beneficial and enable direct assessment of its impact on fuel cell performance.

Through implementation of the higher potential range AST protocol, studies have shown that whilst using a hydrothermal synthetic route, the SS-CCE MEA is able to outperform a NBE MEA, both before and after 5000 cycles.⁴⁸ The SS-CCE using 20% Pt/C,

in that study, also shows to have a higher ECSA of Pt, with a much lower percent loss after the 5000 cycle AST. Knowing that 40% Pt/C SS-CCE provides a thinner catalyst layer and enhanced performance, compared to that using a 20% Pt/C, it may be beneficial to try the hydrothermal method in preparation of a new catalyst layer.^{48,49} Along with this, the ionomer-to-carbon ratio is something that was optimized, but materials could always benefit from further optimization studies. Therefore, if preparing a new SS-CCE catalyst, one would benefit from using 40% Pt/C in a total of $\leq 20\%$ silane ionomer, all within an autoclave reactor where the hydrothermal method may take place. These steps would further enhance PEMFC performance, with the removal of Nafion[®] from the CL altogether, and optimizing CL thickness.

Subsequently, I examined a novel carbon support material, OMC₁₅. An OMC₁₅ was selected due to its ordered mesoporosity, which could be beneficial for the SS-CCE. The OMC₁₅ was synthesized, after which Pt was deposited. It was first tested to discover the possible benefits of a highly porous and large SSA carbon, as a Pt support. Although the results were not expected, it was discovered that OMC₁₅, as a support, aided the ORR, which could be means of further research, altogether.

When using OMC₁₅, compared to Vulcan, slightly less variation is seen in the electrochemical results, throughout the duration of stress testing. This indicates that OMC₁₅ has great stability. Future AST measurements should employ a higher upper potential limit (e.g. 1.5 V) in order to determine if the OMC₁₅ is less prone to carbon corrosion compared to Vulcan carbon.

In order to combine Pt/OMC₁₅ with SS-CCE, optimization of the Pt/OMC₁₅ catalyst must be continued. One procedural step that needs modification is the deposition of Pt onto

the OMC₁₅ support. Different methods have proven to be successful when depositing Pt, or Pt alloys, onto a carbon support, including: chemical vapour deposition, Pt NP synthesis and deposition with use of a stabilizer, magnetron sputtering method, partial galvanic replacement of Ni by Pt, and many more.^{79–82} Before finding an appropriate Pt deposition technique, this may require OMC₁₅ surface modification with other elements, similar to nitrogen-doped carbon nanotubes, which enhances Pt deposition and stability.⁷⁶ To complete the attempt of implementing Pt/OMC as a fuel cell catalyst, there are other forms of mesoporous carbon that can be used in place of OMC₁₅. This includes OMC₁₆, that obtains a higher surface area from a larger surfactant precursor, as well as colloid imprinted carbons, synthesized through silica colloid imprinting.⁸³ Along with those, TTK carbon is a high SA Ketjenblack[®]-based material that showed promise when implemented in a NBE.⁸⁴ The study provided evidence that utilization of such carbon, with 47% Pt, can enhance PEMFC activity, greatly. Leading to the final potential barrier, within the OMC₁₅, the amount of Pt deposited. Optimizing the Pt-to-C ratio in the catalyst layer may alter electronics between the Pt and C enough to observe more expected results.

Since OMC₁₅ posed a great challenge for implementation into a PEMFC, it may be useful to study the material in other fields. Ones that require an inexpensive, stable and high SSA material. Although the material is not useful in energy conversion, it may have useful properties in energy storage, such as in the ever-growing supercapacitor application. Since it is not out of sight to be able to store energy, OMC₁₅ may also be useful in storing pollutants. Although binding sites on OMC₁₅ remains an issue, further investigation may provide an inexpensive and environmentally-friendly replacement to conventional materials.³²

Both SS-CCE and OMC₁₅ materials, on their own, exhibit low ECSA when tested, but obtain similar, or remarkable, activity when implemented in the PEMFC, or for the ORR, compared to commercial standards. They also both exhibit high capacitance, with low variation, at different operating conditions. When OMC₁₅ is used within SS-CCE, it is presumed a very large capacitance will be present. This provides means for future work on supercapacitor capabilities. Knowing that SS-CCE is stable at varying temperature and RH, and OMC₁₅ is stable under electrochemical stress tests, both in acidic media, it is reasonable to assume that when combined they will show resilience under different operating conditions. Overall, the future goal will be to determine whether, or not, the combination of OMC₁₅ with the SS-CCE material would be a success.

References

1. Appleby, A. J. From Sir William Grove to today: Fuel cells and the future. *J. Power Sources* **29**, 3–11 (1990).
2. Williams, M. C., Strakey, J. P. & Surdoval, W. A. The U.S. Department of Energy, Office of Fossil Energy Stationary Fuel Cell Program. *J. Power Sources* **143**, 191–196 (2005).
3. Shafiee, S. & Topal, E. When will fossil fuel reserves be diminished? *Energy Policy* **37**, 181–189 (2009).
4. Hultman, M. & Nordlund, C. Energizing technology: Expectations of fuel cells and the hydrogen economy, 1990-2005. *Hist. Technol.* **29**, 33–53 (2013).
5. Eudy, L. & Post, M. Fuel Cell Buses in U . S . Transit Fleets : Current Status 2014 Fuel Cell Buses in U . S . Transit Fleets : Current Status 2014. (2014).
6. Wagner, F. T., Lakshmanan, B. & Mathias, M. F. Electrochemistry and the future of the automobile. *J. Phys. Chem. Lett.* **1**, 2204–2219 (2010).
7. UNFCCC. Paris Agreement. *Conf. Parties its twenty-first Sess.* **21932**, 32 (2015).
8. Crowley, T. J. Causes of Climate Change Over the Past 1000 Years. *Science* (80-.). **289**, 270–277 (2000).
9. Cleaveland, M. K. Plain Facts About Anthropogenic Global Climate Change and Warming: A Review. *J. Ark. Acad. Sci.* **70**, 64–76 (2016).
10. Ajanovic, A. & Haas, R. Economic and Environmental Prospects for Battery Electric- and Fuel Cell Vehicles: A Review. *Fuel Cells* **19**, 515–529 (2019).
11. Martin, K. E., Kopasz, J. P., Mcmurphy, K. W., Cells, F. & Technologies, I. Status of Fuel Cells and the Challenges Facing Fuel Cell Technology Today. in *Fuel Cell Chemistry and Operation* (eds. Herring, A. M., Zawodzinski, T. A. & Hamrock, S. J.) **1040**, 1–13 (2010).
12. Peron, J., Shi, Z. & Holdcroft, S. Environmental Science Hydrocarbon proton conducting polymers for fuel cell catalyst layers. *Energy Environ. Sci.* **4**, 1575–1591 (2011).
13. Ioroi, T., Siroma, Z., Yamazaki, S. & Yasuda, K. Electrocatalysts for PEM Fuel Cells. *Adv. Energy Mater.* **9**, 1801284 (2019).
14. Schmidt, T. J., Paulus, U. A., Gasteiger, H. A. & Behm, R. J. The oxygen reduction reaction on a Pt/carbon fuel cell catalyst in the presence of chloride anions. *J. Electroanal. Chem.* **508**, 41–47 (2001).
15. Nørskov, J. K. *et al.* Origin of the overpotential for oxygen reduction at a fuel-cell cathode. *J. Phys. Chem. B* **108**, 17886–17892 (2004).
16. Reid, O. Investigation of an Alternative Sulfonated Silane in Ceramic Carbon

Electrodes for Fuel Cell Applications. (University of Ontario Institute of Technology, 2015).

17. Shimizu, R. *et al.* Durability and degradation analysis of hydrocarbon ionomer membranes in polymer electrolyte fuel cells accelerated stress evaluation. *J. Power Sources* **367**, 63–71 (2017).
18. Aoki, M., Uchida, H. & Watanabe, M. Decomposition mechanism of perfluorosulfonic acid electrolyte in polymer electrolyte fuel cells. *Electrochem. commun.* **8**, 1509–1513 (2006).
19. Li, Y. *et al.* Self-Healing Proton-Exchange Membranes Composed of Nafion–Poly(vinyl alcohol) Complexes for Durable Direct Methanol Fuel Cells. *Adv. Mater.* **30**, 1–7 (2018).
20. Barati, S., Abdollahi, M., Khoshandam, B. & Mehdipourghazi, M. Highly proton conductive porous membranes based on polybenzimidazole/ lignin blends for high temperatures proton exchange membranes: Preparation, characterization and morphology- proton conductivity relationship. *Int. J. Hydrogen Energy* **43**, 19681–19690 (2018).
21. Alipour Moghadam Esfahani, R., Fruehwald, H. M., Afsahi, F. & Easton, E. B. Enhancing fuel cell catalyst layer stability using a dual-function sulfonated silica-based ionomer. *Appl. Catal. B Environ.* **232**, 314–321 (2018).
22. Samad, S. *et al.* Carbon and non-carbon support materials for platinum-based catalysts in fuel cells. *Int. J. Hydrogen Energy* **43**, 7823–7854 (2018).
23. Soo, L. T., Loh, K. S., Mohamad, A. B., Daud, W. R. W. & Wong, W. Y. An overview of the electrochemical performance of modified graphene used as an electrocatalyst and as a catalyst support in fuel cells. *Appl. Catal. A Gen.* **497**, 198–210 (2015).
24. Samad, S. *et al.* Carbon and non-carbon support materials for platinum-based catalysts in fuel cells. *Int. J. Hydrogen Energy* **43**, 7823–7854 (2018).
25. Alipour Moghadam Esfahani, R., Ebralidze, I. I., Specchia, S. & Easton, E. B. A fuel cell catalyst support based on doped titanium suboxides with enhanced conductivity, durability and fuel cell performance. *J. Mater. Chem. A* **6**, 14805–14815 (2018).
26. Calvillo, L. *et al.* Synthesis and performance of platinum supported on ordered mesoporous carbons as catalyst for PEM fuel cells: Effect of the surface chemistry of the support. *Int. J. Hydrogen Energy* **36**, 9805–9814 (2011).
27. Shahgaldi, S. & Hamelin, J. Improved carbon nanostructures as a novel catalyst support in the cathode side of PEMFC: A critical review. *Carbon N. Y.* **94**, 705–728 (2015).
28. Mesa, M., Sierra, L., Patarin, J. & Guth, J. L. Morphology and porosity characteristics control of SBA-16 mesoporous silica. Effect of the triblock surfactant Pluronic F127 degradation during the synthesis. *Solid State Sci.* **7**, 990–

997 (2005).

29. Benzigar, M. R. *et al.* Recent advances in functionalized micro and mesoporous carbon materials: Synthesis and applications. *Chemical Society Reviews* **47**, 2680–2721 (2018).
30. Ryoo, R., Joo, S. H., Kruk, M. & Jaroniec, M. Ordered Mesoporous Carbons. *Adv. Mater.* **13**, 677–681 (2001).
31. Ma, T.-Y., Liu, L. & Yuan, Z.-Y. Direct synthesis of ordered mesoporous carbons. *Chem. Soc. Rev.* **42**, 3977–4003 (2013).
32. Shou, W., Guo, R., Pan, H. & Gang, D. D. Ordered Mesoporous Carbon: Fabrication, Characterization, and Application as Adsorbents. *Dekker Encycl. Nanosci. Nanotechnology, Third Ed.* 1–14 (2015). doi:10.1081/e-enn3-120053279
33. Liang, C., Li, Z. & Dai, S. Mesoporous carbon materials: Synthesis and modification. *Angew. Chemie - Int. Ed.* **47**, 3696–3717 (2008).
34. Lebedeva, N. P., Booij, A. S. & Janssen, G. J. M. Cathodes for Proton-Exchange-Membrane Fuel Cells based on Ordered Mesoporous Carbon Supports. in *ECS Transactions* **16**, 2083–2092 (ECS, 2008).
35. Song, S. *et al.* Effect of pore morphology of mesoporous carbons on the electrocatalytic activity of Pt nanoparticles for fuel cell reactions. *Appl. Catal. B Environ.* **98**, 132–137 (2010).
36. Ding, J., Chan, K. Y., Ren, J. & Xiao, F. S. Platinum and platinum-ruthenium nanoparticles supported on ordered mesoporous carbon and their electrocatalytic performance for fuel cell reactions. *Electrochim. Acta* **50**, 3131–3141 (2005).
37. Yoda, T. *et al.* Gas diffusion electrodes containing sulfonated poly (arylene ether) ionomer for PEFCs. Part 1. Effect of humidity on the cathode performance. *Electrochim. Acta* **54**, 4328–4333 (2009).
38. Peron, J., Edwards, D., Besson, A., Shi, Z. & Holdcroft, S. Microstructure–Performance Relationships of sPEEK-Based Catalyst Layers. *J. Electrochem. Soc.* **157**, B1230 (2010).
39. Tsionsky, M., Gun, G., Glezer, V. & Lev, O. Sol-Gel-Derived Ceramic-Carbon Composite Electrodes: Introduction and Scope of Applications. *Anal. Chem.* **66**, 1747–1753 (1994).
40. Buckley, A. M. & Greenblatt, M. The sol-gel preparation of silica gels. *J. Chem. Educ.* **71**, 599–602 (1994).
41. Hench, L. L. & West, J. K. The Sol-Gel Process. *Chem. Rev.* **90**, 33–72 (1990).
42. Anderson, M. L., Stroud, R. M. & Rolison, D. R. Enhancing the Activity of Fuel-cell Reactions by Designing Three-dimensional Nanostructured Architectures: Catalyst-modified Carbon - Silica Composite Aerogels. *Nano Lett.* **2**, 235–240 (2002).

43. Rabinovich, L. & Lev, O. Sol-gel derived composite ceramic carbon electrodes. *Electroanalysis* **13**, 265–275 (2001).
44. Eastcott, J. I. & Easton, E. B. Electrochemical studies of ceramic carbon electrodes for fuel cell systems: A catalyst layer without sulfonic acid groups. *Electrochim. Acta* **54**, 3460–3466 (2009).
45. Eastcott, J. I., Powell, J. A., Vreugdenhil, A. J. & Easton, E. B. Electrochemical and Morphological Studies of Ceramic Carbon Electrodes for Fuel Cell Systems. *ECS Trans.* **41**, 853–864 (2011).
46. Eastcott, J. I. & Easton, E. B. Sulfonated silica-based fuel cell electrode structures for low humidity applications. *J. Power Sources* **245**, 487–494 (2014).
47. Eastcott, J. I. & Easton, E. B. Investigation of transport mechanisms for sulfonated silica-based fuel cell electrode structures. *J. Electrochem. Soc.* **162**, 764–771 (2015).
48. Alipour Moghadam Esfahani, R., Moghaddam, R. B., Ebraliidze, I. I. & Easton, E. B. A hydrothermal approach to access active and durable sulfonated silica-ceramic carbon electrodes for PEM fuel cell applications. *Appl. Catal. B Environ.* **239**, 125–132 (2018).
49. Easton, E. B. *et al.* Recent Advances with Sulfonated Silica Ceramic Carbon Electrodes for Fuel Cells. *ECS Trans.* **92**, 559–570 (2019).
50. Zeng, J., Amici, J., Monteverde Videla, A. H. A., Francia, C. & Bodoardo, S. Synthesis of mesoporous carbons and reduced graphene oxide and their influence on the cycling performance of rechargeable Li-O₂ batteries. *J. Solid State Electrochem.* 1–12 (2016). doi:10.1007/s10008-016-3391-4
51. Zhao, D. *et al.* Triblock copolymer syntheses of mesoporous silica with periodic 50 to 300 angstrom pores. *Science* (80-.). **279**, 548–552 (1998).
52. Ghavidel, M. R. Z., Monteverde, A. H. A., Specchia, S. & Easton, E. B. Electrochimica Acta The relationship between the structure and ethanol oxidation activity of Pt-Cu / C alloy catalysts. *Electrochim. Acta* **230**, 58–72 (2017).
53. Lefebvre, M., Qi, Z., Rana, D. & Pickup, P. G. Chemical synthesis, characterization, and electrochemical studies of poly(3,4-ethylenedioxythiophene)/Poly(styrene-4-sulfonate) composites. *Chem. Mater.* **11**, 262–268 (1999).
54. Li, G. & Pickup, P. G. Ionic conductivity of PEMFC electrodes effect of Nafion loading. *J. Electrochem. Soc.* **150**, (2003).
55. Ren, X. & Pickup, P. G. Ion Transport in Polypyrrole and a Polypyrrole/Polyanion Composite. *J. Phys. Chem.* **97**, 5356–5362 (1993).
56. Cuccaro, R., Lucariello, M., Battaglia, A. & Graizzaro, A. Research of a HySyLab internal standard procedure for single PEMFC. *Int. J. Hydrogen Energy* **33**, 3159–3166 (2008).

57. Samms, S. R. Thermal Stability of Nafion® in Simulated Fuel Cell Environments. *J. Electrochem. Soc.* **143**, 1498 (1996).
58. Lázaro, M. J. *et al.* Study and Application of Carbon Black Vulcan XC-72R in Polymeric Electrolyte Fuel Cells. in *Carbon Black: Production, Properties and Uses* (eds. Sanders, I. J. & Peeten, T. L.) 2–28 (Nova Science Publishers, Inc., 2011).
59. Alothman, Z. A. A review: Fundamental aspects of silicate mesoporous materials. *Materials (Basel)*. **5**, 2874–2902 (2012).
60. Acheampong, R. Probing the influence of relative humidity and temperature on the sulfonated silica ceramic carbon electrode for PEM fuel cell operation by. (University of Ontario Institute of Technology, 2019).
61. Long, N. V., Ohtaki, M., Ngo, V. N., Cao, M. T. & Nogami, M. Structure and morphology of platinum nanoparticles with critical new issues of low- and high-index facets. *Adv. Nat. Sci. Nanosci. Nanotechnol.* **3**, (2012).
62. Guo, X. *et al.* Performance assessment of a combined system consisting of a high-temperature polymer electrolyte membrane fuel cell and a thermoelectric generator. *Energy* **179**, 762–770 (2019).
63. Easton, E. B. & Pickup, P. G. An electrochemical impedance spectroscopy study of fuel cell electrodes. *Electrochim. Acta* **50**, 2469–2474 (2005).
64. Li, Y., Feng, C., Qu, K. N. & He, P. F. Effects of water and hydrogen content on the interaction mechanism between particles and the mechanical properties of a Nafion-based catalyst layer. *Mater. Res. Express* **6**, 085506 (2019).
65. Kaiser, J. *et al.* Influence of carbon support on the performance of platinum based oxygen reduction catalysts in a polymer electrolyte fuel cell. *J. Appl. Electrochem.* **37**, 1429–1437 (2007).
66. Moore, A. D., Holmes, S. M. & Roberts, E. P. L. Evaluation of porous carbon substrates as catalyst supports for the cathode of direct methanol fuel cells. *RSC Adv.* **2**, 1669–1674 (2012).
67. Liu, B. & Creager, S. Carbon xerogels as Pt catalyst supports for polymer electrolyte membrane fuel-cell applications. *J. Power Sources* **195**, 1812–1820 (2010).
68. Ma, Y. *et al.* Highly active Vulcan carbon composite for oxygen reduction reaction in alkaline medium. *Electrochim. Acta* **133**, 391–398 (2014).
69. Sepp, S. *et al.* Performance of Polymer Electrolyte Membrane Fuel Cell Single Cells Prepared Using Hierarchical Microporous-Mesoporous Carbon Supported Pt Nanoparticles Activated Catalysts. *Electrochim. Acta* **203**, 221–229 (2016).
70. Kim, D. S. *et al.* Enhanced electrocatalytic performance due to anomalous compressive strain and superior electron retention properties of highly porous Pt nanoparticles. *J. Catal.* **291**, 69–78 (2012).

71. Paul, R. *et al.* Boron-carbon-nitrogen foam surfaces for thermal physisorption applications. *Thin Solid Films* **528**, 187–193 (2013).
72. Chen, W. *et al.* Origins of high onset overpotential of oxygen reduction reaction at Pt-based electrocatalysts: A mini review. *Electrochem. commun.* **96**, 71–76 (2018).
73. Mahata, A., Nair, A. S. & Pathak, B. Recent advancements in Pt-nanostructure-based electrocatalysts for the oxygen reduction reaction. *Catal. Sci. Technol.* **9**, 4835–4863 (2019).
74. Reid, O., Saleh, F. S. & Easton, E. B. Determining electrochemically active surface area in PEM fuel cell electrodes with electrochemical impedance spectroscopy and its application to catalyst durability. *Electrochim. Acta* **114**, 278–284 (2013).
75. Saleh, F. S. & Easton, E. B. Diagnosing degradation within PEM fuel cell catalyst layers using electrochemical impedance spectroscopy. *J. Electrochem. Soc.* **159**, (2012).
76. Chen, Y. *et al.* Enhanced stability of Pt electrocatalysts by nitrogen doping in CNTs for PEM fuel cells. *Electrochem. commun.* **11**, 2071–2076 (2009).
77. Acheampong, R., Alipour Moghadam Esfahani, R., Moghaddam, R. B. & Easton, E. B. An organosilane-based fuel cell ionomer that mitigates carbon corrosion. *J. Electrochem. Soc. (In Press)*. (2020).
78. Stariha, S. *et al.* Recent Advances in Catalyst Accelerated Stress Tests for Polymer Electrolyte Membrane Fuel Cells. *J. Electrochem. Soc.* **165**, F492–F501 (2018).
79. Choi, D. S., Robertson, A. W., Warner, J. H., Kim, S. O. & Kim, H. Low-Temperature Chemical Vapor Deposition Synthesis of Pt–Co Alloyed Nanoparticles with Enhanced Oxygen Reduction Reaction Catalysis. *Adv. Mater.* **28**, 7115–7122 (2016).
80. Chen, W. F., Huang, H. Y., Lien, C. H. & Kuo, P. L. Enhanced stabilization and deposition of Pt nanocrystals on carbon by dumbbell-like polyethylenimine-terminated poly(oxypropylene)diamine. *J. Phys. Chem. B* **110**, 9822–9830 (2006).
81. Fedotov, A. A., Grigoriev, S. A., Millet, P. & Fateev, V. N. Plasma-assisted Pt and Pt-Pd nano-particles deposition on carbon carriers for application in PEM electrochemical cells. *Int. J. Hydrogen Energy* **38**, 8568–8574 (2013).
82. Mintsouli, I. *et al.* Pt-Ni carbon-supported catalysts for methanol oxidation prepared by Ni electroless deposition and its galvanic replacement by Pt. *J. Solid State Electrochem.* **17**, 435–443 (2013).
83. Banham, D. *et al.* Novel Mesoporous Carbon Supports for PEMFC Catalysts. *Catalysts* **5**, 1046–1067 (2015).
84. Moghaddam, R. B. & Easton, E. B. Impedance spectroscopy assessment of catalyst coated Nafion assemblies for proton exchange membrane fuel cells. *Electrochim. Acta* **292**, 292–298 (2018).